Measurement of the Top-Antitop and Z^0-Boson Production Cross Sections and Their Ratio in the Dileptonic Decay Channels at $\sqrt{s}$ =7 TeV with the CMS Experiment

Messung der Produktionswirkungsquerschnitte von Top-Antitop-Paaren und Z^0-Bosonen als auch deren Verhältnis in den dileptonischen Zerfallskanälen bei $\sqrt{s}$ =7 TeV mit dem CMS Experiment

Diplomarbeit

Department Physik

der Universität Hamburg

vorgelegt von

Jan Kieseler

aus Hamburg

Erstgutachterin: Dr. Katerina Lipka
Zweitgutachter: Prof. Dr. Dieter Horns

Abstract

In this thesis, the production of Z^0 boson and top-quark pairs is studied. In particular, the decays into two leptons are analyzed. The data recorded by the CMS experiment at the LHC in 2011 is used, corresponding to an integrated luminosity of 1.14 fb^{-1}. The candidates are selected by requiring two isolated opposite-sign lepton candidates. The $t\bar{t}$ and Z^0 signal are disentangled by separating the events into two different regions of the invariant mass of the lepton candidate pair. The selection of the $t\bar{t}$ event candidates also includes the requirement for two jets, missing transverse momentum and at least one jet originating from a b-quark. Data-driven estimates for trigger and isolation efficiencies are determined and the electron energies are re-calibrated using the Z^0 invariant mass peak. The main backgrounds to the $t\bar{t}$ and to the Z^0 events are corrected to or obtained from data, respectively.

A Z^0 boson production cross section of $\sigma_Z = 31.1 \pm^{0.9}_{1.3}$ (syst.) ± 1.4 (lumi.) nb is determined, corresponding to the combination of decay channels into different lepton types. A $t\bar{t}$ production cross section using the dileptonic channels of $\sigma_{t\bar{t},comb} = 181.6 \pm 3.5$ (stat.) $\pm^{12.0}_{12.7}$ (syst.) ± 8.2 (lumi.) pb is obtained, corresponding to the combination of the e^+e^-, $\mu^+\mu^-$ and $e^\pm\mu^\mp$ channels. A cross section ratio of $t\bar{t}$ to Z^0 production of $\sigma_{t\bar{t}}/\sigma_Z = 5.52 \pm 0.18$ (stat.) $\pm^{0.48}_{0.54}$ (syst.) $\cdot 10^{-3}$ is measured.

This cross section ratio can be used for an alternative determination of the top-pair production cross section, making use of the precise prediction of the Z^0 boson production in the kinematic range of the analysis. The advantage of this method is a cancellation of the luminosity uncertainty. In this way, a value of the top-pair production cross section of $\sigma^R_{t\bar{t},comb} = 164.0 \pm 5.4$ (stat.) $\pm^{14.2}_{15.9}$ (syst.) ± 7.1 (theo.) pb is obtained, where (theo.) denotes the uncertainty due to the prediction of the Z^0 boson production cross section.

Zusammenfassung

In dieser Arbeit wird die Produktion von Z^0 Bosonen und Top-Quark Paaren mit anschließendem Zerfall in zwei Leptonen untersucht. Die Analyse basiert auf Daten aufgenommen vom CMS Experiment am LHC im Jahre 2011 entsprechend einer integrierten Luminosität von 1.14 fb^{-1}. Die Top-Paar und Z^0-Bosonkandidaten werden selektiert, indem zwei isolierte, entgegengesetzt geladene Leptonkandidaten gefordert werden. Beide Signalprozesse werden separiert, indem die invariante Masse des Leptonpaares in zwei Regionen aufgeteilt wird. In weiteren Schritten der Top-Paarselektion werden zusätzlich zwei Jets, fehlende Transversalenergie und mindestens ein Jet gefordert, der auf ein b-Quark zurück zu führen ist. Mithilfe auf Daten basierender Methoden werden Effizienzen für Trigger- und Isolationskriterien bestimmt. Die Z^0-Resonanz in der Verteilung der invarianten Masse der zwei Leptonkandidaten wird dazu genutzt die Energie der Elektronenkandidaten neu zu kalibrieren. Die Untergrundprozesse zu dem Z^0 und $t\bar{t}$ Signal werden aus den Daten bestimmt bzw. mithilfe der Daten reskaliert.

Der Wirkungsquerschnitt für die Z^0-Boson-Produktion wird aus der Kombination der Zerfallskanäle in verschiedene Leptonentypen zu $\sigma_Z = 31.1 \pm^{0.9}_{1.3}$ (syst.) ± 1.4 (lumi.) nb bestimmt. Die gewonnenen Wirkungsquerschnitte in den drei Kanäle des dileptonischen Top-Paar-Zerfalls e^+e^-, $\mu^+\mu^-$ und $e^\pm\mu^\mp$ werden kombiniert zu einem Wirkungsquerschnitt für die $t\bar{t}$ Produktion von $\sigma_{t\bar{t},comb} = 181.6 \pm 3.5$ (stat.) $\pm^{12.0}_{12.7}$ (syst.) ± 8.2 (lumi.) pb. Das Verhältnis der beiden Wirkungsquerschnitte wird gemessen zu $\sigma_{t\bar{t}}/\sigma_Z = 5.52 \pm 0.18$ (stat.) $\pm^{0.48}_{0.54}$ (syst.) $\cdot 10^{-3}$.

Alternativ wird dieses Verhältnis genutzt um den $t\bar{t}$ Wirkungsquerschnitt zu bestimmen, indem die präzise Theorievorhersage des Z^0 Wirkungsquerschnitts im selben Energiebereich ausgenutzt wird. Der Vorteil dieser Methode besteht darin, dass die Unsicherheit der Luminositätsmessung nicht mehr beiträgt. Der auf diese Weise bestimmte Wert für den Top-Paar-Produktionswirkungsquerschnitt is $\sigma^R_{t\bar{t},comb} = 164.0 \pm 5.4$ (stat.) $\pm^{14.2}_{15.9}$ (syst.) ± 7.1 (theo.) pb. Dabei trgt die Theorieunsicherheit (theo.) signifikant bei.

Contents

CHAPTER 1

Introduction

Fundamental particles and their interactions are described by the Standard Model that comprises leptons and quarks which build up matter, and gauge bosons, which mediate the exchange forces between them. Quarks and leptons are spin-1/2 particles (fermions), while bosons have integer spin. In the parton picture, combinations of two or three quarks, held together by gluons, create hadrons, thereby defining their mass and quantum numbers. Baryons are composed out of three quarks, mesons are made of quark-antiquark pairs.

The heaviest known fundamental particle is the top quark. Its properties are important ingredients in the Standard Model and are important parameters in predictions for new physics. The way to study the top production and its decay are proton (anti-) proton collisions at high energies, such as at the Tevatron of the Large Hadron Collider (LHC).

The LHC is a proton-proton collider designed to discover new particles and shed light on processes that occur in an energy regime not accessible before. Particles emerging from the collisions are detected by experiments, which are located at the interaction points of the collider. One of these is the Compact Muon Solenoid (CMS), a general-purpose detector designed to study the nature of electroweak symmetry breaking for which the Higgs mechanism is presumed to be responsible, to look for evidence of physics beyond the Standard Model, to study aspects of heavy ion collisions and to explore high energy physics at the TeV scale involving particles with high masses.

The top quark and the Z^0 boson, which are subject to this thesis, are the heaviest elementary particles discovered so far. Top quarks offer a unique possibility to study bare quark properties and to constrain the Standard Model parameters, such as the Higgs mass. The top-pair production cross section is measured at the LHC with sufficient precision, the uncertainty of the measurement being limited by the systematics. With increasing luminosity at the LHC, additional systematic studies can be performed in order to minimize the uncertainty, such that the luminosity uncertainty will become a dominant contribution. Therefore, an effort can be made to use a well-known process as a normalization for the determination of the $t\bar{t}$ cross section instead. The Z^0 boson is one of the gauge bosons, which mediate the weak force. Its parameters were measured in e^+e^- collision experiments to a high precision, such that its production and decay can be even used for a better understanding of detector properties and serve as normalization.

In this thesis, the measurements of the top-quark pair and Z^0-boson production cross sections at a center of mass energy of 7 TeV with the CMS experiment are presented. The

Z^0 boson production cross section is also used as a normalization for the determination of the top-pair production cross section independent of the luminosity measurement.

The work is organized as follows: The Standard Model is introduced in Chapter 2 with particular focus on the top quark and the Z^0 boson and the Monte Carlo generators and detector modelling used in this analysis. In Chapter 3, the LHC machine and the CMS detector are described as well as the reconstruction of physical objects. In Chapter 4, the signal extraction procedure in which events containing $t\bar{t}$ or Z^0 bosons are identified is explained along with the estimation of reconstruction efficiencies and systematic uncertainties. The results are presented in Chapter 5.

CHAPTER 2

Top quark and Z^0 boson production in proton-proton collisions

The properties of the top quark and the Z^0 boson are important parameters in the Standard Model and determine to a wide extend the precision of our understanding of nature. In proton-proton collisions at high energies, both top quark and Z^0 boson are produced copiously and their properties can be studied with high precision. Not only accurate measurements, but also reliable theoretical models of the production mechanisms of top quarks and Z^0 bosons are necessary. In the following, the basics for understanding top quark and the Z^0-boson production are discussed.

1. The Standard Model of fundamental particles and their interactions

The Standard Model of particle physics is based on a successful quantum field theory of the strong, weak and the electromagnetic interactions [**66**]. The elementary particles of the Standard model are six *flavors* of quarks and six leptons as illustrated in Figure 2.1. The interactions between these fermions are mediated by a set of gauge bosons: gluons mediate the strong, photons the electromagnetic and the $W^{\pm}$ and Z^0 bosons the weak interaction. Quarks participate in all three fundamental interactions. The charged e, μ and τ leptons are subject to electromagnetic and weak interactions, while the neutrinos experience weak interactions only. To each fermion corresponds an antiparticle with a charge equal in magnitude but of opposite sign.

The electromagnetic interaction of charged particles is described by Quantum Electrodynamics (QED). QED is a relativistic quantum field theory emerging from the principle of local gauge invariance. The demand for local gauge invariance with respect to spacetime dependend transformations represented by the $U(1)$ group results in the field A_μ, which can be identified as the photon field.

The weak interaction is mediated by three massive gauge bosons: the neutral Z^0 and the charged W^+ and W^-. A $W^{\pm}$ boson couples to left-handed fermions or right-handed antifermions respectively (in the following the right-handed anti-fermion counterparts are always implied). In consequence CP symmetry is violated in weak interactions. The amplitude S^2 of an interaction via a boson carrying a momentum Q^2 with the mass m_B obeys Equation 2.2. Therefore, at low energies the high masses of the gauge bosons reduce the strength of the interaction although the coupling itself is of the order of the electromagnetic coupling. An example for a weak interaction at low energies is the β decay.

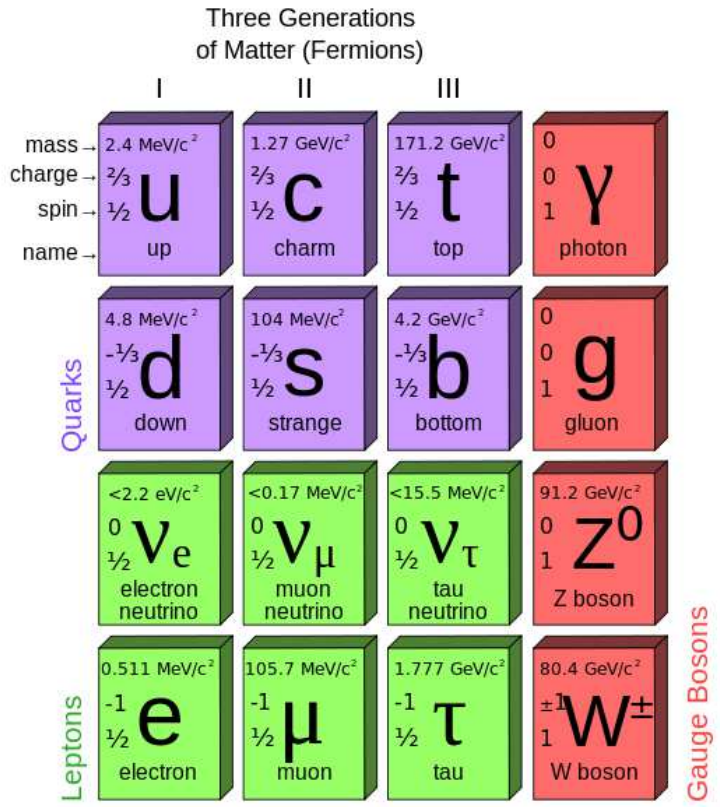

Figure 2.1: All fundamental particles of the standard model including their masses, charges and spins. The Higgs boson is not listed here [**70**].

Weak eigenstates and mass eigenstates are not necessarily the same. Weak eigenstates can consist of a superposition of different mass or strong eigenstates in both the lepton and the quark sector. In the lepton sector this results in neutrino oscillations for the quarks in quark-generation changing weak interactions mediated by $W^{\pm}$ bosons. The transition probability for the quarks is described by the Cabibbo-Kobayashi-Maskawa (CKM) matrix [**56**]:

$$\begin{pmatrix} d' \\ s' \\ b' \end{pmatrix} = \begin{pmatrix} V_{ud} & V_{us} & V_{ub} \\ V_{cd} & V_{cs} & V_{cb} \\ V_{td} & V_{ts} & V_{tb} \end{pmatrix} \begin{pmatrix} d \\ s \\ b \end{pmatrix} \tag{2.1}$$

The weak eigenstates d', s' and b' are superpositions of the strong eigenstates d, s, and b. In the Standard Model, the CKM matrix is unitary. Given the well measured values of the first rows of the matrix and the unitarity requirement, V_{tb} is almost 1 and $V_{td} \approx V_{ts} \approx 0$. Measurements of V_{tb} itself without the unitarity assumption result in $|V_{tb}| > 0.78$ [**8**]. The probability P_{bW} for the decay of top quarks to b-quarks with respect to other channels is given by Equation 2.3. Therefore, top quarks decay almost exclusively into a b-quark and a $W^{\pm}$ boson.

$$S \propto \frac{1}{|Q^2| - m_B^2} \tag{2.2}$$

$$P_{bW} = \frac{|V_{tb}|^2}{|V_{tb}|^2 + |V_{ts}|^2 + |V_{td}|^2} \tag{2.3}$$

The weak and the electromagnetic force can be described in a unified theory. A $U(1)_Y$ and $SU(2)_L$ transformation is introduced. The field B_μ couples via the hypercharge operator Y, which is defined via the operators for charge, Q, and the third projection of the isospin, T^3: $Y = 2(Q - T^3)$. The fields $W_\mu^{(1,2,3)}$ couple to left-handed isospin doublets via the isospin operators $T^{(1,2,3)}$. The left-handed fermions are ordered in isospin doublets, which are eigenstates to the T^3 operator with the eigenvalues of $\pm 1/2$. The $W^{\pm}$ boson fields can be written as ladder operators $W_\mu^{\pm} \propto W_\mu^1 \mp i W_\mu^2$ which flip the eigenvalue of T^3. Orthogonal superpositions of the W_μ^3 field and the B_μ field result in the A_μ and the Z_μ boson fields:

$$A_\mu = W_\mu^3 \cos\theta_W - B_\mu \sin\theta_W \tag{2.4}$$

$$Z_\mu = W_\mu^3 \cos\theta_W + B_\mu \sin\theta_W \tag{2.5}$$

The mixing angle θ_W is a free parameter and can be determined experimentally.

The experimental manifestation of the electroweak unification was provided at the HERA accelerator [**51**], where it was shown that the cross sections of interactions mediated by a photon (with a Z^0 boson contribution) and the ones mediated by $W^{\pm}$ bosons are similar at scales close to the $W^{\pm}$ boson mass.

In order to preserve the $SU(2)_L \otimes U(1)_Y$ gauge symmetry, all particles are required to be massless, which contradicts the experimental measurements. The question of particle mass can be solved by introducing an additional gauge invariant field, the Higgs field. Its minimum is different from zero, such, that a spontaneous symmetry breaking results in an non-zero vacuum expectation value. This implies, that the particles obtain their masses via interaction with the Higgs field without violating the gauge symmetry. The manifestation of the Higgs field, the Higgs boson, has not yet been observed [**6**].

The strong interaction is described by quantum chromodynamics (QCD), based on the $SU(3)_C$ gauge group. There are three strong-charge eigenstates, the colours, named red,

green and blue and their corresponding anticolors. Due to the group structure with 8 generators there are 8 gluon fields carrying colour themselves which mediate the strong force and interact amongst each other. The strong coupling constant α_s, which quantifies the coupling to the colour charge, is strongly dependent on the momentum transfer Q^2 of the interaction. At low Q^2, which corresponds to large interaction distances, α_s becomes very large due to the gluon self-coupling. At high Q^2, α_s becomes very small (asymptotic freedom). In consequence the energy needed to separate two quarks increases with distance until it is energetically more beneficial to produce an additional quark-antiquark pair (confinement). This results in *hadronization*, a process where colorless hadrons are created: baryons (3-quark combinations) and mesons (2-quark combinations).

2. Factorization in proton collisions

A proton-proton collision at a center of mass energy s is sketched in Figure 2.2. The process can be divided into two parts, one describing the hard interaction and one related to the proton structure. The hard interaction refers to the interaction between

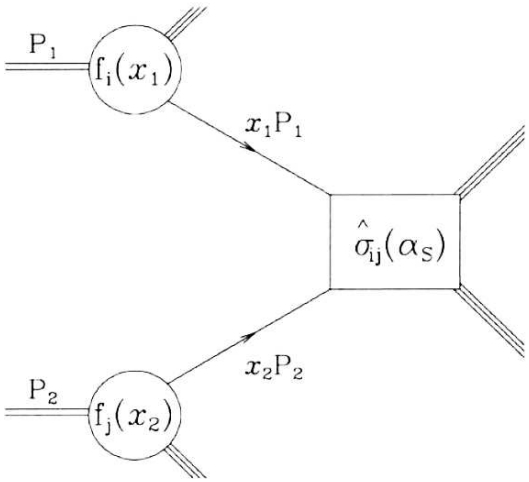

Figure 2.2: Illustration of the factorization approach used to calculate cross sections in proton-proton collisions. The hard interaction cross section $\hat{\sigma}_{ij}(\alpha_s)$ of the partons P_1 and P_2 is convoluted with the parton distributions functions f_i and f_j describing the inner structure of the proton.

two partons in the colliding protons. In the infinite momentum frame, x_1 and x_2 can be understood as the momentum fractions of the colliding protons, carried by the interacting partons. The kinematics of the hard interaction is then described by the effective center-of-mass energy $\hat{s} = \tau \cdot s = x_1 \cdot x_2 \cdot s$, the proton momentum fractions x_1 and x_2, and the energy scale Q or mass of the produced particles $M = Q$.

The cross sections of processes in proton (anti-)proton collisions σ can be factorized by a convolution of the matrix element of the parton-parton interaction and the proton

structure:

$$\sigma(s) = \sum_{i,j} \int_{\tau_0}^{1} \frac{d\tau}{\tau} \cdot \frac{dL_{ij}(\mu_F^2)}{d\tau} \cdot \hat{s} \cdot \hat{\sigma}_{ij}\left(\alpha_s(\mu_R^2)\right) \tag{2.6}$$

$$\tau \cdot \frac{dL_{ij}}{d\tau} \propto \int_{0}^{1} dx_1 dx_2 \left(x_1 f_i(x_1, \mu_F^2) \cdot x_2 f_j(x_2, \mu_F^2)\right) + (1 \leftrightarrow 2)\delta(\tau - x_1 x_2) \tag{2.7}$$

Here, $\hat{\sigma}_{ij}\left(\alpha_s(\mu_R^2)\right)$ represents the cross section of the parton-parton interaction described by a matrix elements, which can be calculated in perturbation theory to a certain order at the *renormalization* scale μ_R^2. The term 2.7 represents the parton luminosity and involves a description of the structure of the colliding protons, expressed in terms of parton density functions, PDFs, $f_{i,j}$. Those PDF represent the probability for a parton i to carry a momentum fraction x_i of the proton momentum at a *factorization* scale μ_F^2. The PDFs of both interacting protons enter multiplicatively into the the calculation of the process cross section. Therefore the precise knowledge of the PDFs is of particular importance for cross-section predictions [**54**].

The PDFs are experimentally determined from structure function measurements in deep inelastic scattering experiments at HERA [**7**], neutrino-nucleon scattering, fixed target experiments [**67, 14**] and the Tevatron. The x-dependence of the of the parton distributions is not yet calculable in perturbative QCD and has to be parametrized at a certain scale $Q_0 = \mu_{F,0} = \mu_{R,0}$. The dependence on Q is described by the DGLAP evolution equations [**53, 58, 50, 12**]. The resulting PDFs depend on the order in which the perturbative QCD calculation is performed, the assumptions about the parametrization and the treatment of heavy quarks [**54**].

3. The Z^0-boson production and decay

With its measured mass of $m_Z = 91.1876(21)$ GeV [**61**] the Z^0 boson is the heaviest boson observed so far. It was discovered 1983 by the UA1 and UA2 experiments at the SPS collider at CERN [**46**] long after its introduction in the theoretical framework of the Standard Model in the 1960s. Precise measurements of the Z^0 boson properties were performed in e^+e^- collider experiments at LEP [**61**]. The Z^0 production amplitude peaks at the Z^0 boson mass as shown in Figure 2.3. The peak can be described by a Breit-Wigner function. The width of Γ_Z =2.4952(23) was determined [**61**], corresponding to a lifetime of $\approx 10^{-25}$ s.

A variety of fundamental parameters of the electroweak Standard Model can be accessed through investigations of Z^0 boson production and properties, such as forward-backward asymmetry and the ratio of the Z^0 boson and the $W^{\pm}$ boson masses, which are directly linked to the weak mixing angle θ_W. The coupling of the Z^0 to different fermions sheds light on the coupling constants of the B_μ and W_μ^i fields and the measurement of the partial widths of Z^0 in leptonic and hadronic channels constrains the number of lepton generations. Meanwhile, the properties of the Z^0 boson are precisely known and its

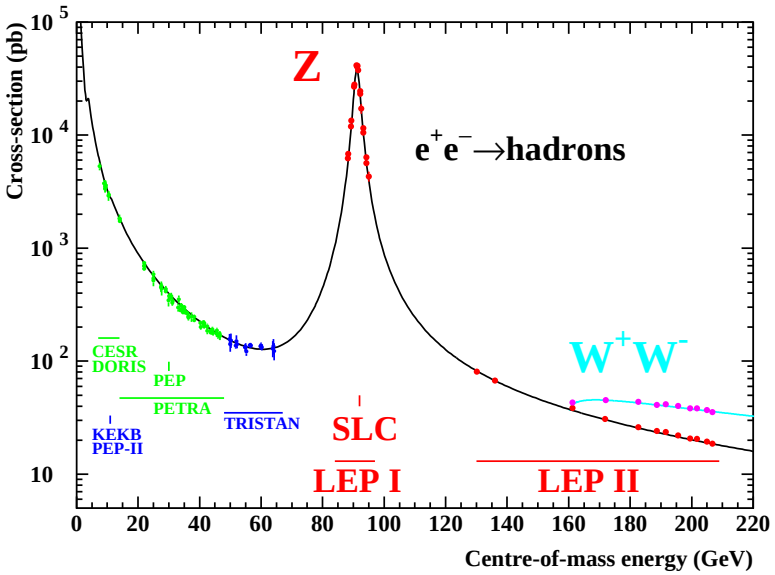

Figure 2.3: The hadronic Z^0-boson cross section as a function of center-of-mass energy. The solid line is the Standard Model prediction, and the points are the experimental measurements. Also indicated are the energy ranges of various e^+e^- accelerators [**65**].

resonant production makes it possible to use the Z^0 production for detector calibration and alignment purposes.

The Z^0 boson production is dominated by Drell-Yan processes (quark-antiquark annihilations) as shown in Figure 2.4. Due to an interference with the photon production, the contributions from the photon and the Z^0 boson can not be disentangled. In case of Z^0 exchange, the invariant mass of the fermion pair forms a resonance between 60 GeV and 120 GeV. The Z^0 decays hadronically (quark-antiquark pairs forming two jets) or leptonically into 2 opposite charged leptons of the same flavor.

At the LHC, the Z^0 boson is produced with a large cross section, as shown in Figure 2.4, through the Drell-Yan process with a contribution of 65% at leading order with the remaining 35% originating from higher order corrections. With measurements of the Z^0 boson at the LHC, electroweak parameters can be studied thoroughly and the d-type quark distribution in the proton may be constrained by the rapidity distribution of the Z^0 boson production [**45**].

Therefore, understanding its production is crucial for the LHC program [**52**]. Due to the high event rate at the LHC, the measurements of Z^0 boson production are not limited by statistics. Leading order (LO) and even next-to-leading order (NLO) predictions for Z^0 production are insufficient for a precise comparison with data; more accurate predictions are required which are provided at NNLO. In this thesis, the Z^0 boson cross section results are compared to a fully exclusive NNLO QCD calculation, which incorporates $\gamma - Z^0$ interference, finite width effects, the leptonic decay of vector bosons, such as the Z^0, and the corresponding spin correlations [**20**]. The calculation is implemented in FEWZ [**52**] and performed based on the proton structure described by the CTEQ6M [**62**] parton densities.

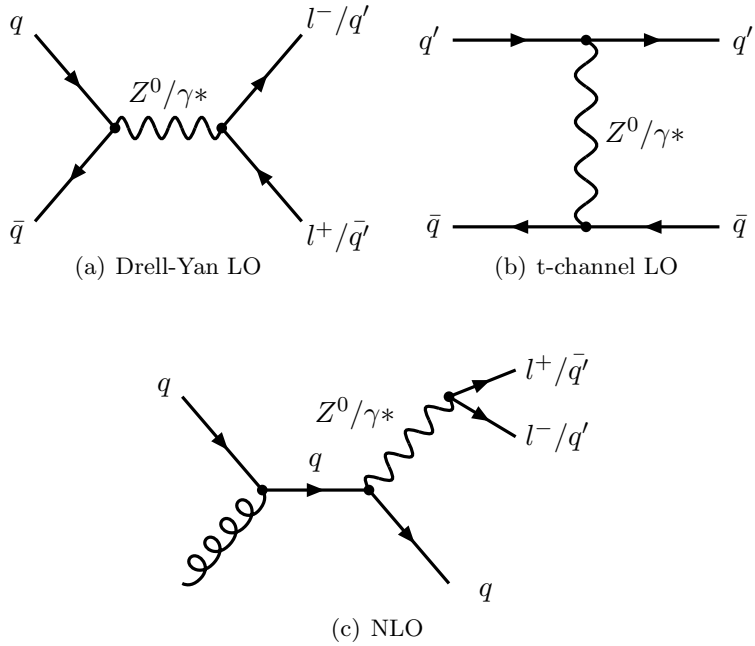

(a) Drell-Yan LO (b) t-channel LO

(c) NLO

Figure 2.4: Feynman diagrams for Z^0 production in proton-proton collisions with l being any lepton or leptoneutrino and q, q' being quarks of any flavor.

4. The top quark

The top quark is the heaviest particle of the Standard Model and was discovered 1995 at the Tevatron [**4**]. The production cross section for top quarks, as illustrated in Figure 2.5, is orders of magnitude smaller than for Z^0 or $W^{\pm}$ boson production. Top quark properties are important parameters in calculations in the Standard Model and beyond. The top mass enters radiative corrections to the electroweak coupling at low energies together with the $W^{\pm}$ mass and the Higgs mass. The latter can be constrained with the precise knowledge of the other parameters. Also for direct Higgs production, the top quark plays an important role due to its high mass and therefore high coupling to the Higgs boson.

In searches for new physics, the top quark might influence the electroweak symmetry breaking in Topcolor Assisted technicolor theories [**21**], or a significant deviation of $|V_{tb}|^2$ from 1 might indicate a fourth generation of fermions. Also a Z' in Topcolor or Kaluza-Klein theories would show up as a bump in the $t\bar{t}$ invariant mass spectrum and change its kinematics [**17**]. Charge asymmetry in top and antitop production can give insights to non-Standard Model boson exchange in top production.

The production of the $t\bar{t}$ pairs in proton-proton collisions is possible via quark-antiquark annihilation or gluon-gluon fusion in leading order as shown in Figure 2.6. The required energy to produce a $t\bar{t}$ pair is at least double the top mass $\approx \mathcal{O}(350$ GeV). At a center of mass energy of $\sqrt{s} = 7$ TeV, the gluon-gluon luminosity is higher than the quark luminosity at the corresponding partonic momentum fractions. Therefore 90% of $t\bar{t}$ pairs at the LHC are produced by gluon-gluon fusion.

Due to their large mass, top quarks decay before hadronization. Almost to 100%, a top quark decays into a $W^{\pm}$ boson and a b quark as illustrated in Figure 2.7. In a next step the $W^{\pm}$ bosons decay hadronically or leptonically. The $W^{\pm}$ decay determines the nomenclature of the $t\bar{t}$ decays.

For the prediction of $t\bar{t}$ cross sections, no exclusive NNLO QCD calculations are performed so far. Instead, different approximations to calculate higher order corrections to the NLO predictions are available (approximate NNLO). In this thesis, three calculations are compared to the measured $t\bar{t}$ cross section, which are briefly described in the following.

The prediction by Langenfeld *et al.* [**57**] takes into account NNLO contributions from logarithmically enhanced terms near the production energy threshold, where the corrections are dominated by soft gluon effects, Coulomb corrections at two loops, and terms, explicitly depending on the renormalization and factorization scale.

In the calculation of Kidonakis [**55**], soft gluon corrections to the differential cross sections, which can be expressed in power terms of the form of logarithms, are resummed at next-to-next-to-leading-logarithm (NNLL) accuracy via two loop soft anomalous dimension matrices [**15**]. Within this model, approximate NNLO differential and total cross sections can be calculated.

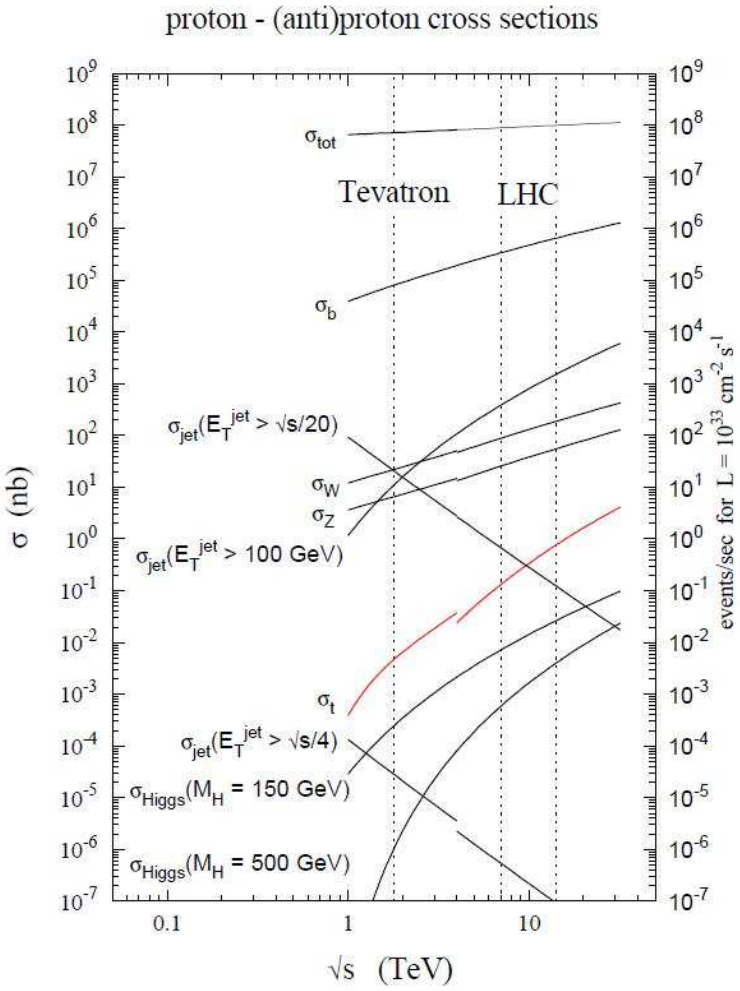

Figure 2.5: The cross section expectations for selected standard model processes as functions of the center of mass energy $\sqrt{s}$. The dashed vertical lines mark the center of mass energy at the Tevatron at 1.96 TeV and at the LHC at 7 TeV or 14 TeV, respectively. For $\sqrt{s} < 4$ TeV the cross sections for $p\bar{p}$ collisions are shown and for $\sqrt{s} > 4$ TeV for pp collisions. [**48**]

Ahrens *et al.* [**10**] have improved the existing calculations of the double-differential cross section in the invariant mass and the scattering angle by using techniques from soft-collinear effective theory [**16**] to perform NNLL resummation of threshold algorithms. An approximate formula for the differential cross section at NNLO in fixed-order perturbation theory is derived and matched in the threshold region with exact results at NLO in fixed-order perturbation theory.

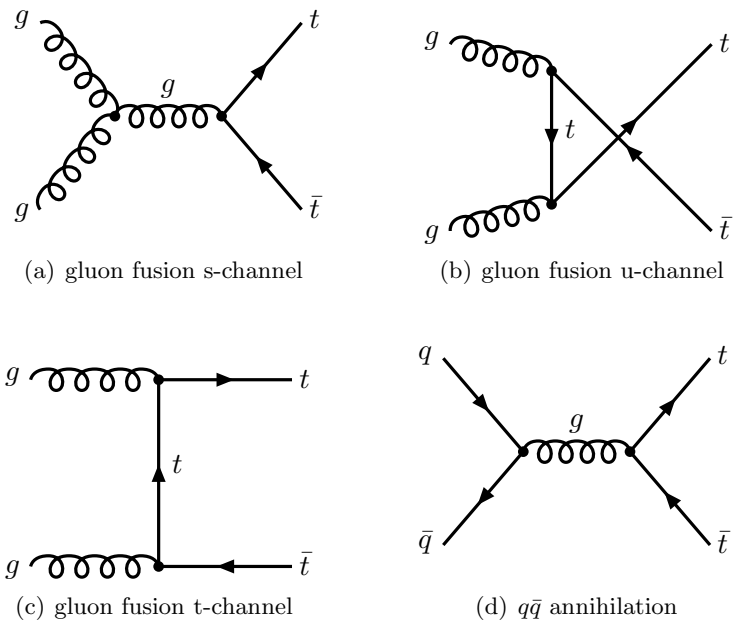

(a) gluon fusion s-channel (b) gluon fusion u-channel

(c) gluon fusion t-channel (d) $q\bar{q}$ annihilation

Figure 2.6: Feynman diagrams of top pair production at leading order.

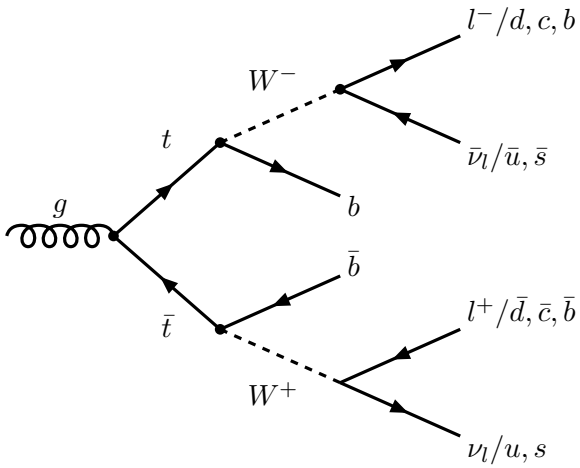

Figure 2.7: Decay of the $t\bar{t}$ pair into $b/\bar{b}$ quarks and $W^{\pm}$ bosons on tree level including subsequent leptonic and hadronic $W^{\pm}$ decays with l being e, μ, τ.

In QCD, the prediction of the top-pair production cross section depends strongly on the assumption on the top mass value. In Figure 2.8 the dependence of the predicted cross sections at approx. NNLO are shown as a function of the top mass.

The proton structure in the predictions is described by MSTW08NNLO [**59**]. The dominant uncertainty of the prediction is the uncertainty of the PDF and assumptions on α_s. The contribution of missing higher-order corrections is estimated through a variation of factorization and renormalization scales in the calculations, which however does not exceed 4%.

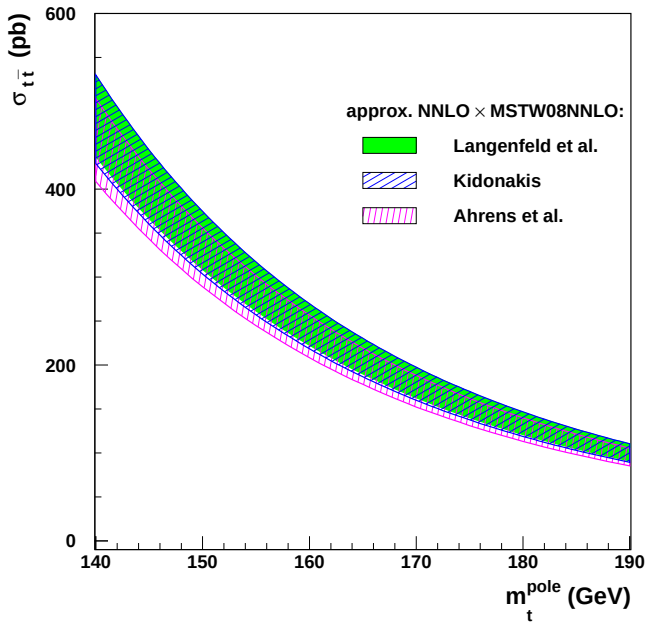

Figure 2.8: Top-mass value m_t^{pole} dependence of the three [**57, 55, 10**] theory predictions for the $t\bar{t}$ production cross section $\sigma_{t\bar{t}}$.

The prediction from Langenfeld *et al.* is calculated [**34**] using the Hathor program [**11**]. The renormalization and factorization scale are varied independently. For the calculation [**55**], the uncertainties due to the top quark mass value, parton luminosities and scale variations are provided by the author. The third prediction [**10**] for the top-pair production cross secton is calculated using the TopNNLO program [**10**]. In the calculations [**55, 10**], the renormalization and factorization scale are varied simultaneously.

5. Monte Carlo generators

In order to be able to compare theory predictions to the experimental observations based on the detector responses, not only a prediction of the cross section of a particular process is necessary. The following production and decay of all final-state particles has to be simulated and transformed into detector signals, as in case of the measurement.

Monte Carlo generators are necessary to simulate the cross sections of particular physical processes and the subsequent particle decays. In this thesis, they are used to investigate the kinematics of signal and background. An event generator produces a large number of events which are statistically distributed according to the cross section predictions of the implemented model. Events are generated in steps:

- The incoming scatterers are characterized. In case of the LHC, two protons collide. Their structure is described by PDFs. A parton from one proton interacts with a parton from the second proton in a hard scattering process according to the particle-particle cross section.
- The outgoing particles further decay and generate showers.
- The proton remnants can still carry color charge and interact with the final state.
- Phenomenological models describe fragmentation of the partons to observable hadrons. These hadrons can be unstable and decay further.

Most event generators are based on leading or next-to-leading order matrix element calculations. The contribution of higher orders are included via different models of parton showering. In the following, the specific event generators used in this analysis are described.

Pythia6 [**64**] is a general-purpose MC event generator is based on LO matrix elements. Higher order effects like initial state radiation (ISR), final state radiation (FSR) are taken into account via parton shower models. The decays of τ leptons are simulated using an additional program, *Tauola* [**49**]), which incorporates a substantial amount of specific results from distinct τ lepton measurements, QED corrections and spin information.

MadGraph [**13**] is a generator for matrix elements on tree-level for pp and $p\bar{p}$ collisions. In consequence, its calculations include ISR, FSR and additional jet production in higher orders. For the simulation of hadronization and parton showering it is typically interfaced to Pythia. To avoid double counting in gluon radiation simulation in the showering and matrix element, an energy threshold (matching threshold) is introduced, which assigns each jet production to a distinct generator according to its energy.

The Powheg generator [**63**] uses a different approach to avoid this double counting. It incorporates next-to leading order (NLO) matrix element calculations and passes on interactions to parton showering generators ranked by their hardness, such, that the showering Monte Carlo is prevented from generating subsequent emissions, which are harder than the one on matrix element level.

The interaction of the generated particles with the detector and its response is modelled in a next step with *GEANT4* [**9**], which describes the interaction of particles with matter. A model of CMS detector geometry and detector materials including all subdetectors, magnetic fields, electronic systems and supporting structure is built in the software. Using this information the generated particles are fed through the simulation of bremsstrahlung, showering in calorimeters and multiple scattering. As a result, an

event dataset that is similar to the one from recorded experimental data is obtained. The information about the quantities of each generated particle is preserved and can be addressed at a later stage of the analysis.

CHAPTER 3

The LHC and the CMS experiment

1. The Large Hadron Collider

The Large Hadron Collider (LHC) [**18**] is a proton-proton (pp) ring collider[1] with a circumference of 27 km designed for a center of mass energy of $\sqrt{s} = 14$ TeV located at CERN (European Organization for Nuclear Research) near Geneva, Switzerland. Currently it is operating at a center of mass energy of $\sqrt{s} = 7$ TeV for pp collisions.

Two proton beams running in opposite direction are led in bunches in two evacuated beam pipes by helium-cooled superconducting magnets with a field up to 4.16 T. They are focused and collided at four interaction points, where four collider experiments are located: ALICE (A Large Ion Collider Experiment), ATLAS (A Toroidal LHC ApparatuS), CMS (Compact Muon Solenoid), and LHCb (Large Hadron Collider beauty experiment).

The proton bunches are accelerated in steps: Hydrogen atoms are first stripped of their electrons, split and accelerated to 50 MeV in a linear accelerator. Boosters and synchrotrons then accelerate the protons to an energy of 450 GeV before they are injected in the LHC beam pipes. There, acceleration to 3.5 GeV per beam takes place which results in the designated center of mass energy of 7 TeV.

At the interaction points of the two multi-purpose experiments, CMS and ATLAS, the beams are focused to a profile of 16.7 μm diameter and collide with a crossing angle of 285 μrad and a rate of $\mathcal{O}$(40 MHz). The integrated luminosity recorded by both detectors until the end of 2011 is about 5.7 fb^{-1} as shown in Figure 3.1. The luminosity depends on the number of bunches N_b, the number of protons per bunch, N_i, in beam i, the revolution frequency ν, and the beam profile area, A, at the collision point (see Equation 3.1). The expected event rate $\mathrm{d}N_k/\mathrm{d}t$ of a certain process k is connected with its cross section σ_k through the instantaneous luminosity, the total number of signal events, N_k, through the integrated luminosity L_{int}.

$$L = \frac{N_b \cdot N_i \cdot N_j \cdot \nu}{A}, \quad \frac{\mathrm{d}N_k}{\mathrm{d}t} = L(t) \cdot \sigma_k, \quad N_k = \sigma_k \cdot \int_t L(t) = L_{int}\sigma_k \tag{3.1}$$

The LHCb detector is designed for studies of heavy flavor physics and CP violation. It covers a horizontal angle of 10 to 300 mrad and a vertical angle of 250 mrad with

[1] and heavy ion collider which is not part of this work

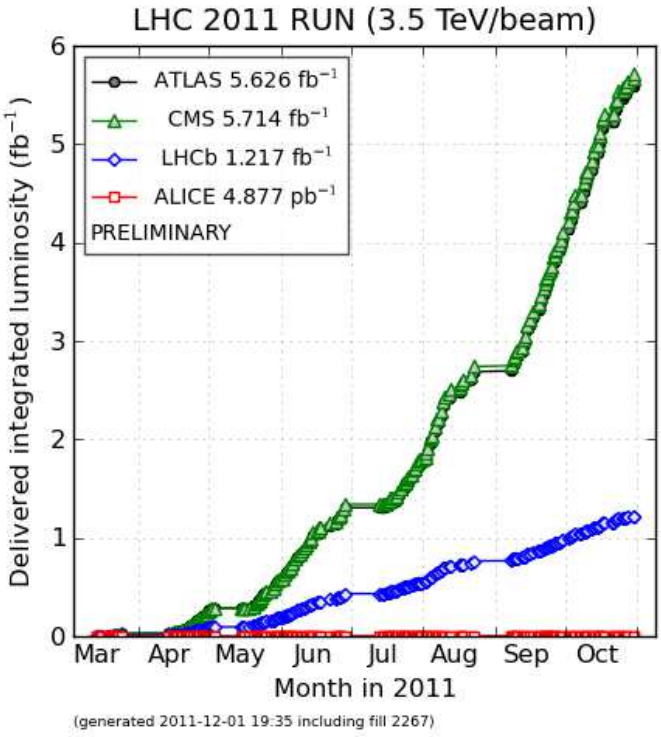

Figure 3.1: Integrated luminosity delivered by the LHC machine during the run period of 2011 at a center of mass energy of 7 TeV [**3**]

respect the beam line where heavy flavor c and b mesons are predominantly produced. The ALICE experiment is optimized to measure high track multiplicities in heavy ion collisions. Being technically a part of the CMS experiment, the TOTEM experiment is build to perform measurements of the total pp cross section and diffraction.

2. The Compact Muon Solenoid

The Compact Muon Solenoid (CMS) experiment is one of the two general-purpose detectors at the LHC, which is located about 100 m underground at one of the LHC interaction points. Its design, as shown in Figure 3.2, is radially symmetric along the beam pipe and consists of several subdetector-layers.

The origin of the CMS coordinate system is the interaction point at the center of the detector [**28**]. The x-axis points to the middle of the LHC ring, the y-axis upwards and the z-axis along the beamline in anti-clockwise direction. The polar angle θ is measured with respect to the z-axis and the pseudorapidity η is defined as $\eta = \ln(tan(\theta/2))$. The azimuthal angle ϕ is measured in the x–y plane with respect to the x-axis.

An homogeneous magnetic field of 3.8 T is produced by a solenoid coil of 12.5 m length and a diameter of 6 m. Inside the coil starting from the interaction point the tracking system is surrounded by the main calorimeters. The muon system outside the coil is embedded in the iron yoke, which returns the magnetic flux. The endcaps close the coils orifices and show the same setup.

In the following, the detector components particularly important for the analysis performed in this thesis, are described.

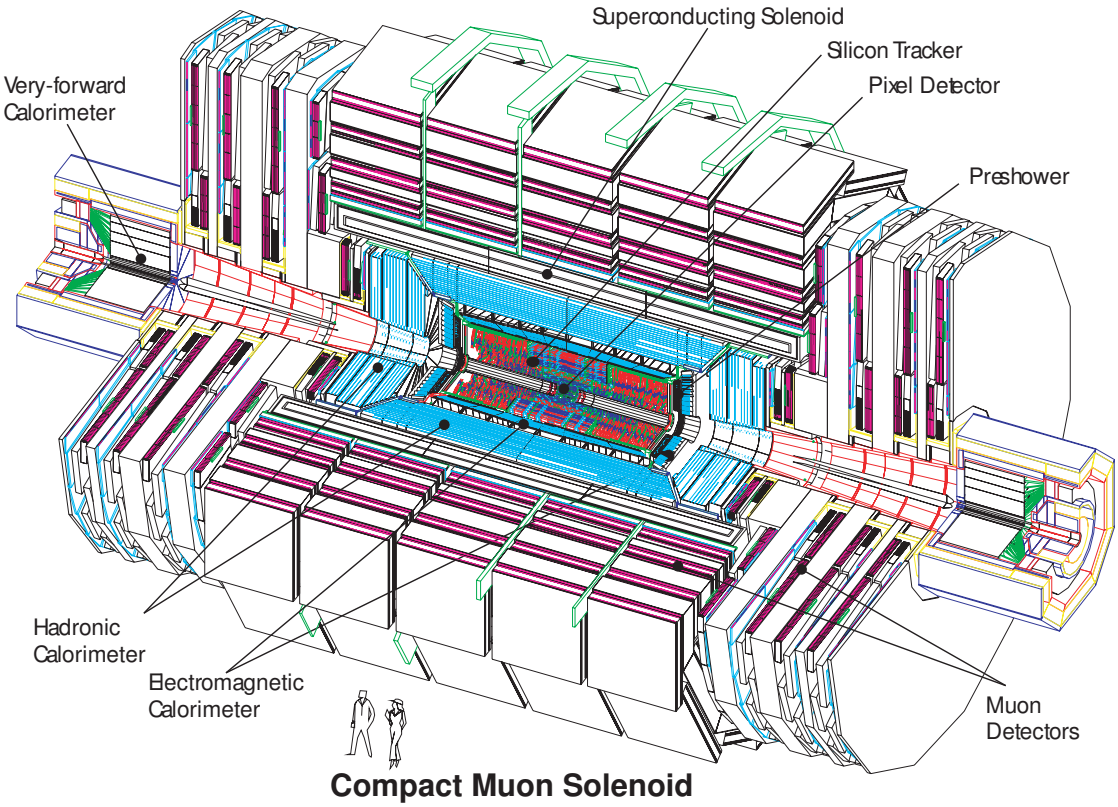

Figure 3.2: The CMS detector with its main components [**1**]

2.1. Tracker

The CMS tracker is placed on a carbon-fibre frame and cooled down to –20^{o}C. It is divided into an inner pixel detector and an outer strip detector for reconstruction of trajectories and charge measurements.

Both tracker parts, which are illustrated in Figure 3.3, are based on semi-conductive silicon diodes with embedded readout chips and correspond to an angular acceptance

of $\eta < 2.5$. They provide a fine granularity and fast readout to cope with high track multiplicities and a high bunch crossing rate.

The inner pixel detector consists of three cylindrical layers of sensors, which are located at a radial distance of 4.4 cm, 7.3 cm, and 10.2 cm, and layers in the $x - y$ plane at $|z| = 34.5$ cm and 46.5 cm [**39**]. In total 66 million pixels distributed over a total area of about 1 m^2 result in a $\rho - \phi$ resolution of ≈ 10 μm and a resolution in z of ≈ 20 μm.

The outer strip detector is divided into four parts illustrated in Figure 3.3: the Tracker Inner Barrel (TIB), the Tracker Outer Barrel (TOB), the Tracker Inner Disks (TID) and the Tracker Endcap (TEC). The barrel parts are located in the $\rho - \phi$ plane, the disk and endcap parts in the $x - y$ plane. Strips are used to collect the electrons or holes produced by charged particles passing the diode material. The first two layers of each part and the fifth layer of the TEC incorporate *stereo* modules, which provide a measurement not only in $r - \phi$ but also in $r - z$. Two strip sensors are superposed with an angle of 100 mrad to form a stereo module. So called ghost hits occur, if two particles cross a module at the same time but at different points where the stripes from the layers of a module overlap. The resulting ambiguity has to be resolved in the reconstruction process using pixel detector information. The tracker stripes are distributed over an area of approximately 200 m^2 and are read out in 9.6 million channels. The resolution is of the order of 20 μm to 50 μm in $\rho - \phi$ and 500 μm in z.

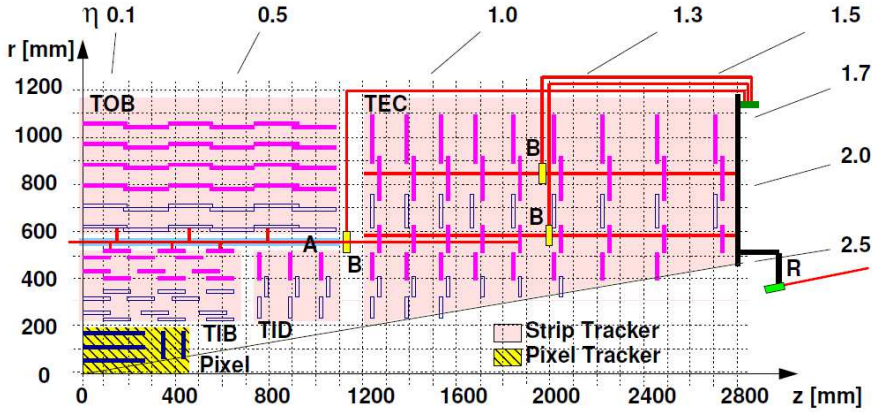

Figure 3.3: Drawing of a quadrant of the inner tracker of CMS in the $r - z$ plane. It shows the pixel detector, the tracker inner barrel (TIB), outer barrel (TOB), inner disks (TID) and endcaps (TEC) [**39**]

2.2. Electromagnetic calorimeter

The electromagnetic calorimeter (ECAL) covers two regions in $|\eta|$. The barrel calorimeter measures energies for the region $1.479 > |\eta|$ and the endcap calorimeter for $1.479 < |\eta|$ as illustrated in Figure 3.4. Both are crystal calorimeters made out of tungstate ($PbWO_4$) which acts as scintillator and absorber simultaneously. Each of in total 75848 crystals covers an angle of $0.0174^o \times 0.0174$ in $\phi \times \eta$. The material allows for a high granularity due to a short Moliere radius of 2.2 cm and a fast response, such, that 80% of the light is emitted within 25 ns.

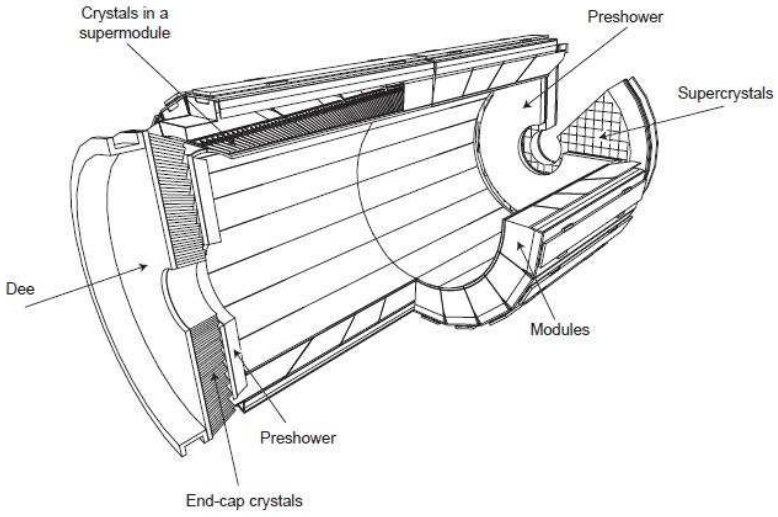

Figure 3.4: Schematic view of the electromagnetic crystal calorimeter of CMS [**37**]

The length of the barrel and endcap crystals is 22 cm or 23 cm, respectively, which corresponds to a radiation length of about $25 \cdot X_0 = 25 \cdot 0.89$ cm. The emitted light is detected by photodiodes in the barrel part and phototriodes in the endcaps. The crystals as well as the photodiodes are cooled down to a consant temperature to ensure a constant sensitivity. In front of the endcap ECAL modules for $1.653 < |\eta| < 2.6$, pre-shower detectors are placed. These are sampling calorimeters which consist of layers of altering scintillator and showering material. The preshower detectors identify neutral pions and improve the position resolution of the showers with their inbuilt silicon strip sensors. The relative resolution of the ECAL depends on the energy deposit E as given by Equation 3.2. The first term of Equation 3.2 is a stochastic term, the second describes noise from electronics and the third constant term describes leakages, non-uniformities, and non-linearities in the response.

$$\frac{\Delta(E)}{E} = \frac{2.\%}{\sqrt{E/GeV}} \oplus \frac{12\%}{E/GeV} \oplus 0.3\% \tag{3.2}$$

2.3. Hadronic calorimeter

The hadronic calorimeter is divided into four subsystems as shown in Figure 3.5. These are all sampling calorimeters: the hadronic barrel calorimeter (HB), the hadronic endcap calorimeter (HE), the outer hadronic calorimeter (HO), and the forward hadronic calorimeter (HF).

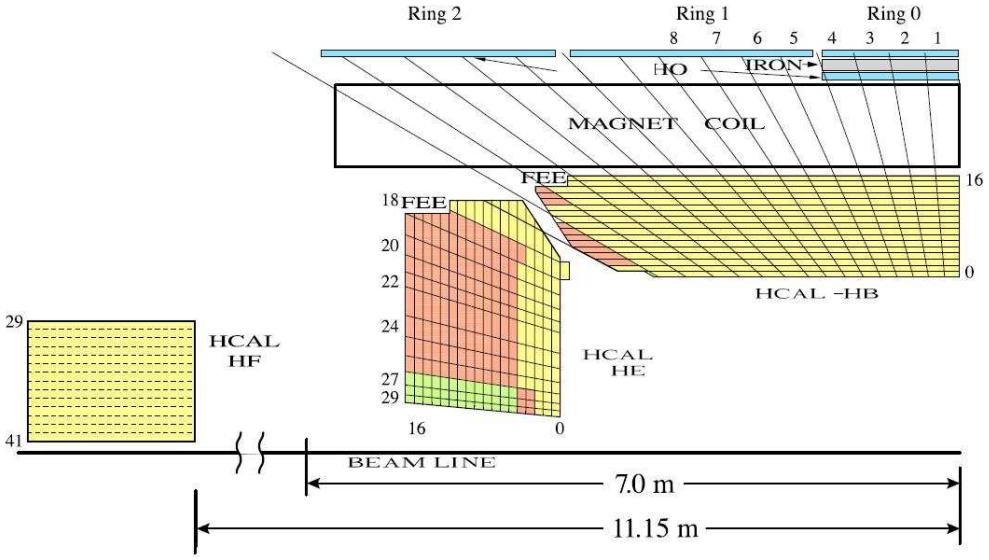

Figure 3.5: Structure of a quadrant of the CMS hadronic calorimeter in $y-z$ plane with the hadronic barrel (HB), the the hadronic endcap (HE), the hadronic forward (HF) and the hadronic outer calorimeter (HO) [**41**]

The HB covers the range of $|\eta| < 1.4$ and consists of segments (*towers*) incorporating 15 layers of altering absorber and scintillator. Each of these 2304 towers is enclosed in stainless steel and covers an angle of $0.087^o \times 0.087$ in $\phi - \eta$. The thickness increases from 5.85 interaction lenghts in the central region to about 10 at $|\eta| = 1.3$. The scintillator light is lead though wave-shifting fibres to multi-channel hybrid photodiodes.

The HO, which is located outside the solenoid coil, increases the total thickness of the hadronic calorimeters in the barrel region to above 10 interaction lengths and follows the segmentation geometry of the HB.

The HE covers the range of $1.3 < |\eta| < 3.0$. It's tower size is increasing with respect to η up to $\Delta\eta = 0.35$ and $\Delta\phi = 0.175$. Each HB and HE tower matches 5×5 ECAL segments.

The HF is positioned 11.2 m from the interaction point in z and covers the range of $3.0 < |\eta| < 5.0$. In contrast to all other HCAL parts, steel is used as absorber material and quartz fibres as scintillator. Radiation-hard materials are used, since most of the

collisions at the LHC result in soft scattering interactions in this spatial region. Apart from the luminosity measurement [**30**] this part of the calorimeter is not used in this analysis. The energy resolution of the hadronic calorimeter follows Equation 3.3 with $a = 0.847 \pm 0.016$, $b = 0.074 \pm 0.008$ for HE and HB, and $a = 1.98$, $b = 0.09$ for the HF [**41**].

$$\frac{\Delta(E)}{E} = \frac{a}{\sqrt{E/GeV}} \oplus b \tag{3.3}$$

2.4. Muon system

The most outer part of the detector is the muon system. It is embedded in the iron yoke to return the magnetic flux. The magnetic field in the return yoke is 2 T. The muon detectors consist of the following gas detectors: resistive plate chambers (RPC), drift tubes (DT) for the barrel region and cathode strip chambers (CSC) in the endcap region as illustrated in Figure 3.6.

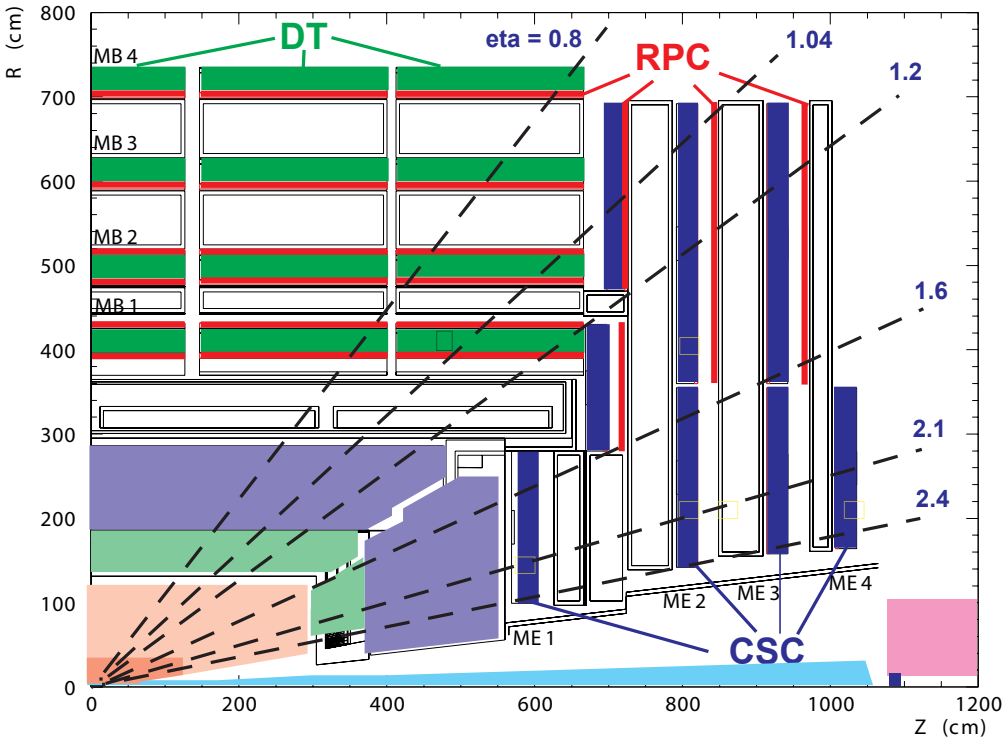

Figure 3.6: Quadrant of the CMS muon detector system consisting of Drift Tubes (DT) in the barrel and Cathode Strip Chambers (CSC) in the endcaps. Attached to both Resistive Plate Chambers (RPC) [**28**]

The gas gap in the RPCs is enclosed by two parallel phenolic resin plates with large electrical resistance and a distance of a few millimeters coated by conductive paint [**35**].

This graphite paint forms the electrodes, which induce the electric field. Insulated from the electrodes, aluminum stripes are coupled to the readout electronics. The CMS RPCs are operated in avalanche mode, meaning, that no local discharges are induced by crossing particles. This increases the read-out speed to cope with the LHC interaction rate. The RPCs provide a time resolution of about 1 ns and are used mainly for trigger purposes.

Four layers of drift tubes at $\rho = 4.0$ m, 4.9 m, 5.9 m, and 7.0 m are located in the barrel region(see Figure 3.6). The drift tubes have a rectangular profile with a maximum drift distance of 2.1 cm. Drift tubes are collected in so-called stations *MB1 – MB4* as shown in Figure 3.6, having a resolution of ≈ 100 μm.

In the endcaps four disks of CSCs (*ME1 – ME4*) provide track information. 36 chambers are combined with an RPC at the inner side to form one disk for ME2, ME3, ME4 and have a spatial resolution of about 200 μm. ME1 consists of 18 chambers and achieves a resolution of about 100 μm. The CSC signals can be used for triggering purposes, due to the fast detector response.

2.5. Luminosity determination

An accurate luminosity determination is crucial for most of the physics measurements at the LHC [**42**]. The luminosity, L, is given in Equation 3.1. The revolution frequency, ν, the number of bunches, N_b, and the bunch intensity, N_i, in beam i can be expressed in terms of the beam currents, which are measured using Fast Beam Current Transformers (FBCT) [**42**]. The FBCT measurements provide an accurate bunch-to-bunch value, leading to an overall accuracy of 3.1%.

The effective overlap area of the colliding beams, A, is obtained using Van der Meer luminosity calibration scans [**68**]. The beam profile is measured by recording the relative interaction rate as a function of the transverse beam separation The luminosity can be expressed as a product of two terms:

$$L = \frac{N_b \cdot N_1 N_2 \cdot f}{1} \cdot \frac{F(0,0)}{\int f(\Delta_x) d\Delta_x \int g(\Delta_y) d\Delta_y}, \tag{3.4}$$

where $F(x, y) = f(x)g(y)$ is the beam profile as a function of $f(x)$ and $g(y)$, Δ_x and Δ_y the beam separations in x and y and the first term is constant with respect to the scan time. Each of the functions f and g is a double-Gaussian with three free parameters: the width of each and the relative contribution of the first Gaussian with respect to the second one. Based on the measured relative interaction rate during the scan, a fit of the parameters of f and g is performed and the beam profile is obtained.

The relative luminosity, this method relies on, is determined with online data from the HF for the value used in this analysis. Two methods are employed for extracting the instantaneous luminosity. The first exploits the linear dependence between the average transverse energy per calorimeter tower and the luminosity. The second is based on *zero counting*, in which the average fraction of empty towers relates to the mean number of interactions per bunch crossing [**42**]. For the zero counting method used in this analysis,

the number of vertices is assumed to follow a poissonian distribution. This results in an estimate for the mean $n_0 = -\ln p_0$, with p_0 being the fraction of events with no interaction. The method offers a high statistical precision especially in a high pileup environment.

2.6. Trigger

With the full design luminosity, the LHC has a bunch crossing rate of 40 MHz. During each bunch crossing multiple proton-proton interactions occur; this effect is called *pileup*. Taking into account the current pileup conditions, the proton-proton interaction rate is of the order of up to 1 GHz. In order to be able to record the information delivered by the detector systems, the event rate must be reduced to approximately 100 Hz. This is achieved by a trigger system [**37**], which decides during data taking which events to record and which to reject. It consists of the hardware based Level-1 (*L1*) trigger and the software based High Level Trigger (*HLT*).

The L1 trigger is based on programmable electronics and reduces the event rate by a factor of about 1000. It is divided in local, regional and global subsystems illustrated in Figure 3.7. During a decision time of less then 1 μs the full event information is stored in a memory. The decision process starts from an event in a local detector subsystem, such as a hit pattern in a muon chamber or energy deposits in a calorimeter tower. In a second step, the information of the chambers or towers, respectively, is combined *regionally* to build *primitive* trigger objects. These are transferred from all regions of the detector to the Global Muon and Calorimeter Triggers ranked by energy, momentum and quality. The highest rank objects are then passed on to the Global Trigger, which rejects or accepts the event.

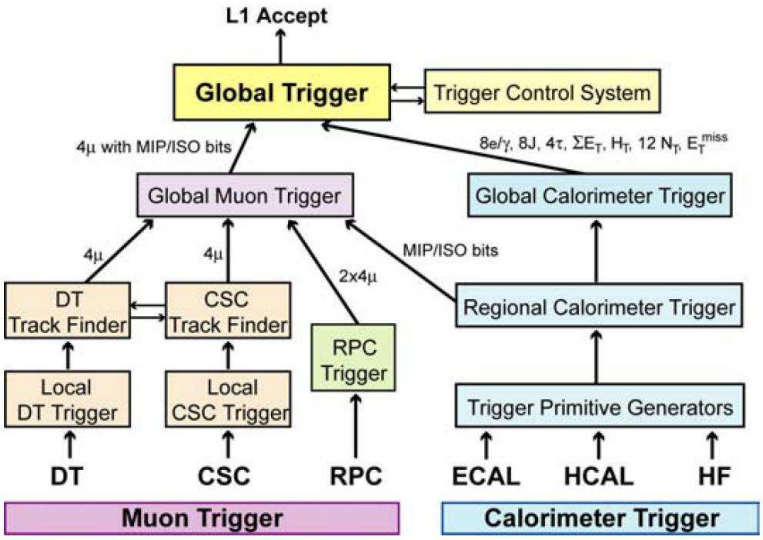

Figure 3.7: Structure of the Level-1 CMS Trigger [**37**]

Is the event accepted, the full event information from the memory pipeline is transferred to the High Level Trigger. The HLT is run on a computing farm with $\mathcal{O}(1000)$ processors and reduces the event rate from $\approx$ 100 kHz to $\approx$ 100 Hz before it is finally recorded. It takes a decision based on software algorithms which perform a fast reconstruction of physics objects. The reconstruction starts at *regions of interest* marked by the L1 Trigger and adds gradually more information from other detector subsystems e.g. from the tracker. The HLT is organized in *trigger paths*, corresponding to a sequence of requirements. If at one step the event does not fulfill the requirements of any path, the event is rejected.

3. Reconstruction

The detector responses are subject to the reconstruction procedure, common for data and simulation. In Figure 3.8, the reconstruction principle for assigning tracks and energy deposits to a muon, an electron, a photon and a neutral and a charged hadron is shown schematically. The magnetic field bends the tracks of the charged particles corresponding to their charge and their momentum. Neutral particles are neither affected by the magnetic field nor leave hits in the tracker. Muons pass all subsystems including the iron yoke with the inbuilt muon chambers. Charged and neutral hadrons deposit their energy mainly in the HCAL, electrons and photons in the ECAL only. Based on this information, the detector response is interpreted by different reconstruction algorithms. In this thesis, the particle-flow algorithm is used and described in the following.

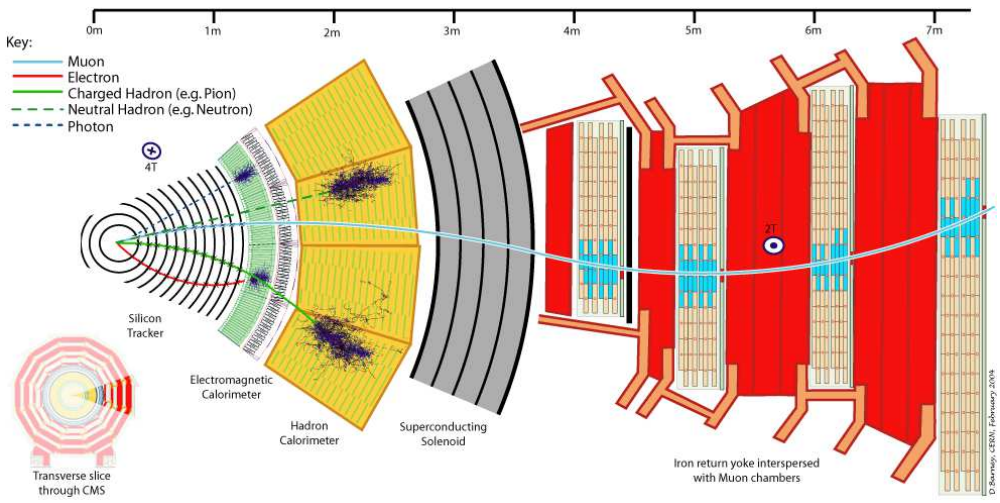

Figure 3.8: Signatures of different particles in the CMS detector [**2**].

3.1. Particle-flow event reconstruction

The particle-flow reconstruction algorithm [**69**] aims at providing a global event description at the level of individually reconstructed particles by combining information coming from all CMS subdetectors. The reconstructed particles include muon candidates, electron candidates (with individual reconstruction and identification of all bremsstrahlung photons), photons, charged hadron candidates (with or without a nuclear interaction in the tracker material), as well as stable and unstable neutral hadron candidates.

The algorithm starts with reconstruction performed independently within each CMS subdetector. Energy clustering is conducted separately in the electronic and hadronic calorimeters and track reconstruction takes place in the combined silicon and pixel tracker system. In order to combine the information obtained from the subsystems and avoid double counting, these elements are connected through a linking algorithm [**5**]. The tracks of charged particle candidates are linked to calorimeter clusters, if the extrapolated position is within the boundaries of a reconstructed energy deposit. At each stage of the following particle-flow candidate reconstruction, particular subdetector information is associated with exactly one particle candidate removed from further processing.

Linked tracks from the tracker and the muon chambers with a small energy deposit in the calorimeters are reconstructed as particle-flow muon candidates. A track associated to an energy deposit in the ECAL, which shows tangent tracks linked to ECAL deposits (identified as bremsstrahlung photon candidates), is assigned to a particle-flow electron candidate. The remaining tracks are reconstructed as charged hadron candidates, if their track momentum and energy deposit in the calorimeter is compatible. If the clustered energy exceeds the track momentum significantly, a neutral particle candidate is created. This can be a neutral hadron or photon candidate providing a large or small energy deposit fraction in the HCAL, respectively. In the same way either photon or neutral hadron candidates are created from the remaining calorimeter clusters in the last step of the particle-flow candidate reconstruction.

The tracks of the reconstructed candidates are extrapolated to the interaction vertices. The reconstructed interaction vertex with the largest value of the sum $\sum_i p_{t,i}$, where $p_{t,i}$ is the transverse momentum of the track i associated to the vertex, is selected as the primary event vertex. This vertex is used as the reference vertex for all relevant objects in the event. All particle candidates, which are associated to a different vertex, are not taken into account further. This step is referred to as the *charged hadron subtraction*.

3.2. Jet reconstruction

The aim of jet algorithms is to reconstruct the initial energy of the particle the hadronization process started from, ideally without being affected by soft emissions or collinear splitting, meaning, that the result neither depends on the detection of particles from soft radiation nor is influenced by the granularity of the detector. To a large extent, the *anti-kt* [**19**] algorithm, used in this analysis, fulfills these requirements.

In simulation, the energy of the reconstructed jet and of its parent generated particle can be estimated and a systematic deviation depending on the p_T and η of the jet becomes visible, which is corrected in steps. The first step removes the energy offset caused by electronic noise and the remaining neutral and charged hadron contributions from pileup events. In a second step, p_T- and η-dependent non-linearities in the energy determination are corrected. The correction factors are obtained using MC. Residual corrections are applied to the data, which are derived from and constantly tuned to the data and pileup conditions [**25, 36**].

3.3. Missing transverse energy

Neutrinos pass the detector material without being registered, but can be identified via missing transverse energy. The missing transverse energy ($\not\!\!E_{\mathrm{T}}$) is computed by calculating the inverse of the vectorial sum of the p_T of all reconstructed objects. It corresponds to the transverse energy of all particles, which are not detected.

CHAPTER 4

Measurement of $t\bar{t}$ and Z^0 cross section

In the following, the measurement of the $t\bar{t}$ and Z^0 boson production cross section and their ratio is described. The cross-section ratio is used for an alternative determination of the $t\bar{t}$ cross section, using the NNLO prediction for the Z^0 boson production cross section in the kinematic range of this analysis. Employing this procedure, some systematic uncertainties cancel (e.g. the luminosity uncertainty) or are reduced (e.g. trigger and selection uncertainties).

1. Data and simulated samples

The datasets used in this analysis are listed in Table 4.1 and correspond to an integrated luminosity of 1.14 fb^{-1}.

Sample	Run range	Luminosity
/DoubleMu/Run2011A-May10ReReco-v1/AOD	160431–163869	214.8 pb^{-1}
/DoubleMu/Run2011A-PromptReco-v4/AOD	165088–167913	927.9 pb^{-1}
/DoubleElectron/Run2011A-May10ReReco-v1/AOD	160431–163869	214.8 pb^{-1}
/DoubleElectron/Run2011A-PromptReco-v4/AOD	165088–167913	927.9 pb^{-1}
/MuEG/Run2011A-May10ReReco-v1/AOD	160431–163869	214.8 pb^{-1}
/MuEG/Run2011A-PromptReco-v4/AOD	165088–167913	927.9 pb^{-1}

Table 4.1: Datasets used in the analysis, the corresponding run ranges and luminosities.

In order to estimate detector and selection inefficiencies as well as background contributions, Monte Carlo simulation for the $t\bar{t}$ and Z^0 signal and the relevant background processes, are used in the analysis[1]. The simulated background contributions originate from tW, W+jets and diboson (WW, WZ^0 and Z^0Z^0) production. In the QCD background simulation, a lepton enriched MC sample (referred to as QCD MC) is used. The latter consists of a muon-enriched sample with $p_T(\mu) > 15$GeV and an electron enriched sample, which is divided into three regions depending on the electrons transverse momentum p_T: 20 GeV $< p_T <$ 30 GeV, 30 GeV $< p_T <$ 80 GeV, 80 GeV $< p_T <$ 170 GeV. The signal and the tW background MC are generated with MadGraph and interfaced with Pythia for hadronization and parton fragmentation. Additional Drell-Yan MC samples generated with Pythia are used to complete the low dilepton invariant mass

[1]Detailed list: see appendix, Tables 5.9. Parameters: see appendix, Table 5.6, 5.7, 5.8

range of < 50 GeV. The diboson MC samples are produced with Pythia, as well as the QCD MC samples.

All the simulated processes are normalized to the integrated luminosity of the data using the theory predictions for their cross sections given by the CMS generator group [**24**] except for the $t\bar{t}$ signal sample, which is normalized to the cross section measured by CMS in 2011 in the dilepton channels: 169.9 pb [**32**].

2. Event selection

In this section, the procedure to select events containing $t\bar{t}$ or Z^0 production is described. Both, Z^0 and top-pair production are identified through their decays into two leptons.

Leptonic decays of the Z^0 boson with electrons or muons in the final stare are addressed. Experimentally, the leptonic Z^0 boson decay are identified through two oppositely-charged isolated leptons with high transverse momentum. The possible combinations of charged leptons without intermediate τ decays are e^+e^- and $\mu^+\mu^-$ final states (see Chapter 2) and are referred to as ee and $\mu\mu$ channels. The contribution of tau-leptons is negligible and is not particular accounted for.

As discussed in Chapter 2, the top quark decays almost exclusively into $W^\pm$ and a b-quark. The decays of the $W^\pm$ boson determine the top-quark decay channel classification. In this analysis, only leptonic decays of the $W^\pm$ bosons into electrons or muons, including decays via a tau lepton, are considered. In turn, the dileptonic decays of the top-quark pairs are identified through two isolated leptons of opposite charge with high transverse momentum. The leptonic combinations are e^+e^-, $\mu^+\mu^-$ or $e^\pm\mu^\mp$ and are referred to as ee, $\mu\mu$ or $e\mu$ channel, respectively. In addition, two jets originating from the b-quarks and missing transverse energy from produced neutrinos are expected.

The main challenge of the $t\bar{t}$ cross section measurement is to disentangle signal and background, since the cross section for top production is orders of magnitude lower than for the background as illustrated in Chapter 2, Figure 2.5. The main background contribution are QCD processes with high track and jet multiplicities and Drell-Yan processes. Therefore, the data are subjected to several steps of a sophisticated event selection and suffer from various systematic uncertainties.

At first, the recorded data are restricted to good running conditions, described in the following. Only proton-proton collision data are analyzed and beam scraping events are excluded by requiring more than 9 tracks per event with a significant fraction of high-purity tracks [**38**]. Selected events must contain at least one non-fake primary vertex [**31**], which provides more than 4 effective degrees of freedom and a position with $|\rho| = \sqrt{x^2 + y^2} < 2$ cm and $|z| < 24$ cm. In addition, events with significant noise in the calorimeters are removed.

2.1. Trigger selection

The selected events are required to be recorded due to different High Level Triggers for each particular decay channel to be studied. All of them require at least two lepton candidates with a transverse momentum p_T above a certain threshold[2]. For the $\mu\mu$ channel, the trigger selection is run-dependent and based on increasing p_T thresholds, in order to cope with the increasing instantaneous luminosity. For the ee and the $e\mu$ channels the trigger paths also include isolation and identification criteria for the electron candidates.

2.2. Pileup reweighting

The influence of pileup on the event topology is reduced by the charged hadron subtraction and the jet energy corrections described in details in Chapter 3. Since this quantity is run-dependent, the number of interactions per event in MC does not describe the data, as shown in Figure 4.1. Therefore, the simulation is reweighted. In Figure 4.1 the distribution of primary vertices is shown before and after the reweighting for the $\mu\mu$ channel. Remaining discrepancies are covered by the systematic uncertainty, described in Section 6.

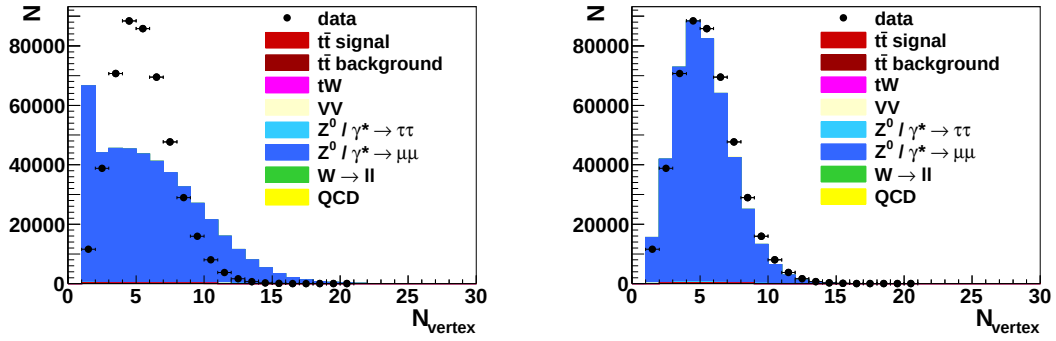

(a) default (b) reweighted

Figure 4.1: Vertex multiplicity in the $\mu\mu$ channel after the dilepton selection step (see section 2.3) before (a) and after (b) pileup reweighting. The data is shown in closed symbols. The red histogram represents the simulation of the $t\bar{t}$ production, the dark blue the prediction for the Z^0 production. The background contributions are shown in different colored histograms, as indicated in the legend.

[2]details: see appendix, Table 5.10.

2.3. Lepton selection

Signal events, both for the $t\bar{t}$ and Z^0 selection, are required to have at least two oppositely-charged leptons fulfilling certain identification and isolation criteria as described in the following.

2.3.1. *Muon selection.* Muon candidates are reconstructed using the particle-flow algorithm and are required to have a transverse momentum $p_T > 20$ GeV with a pseudo-rapidity of $|\eta| < 2.4$ and at least one associated hit in the muon chambers. Fake muons or muons from inflight decays are suppressed by requiring for a minimal number of tracker hits associated with the muon candidate ($N_{hit}^{trk} \geq 10$) and a transverse impact parameter, d_{BS}, of the muon-candidate track with respect to the primary vertex fulfilling $d_{BS} < 0.02$ cm, and a longitudinal deviation $|d_z| < 0.5$ cm. To further increase the purity of the muons candidates, the global track fit (reconstructed from tracker and muon detector hits) should have a good quality ($\chi^2/n_{dof} < 10$). At least one hit in the muon detector is required. An isolation criterion is applied to remove contributions from leptons originating from QCD events. Isolated muon candidates are selected if they fulfill the condition $I_{rel} < 0.20$. Here, I_{rel} is defined as the sum of transverse energy deposits from charged or neutral hadron and photon candidates, relative to the transverse momentum of the lepton candidate, inside a cone in $\eta - \phi$ space of $\Delta R = \sqrt{(\Delta\phi)^2 + (\Delta\eta)^2} \leq 0.3$ around the lepton candidate.

2.3.2. *Electron Selection.* Electron candidates are reconstructed using the particle-flow algorithm and must have a transverse momentum $p_T > 20$ GeV with a pseudo-rapidity $|\eta| < 2.4$. Electron candidates are further selected by applying a sophisticated set of identification criteria, such as requirements on track matching with the ECAL, a small amount of HCAL energy deposits relative to ECAL deposits in the same region, cluster shapes, tracker and calorimeter isolation, and distance requirements between two electron tracks [**23**]. Additionally, electron candidates are required to be isolated fulfilling $I_{rel} < 0.17$, defined as above.

2.4. Lepton pair selection

Events with at least two oppositely-charged leptons fulfilling the above selection criteria are accepted. If more than two oppositely-charged lepton candidates are reconstructed in the event, the one oppositely charged lepton candidate pair with the highest sum of the transverse momenta of the two lepton candidates is chosen. The event is then unambiguously classified as ee, $e\mu$, $\mu\mu$ depending on the flavor of the selected lepton pair (i.e. an event with three leptons, e.g. μ^+, μ^-, and e^+, will be assigned either to the $e\mu$ or the $\mu\mu$ channel, but not to both).

The invariant mass of the selected lepton pair, m_{ll}, is subject to the next selection steps and is required to be above 12 GeV in order to exclude low mass Drell-Yan resonances and QCD processes in all channels. Drell-Yan processes in the region of $m_{ll} > 50$ GeV are described well by the MadGraph MC. The Pythia Drell-Yan MC for $m_{ll} < 50$ GeV does not describe the data in the ee and $\mu\mu$ channel as illustrated in Figure 4.2. Therefore

this region is also excluded in these two channels. In the following, this step is referred to as the dilepton selection.

For the $t\bar{t}$ cross section measurement in the ee and $\mu\mu$ channel, Z^0 candidates are excluded (Z^0 veto), which fall into the invariant mass range of m_{ll} between 76 GeV and 106 GeV. For the Z^0 cross section measurement, this selection is inverted, such that the datasets for both measurements are statistically uncorrelated.

2.5. Jet and $\not\!\!E_{\mathrm{T}}$ selection

All following selection steps are applied for the $t\bar{t}$ cross section measurement only. Since most of the remaining background events to the $t\bar{t}$ signal originate from Drell-Yan processes and diboson production, which are not expected to have a high amount of hadronic activity, $t\bar{t}$ events can be disentangled from the background by requirements on jets and missing transverse energy.

Jets are reconstructed from the remaining particle-flow candidates, which are not selected in the lepton selection. The resolution of the jet energy in data has proven to be better than in MC [**33**]. Therefore it is increased in MC by 10% taking into account the relative p_T difference of generated and matched reconstructed jet.

Jets are required to fulfill certain kinematic and identification criteria. In order to reduce detector noise, the neutral, electromagnetic and hadronic fractions in the jet must be below 0.99. In addition, for jets with $|\eta| > 2.4$ the charged electromagnetic fraction must be lower than 0.99 [**26**].

Due to the kinematic constraints of the $t\bar{t}$ decay signature, at least two jets with $p_T > 30$ GeV and $|\eta| < 2.4$ are required. The jet multiplicity is shown in Figure 4.3.

Another characteristic feature of the $t\bar{t}$ signal is the presence of $\not\!\!E_{\mathrm{T}}$ due to the neutrinos produced in the $W^{\pm}$ decays. Therefore, selecting events with significant $\not\!\!E_{\mathrm{T}}$ allows suppressing Drell-Yan and QCD background contributions, where no real source of $\not\!\!E_{\mathrm{T}}$ is present. Therefore, events in the dimuon and dielectron channels are required to have a missing $E_T > 30$ GeV. The observed $\not\!\!E_{\mathrm{T}}$ is consistently reconstructed from particle-flow objects. No $\not\!\!E_{\mathrm{T}}$ selection is applied in the $e\mu$ channel. Missing E_T distributions for the ee, $\mu\mu$ and $e\mu$ channels are shown in Figure 4.4.

2.6. B-tagging

At least one of the jets is required to be identified as a b-quark jet. For this purpose, and algorithm is used, in which the large mass and lifetime of mesons containing b-quarks are exploited, requiring a displacement of the b-jet origin with respect to the primary vertex. As a discriminating variable, the significance of the impact parameter of the second track of the jet is used. The impact parameter (IP) is the distance between the track and the primary vertex at the point of the closest approach. The tracks are ordered in descending IP significance. The discriminator value of 1.7 is chosen such that an efficiency of about 80% at a mistag rate of 10% [**43**]. In Figure 4.5 the multiplicity of b-tagged jets is illustrated after the jet and $\not\!\!E_{\mathrm{T}}$ requirements are applied.

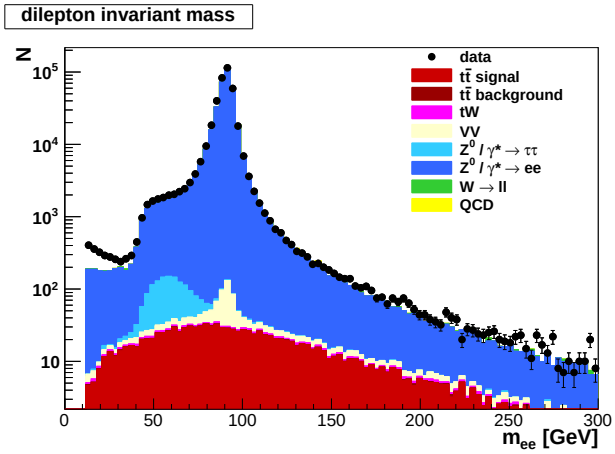

(a) ee channel

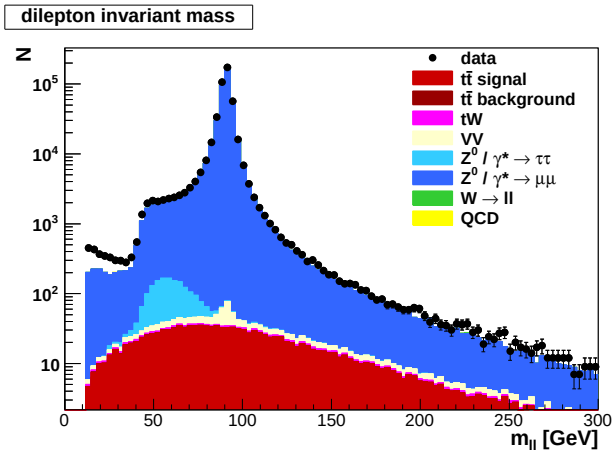

(b) $\mu\mu$ channel

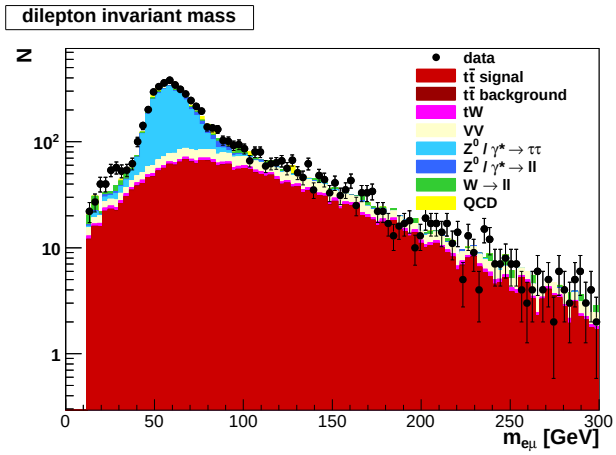

(c) $e\mu$ channel

Figure 4.2: Invariant mass of the lepton candidate pair after the removing low mass Drell-Yan-processes for the ee channel (a), the $\mu\mu$ channel (b), and the $e\mu$ channel (c). The data is shown in closed symbols. The red histogram represents the simulation of the $t\bar{t}$ production, the dark blue the prediction for the Z^0 production. The background contributions are shown in different colored histograms, as indicated in the legend.

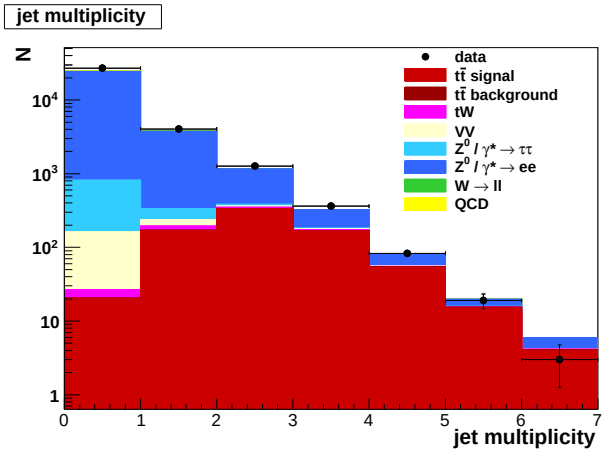

(a) ee channel

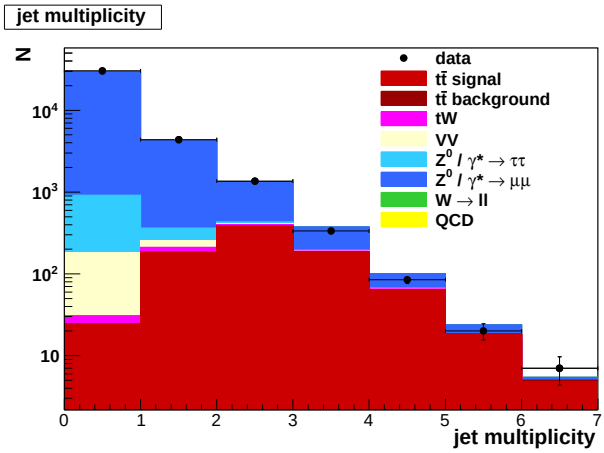

(b) $\mu\mu$ channel

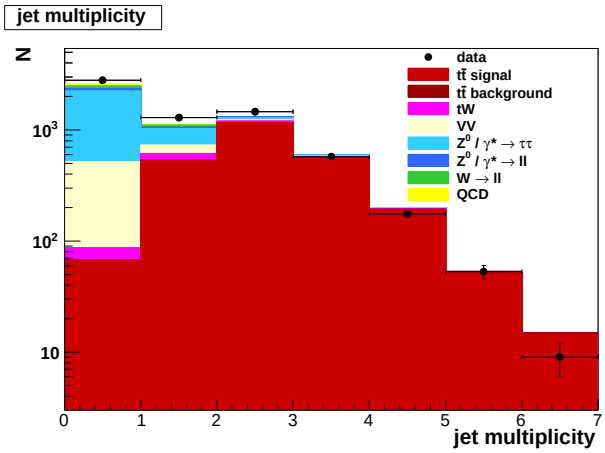

(c) $e\mu$ channel

Figure 4.3: Multiplicity of the selected jets which fulfill the identification and kinematic criteria ($p_T > 30$ GeV, $|\eta| < 2.4$) after the $t\bar{t}$ lepton selection for the ee channel (a), the $\mu\mu$ channel (b) and the $e\mu$ channel (c). The data is shown in closed symbols. The red histogram represents the simulation of the $t\bar{t}$ production, the dark blue the prediction for the Z^0 production. The background contributions are shown in different colored histograms, as indicated in the legend.

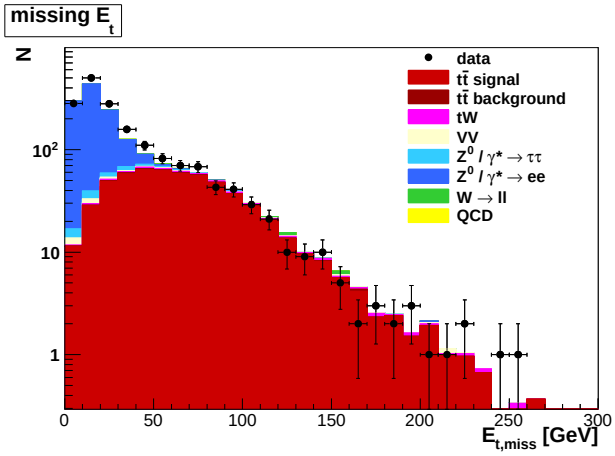

(a) ee channel

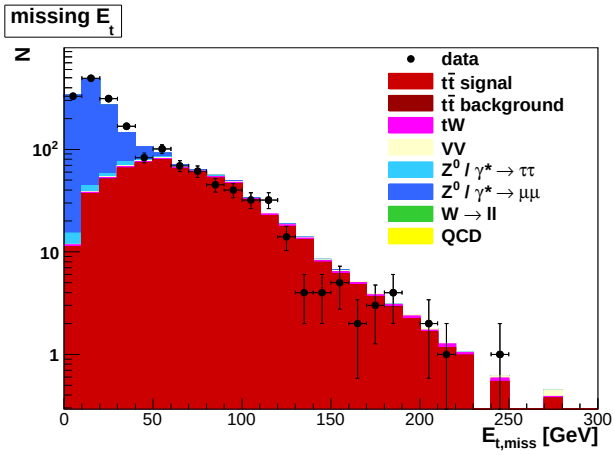

(b) $\mu\mu$ channel

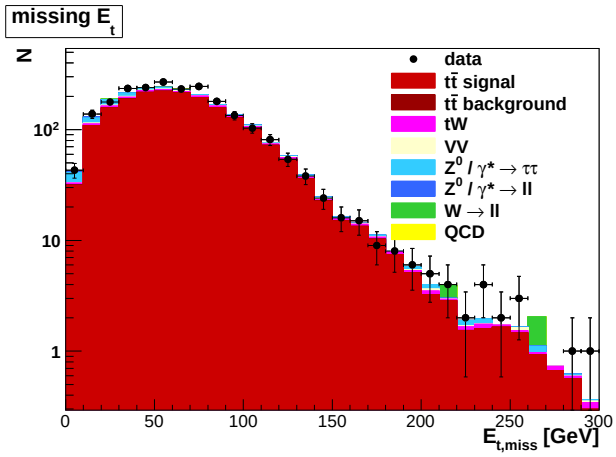

(c) $e\mu$ channel

Figure 4.4: Missing E_T after the requirement of at least two selected jets for the ee channel (a), the $\mu\mu$ channel (b) and the $e\mu$ channel (c). The data is shown in closed symbols. The red histogram represents the simulation of the $t\bar{t}$ production, the dark blue the prediction for the Z^0 production. The background contributions are shown in different colored histograms, as indicated in the legend.

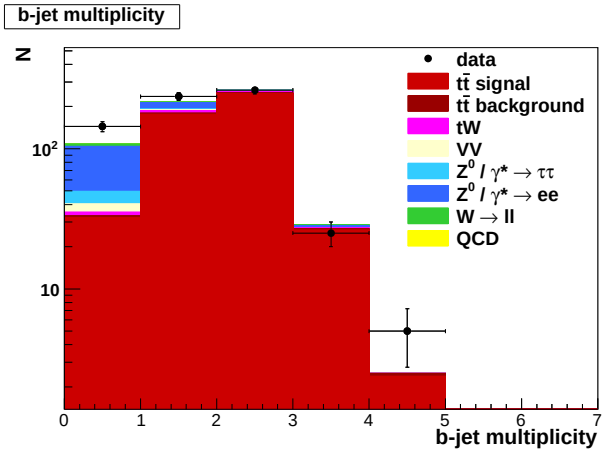

(a) ee channel

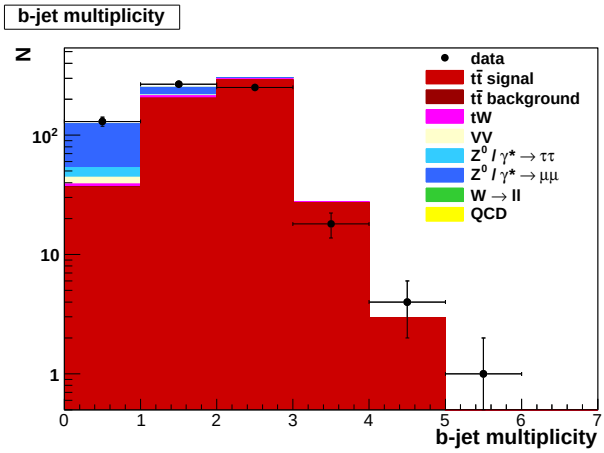

(b) $mu\mu$ channel

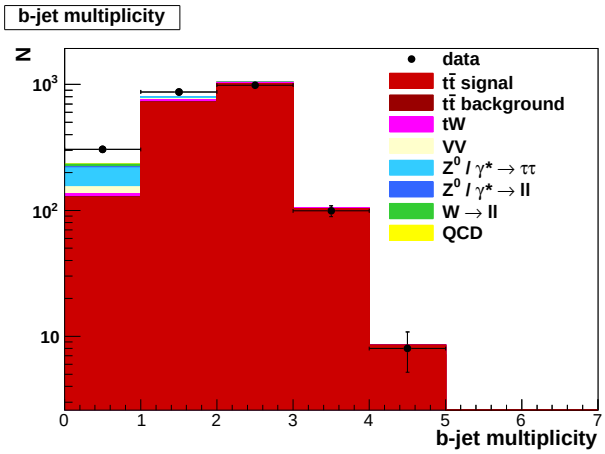

(c) $e\mu$ channel

Figure 4.5: Multiplicity of the selected b-tagged jets after the $\not\!\!E_{\mathrm{T}}$ requirement in the ee (a) and $\mu\mu$ channel (b) or the requirement of two selected jets ($e\mu$ channel (c)). The data is shown in closed symbols. The red histogram represents the simulation of the $t\bar{t}$ production, the dark blue the prediction for the Z^0 production. The background contributions are shown in different colored histograms, as indicated in the legend.

A summary of the selected events and simulated background contributions for each step starting from the dilepton requirement is given in Table 4.2, 4.3 and 4.4.

	dilepton	Z^0 selection	Z^0 veto	two jets	$\not\!\!E_{\mathrm{T}}$	b-tag
$t\bar{t}$ *signal*	1051	288	763	574	485	453
$t\bar{t}$ *background*	14	4	10	8	7	6
tW	67	18	50	19	16	14
VV	544	350	194	15	7	2
Z^0 / $\gamma* \rightarrow \tau\tau$	839	61	778	28	14	4
Z^0 / $\gamma* \rightarrow ee$	378464	350518	27946	939	81	27
$W \rightarrow ll$	155	37	118	11	7	2
QCD	454	271	183	0	0	0
MC sum	381589	351548	30041	1593	616	508
Data	389951±624	357215±598	32736±181	1732±42	672±26	528±23

Table 4.2: Summary of the selected events and simulated background contributions for the ee channel with statistical uncertainties for data at each selection step.

	dilepton	Z^0 selection	Z^0 veto	two jets	$\not\!\!E_{\mathrm{T}}$	b-tag
$t\bar{t}$ *signal*	1190	326	864	657	558	522
$t\bar{t}$ *background*	4	2	2	2	1	1
tW	76	20	56	22	18	16
VV	364	160	204	10	8	3
Z^0 / $\gamma* \rightarrow \tau\tau$	935	70	865	26	13	4
Z^0 / $\gamma* \rightarrow \mu\mu$	450389	417539	32850	1094	110	39
$W \rightarrow ll$	6	1	5	0	0	0
QCD	0	0	0	0	0	0
MC sum	452964	418118	34847	1810	709	585
Data	458933±677	422458±650	36475±191	1807±43	671±26	541±23

Table 4.3: Summary of the selected events and simulated background contributions for the $\mu\mu$ channel with statistical uncertainties for data at each selection step.

	dilepton	Z^0 veto	one jet	two jets	$\not\!\!E_{\mathrm{T}}$	b-tag
$t\bar{t}$ *signal*	2560	2560	2492	1963	1963	1837
$t\bar{t}$ *background*	21	21	20	17	17	15
tW	162	162	144	62	62	54
VV	569	569	139	25	25	7
Z^0 / $\gamma* \rightarrow \tau\tau$	2109	2109	392	94	94	31
Z^0 / $\gamma* \rightarrow ll$	154	154	38	8	8	2
$W \rightarrow ll$	195	195	62	14	14	4
QCD	117	117	10	0	0	0
MC sum	5887	5887	3298	2183	2183	1951
Data	6368±80	6368±80	3565±60	2272±48	2272±48	1967±44

Table 4.4: Summary of the selected events and simulated background contributions for the $e\mu$ channel with statistical uncertainties for data at each selection step.

3. Data-driven corrections

The limitations of the detector acceptance and resolution are described by the reconstruction efficiency, determined using MC simulation. The efficiency ϵ^{MC} is defined as the ratio of the number of events that are reconstructed and selected to the number of events that are originally generated. In general, it is estimated from the signal MC sample, but certain contributions are also obtained from data to improve the already generally good agreement between data and simulation. In most cases, a data-to-simulation correction factor $\rho_i = \epsilon_i^{data}/\epsilon_i^{MC}$ is applied to the efficiency estimate from simulation to correct it in a data-driven approach for a particular selection step i. The correction factor is introduced as an event weight, which is applied to the simulation at the corresponding step and can depend on the event topology.

3.1. Trigger efficiencies

One of the first event selection steps is the trigger decision. The trigger efficiency is estimated from data using independent triggers (cross-triggers) [**32**], which are ideally not correlated with the investigated dilepton trigger. In this analysis, $\not{E}_{\mathrm{T}}$ and jet high-level triggers[3] are used for this purpose. These triggers have a weak correlation to the dilepton triggers and provide sufficient statistics to keep the statistical uncertainty below 1%. On these datasets, the same event selection as described in section 2 is performed up to the full lepton identification (except for different HLT paths). Two selected lepton candidates according to the investigated dilepton trigger are required in the event (e.g. two electron candidates for the dielectron trigger). Events with more than two lepton candidates of the right flavor are not considered to avoid ambiguity. The fraction of these events is below 0.1%. The number of events passing this selection, N_{dilep}, and therefore containing a dilepton candidate, is then compared to the number of events also fulfilling the corresponding dilepton trigger constraints, N_{trig}. This results in a trigger efficiency ϵ_{trig} for the dilepton HLT according to Equation 4.1.

$$\epsilon_{trig} = \frac{N_{trig}}{N_{dilep}} \tag{4.1}$$

In MC, the simulated HLT efficiency can be determined by comparing the number of events before and after the trigger selection. To take into account possible correlations between the lepton candidate identification and the trigger response, the same event selection procedure as described above for data is applied to MC, except for the cross trigger requirement.

The correlation between both triggers is estimated from MC using a similar procedure as [**32**]. The dilepton trigger efficiency, $\epsilon^{MC}_{trig,ll}$, the cross-trigger trigger efficiency $\epsilon^{MC}_{trig,\times}$ and the combined trigger efficiency, $\epsilon^{MC}_{trig,\times,ll}$, is determined. The latter represents the efficiency for an event passing both trigger requirements simultaneously. For independent triggers, the ratio R_{trig} given in Equation 4.2 becomes 1.

[3] details: see appendix, Tables 5.11 and 5.12

A deviation of R_{trig} from 1 indicates a correlation of the triggers resulting in a systematic uncertainty which is conservatively estimated to be three times larger than the deviation. The statistical uncertainty is given by a binomial error (see Equation 4.3), $\Delta_{\epsilon_{trig}}$, due to the correlation between N_{trig} and N_{dilep}. The obtained efficiencies are listed in Table 4.5.

$$R_{trig} = \frac{\epsilon^{MC}_{trig,\times} \cdot \epsilon^{MC}_{trig,ll}}{\epsilon^{MC}_{trig,\times,ll}} \tag{4.2}$$

The kinematic properties of the leptons originating from $t\bar{t}$ and Z^0 decays are different, as can be seen in Figure 4.6. In order to take these differences into account, the efficiencies are obtained as a function of p_T and η of the lepton candidates. A large binning is chosen to keep the statistical uncertainty low.

$$\Delta^2_{stat.}(\epsilon_{trig}) = \frac{1 - \epsilon_{trig}}{N_{dilep}} \tag{4.3}$$

channel	R_{trig}	ϵ^{data}_{trig}	ϵ^{MC}_{trig}
ee	1.0015	$0.956 \pm 0.007(stat) \pm 0.005(sys)$	$0.986 \pm 0.001(stat) \pm 0.005(sys)$
$\mu\mu$	0.9985	$0.920 \pm 0.002(stat) \pm 0.005(sys)$	$0.956 \pm 0.001(stat) \pm 0.005(sys)$
$e\mu$	1.0002	$0.930 \pm 0.007(stat) \pm 0.001(sys)$	$0.947 \pm 0.001(stat) \pm 0.001(sys)$

Table 4.5: Trigger efficiencies ϵ_{trig} for the ee, $\mu\mu$ and $e\mu$ trigger and correlation factors R_{trig} determined with the cross trigger method for data and MC.

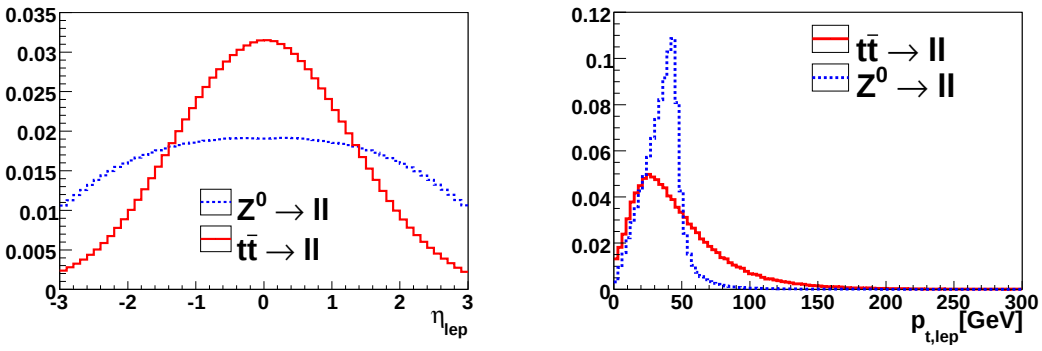

Figure 4.6: Kinematic distributions in pseudorapidity η and transverse momentum p_T for generated muons and electrons originating from a Z^0 or $t\bar{t}$ decay illustrated by the blue or red lines, respectively.

In order to account for the correlation between η_i and $p_{T,i}$ for each lepton candidate i, the efficiencies are determined double differentially in η_i and $p_{T,i}$, from which the single lepton trigger weights $s^{trig}_{l,i}(p_{T,i},\eta_i) = \epsilon^{data}_{trig,ll}(p_{T,i},\eta_i)/\epsilon^{MC}_{trig,ll}(p_{T,i},\eta_i)$ are obtained (see Tables 4.6, 4.7, and 4.8). Their statistic and systematic uncertainties are calculated as described above, but independently for each bin. The measured efficiencies are taken into account in the analysis by assigning an event weight, w_{trig}, to the simulated events, which dependends on the single lepton factors $s^{trig}_{l,i}$ according to Equation 4.4.

$$w_{trig}(p_{T,1},\eta_1,p_{T,2},\eta_2) = \sqrt{s^{trig}_{l,1}(p_{T,1}\eta_1)\cdot s^{trig}_{l,2}(p_{T,2},\eta_2)} \tag{4.4}$$

ϵ^{data}_{trig}	20 GeV $< p_T <$ 50 GeV	$p_T \geq$ 50GeV
-2.4 $< \eta \leq$ -1.2	0.983 ± 0.011	0.975 ± 0.014
-1.2 $< \eta \leq$ 1.2	0.973 ± 0.010	0.976 ± 0.006
1.2 $< \eta \leq$ 2.4	0.975 ± 0.016	0.971 ± 0.015
ϵ^{MC}_{trig}	20 GeV $< p_T <$ 50 GeV	$p_T \geq$ 50GeV
-2.4 $< \eta \leq$ -1.2	0.981 ± 0.002	0.991 ± 0.002
-1.2 $< \eta \leq$ 1.2	0.985 ± 0.001	0.985 ± 0.001
1.2 $< \eta \leq$ 2.4	0.987 ± 0.002	0.989 ± 0.002
$s^{trig}_{l,i}$	20 GeV $< p_T <$ 50 GeV	$p_T \geq$ 50GeV
-2.4 $< \eta \leq$ -1.2	1.002 ± 0.012	0.984 ± 0.014
-1.2 $< \eta \leq$ 1.2	0.987 ± 0.010	0.991 ± 0.006
1.2 $< \eta \leq$ 2.4	0.988 ± 0.016	0.982 ± 0.015

Table 4.6: Trigger efficiencies dependending on the lepton candidates transverse momentum p_T and pseudorapidity η for the ee trigger in data ϵ^{data}_{trig} and MC ϵ^{MC}_{trig}. For MC statistical uncertainties are shown, for data and the weight per lepton $s^{trig}_{l,i}$ the systematic uncertainty is also taken into account.

For events with more than two leptons passing the dilepton selection ($\approx$ 0.1 % of the events) the trigger efficiencies in data and MC are expected to be close to 1, therefore, a weight w_{trig} =1 is assigned. The influence of this approximation on the cross sections is considered to be negligible.

ϵ_{trig}^{data}	20 GeV $< p_T <$ 50 GeV	$p_T \geq$ 50GeV
-2.4 $< \eta \leq$ -1.2	0.935 $\pm$ 0.006	0.913 $\pm$ 0.021
-1.2 $< \eta \leq$ 1.2	0.954 $\pm$ 0.016	0.946 $\pm$ 0.004
1.2 $< \eta \leq$ 2.4	0.938 $\pm$ 0.006	0.932 $\pm$ 0.009
ϵ_{trig}^{MC}	20 GeV $< p_T <$ 50 GeV	$p_T \geq$ 50GeV
-2.4 $< \eta \leq$ -1.2	0.949 $\pm$ 0.003	0.944 $\pm$ 0.004
-1.2 $< \eta \leq$ 1.2	0.962 $\pm$ 0.002	0.961 $\pm$ 0.002
1.2 $< \eta \leq$ 2.4	0.951 $\pm$ 0.003	0.940 $\pm$ 0.004
$s_{l,i}^{trig}$	20 GeV $< p_T <$ 50 GeV	$p_T \geq$ 50GeV
-2.4 $< \eta \leq$ -1.2	0.985 $\pm$ 0.007	0.968 $\pm$ 0.021
-1.2 $< \eta \leq$ 1.2	0.992 $\pm$ 0.016	0.984 $\pm$ 0.004
1.2 $< \eta \leq$ 2.4	0.987 $\pm$ 0.007	0.991 $\pm$ 0.010

Table 4.7: Trigger efficiencies dependending on the lepton candidates transverse momentum p_T and pseudorapidity η for the $\mu\mu$ trigger in data ϵ_{trig}^{data} and MC ϵ_{trig}^{MC}. For MC statistical uncertainties are shown, for data and the weight per lepton $s_{l,i}^{trig}$ the systematic uncertainty is also taken into account.

ϵ_{trig}^{data}	20 GeV $< p_T <$ 50 GeV	$p_T \geq$ 50GeV
-2.4 $< \eta \leq$ -1.2	0.906 $\pm$ 0.022	0.918 $\pm$ 0.023
-1.2 $< \eta \leq$ 1.2	0.945 $\pm$ 0.008	0.929 $\pm$ 0.009
1.2 $< \eta \leq$ 2.4	0.923 $\pm$ 0.020	0.928 $\pm$ 0.020
ϵ_{trig}^{MC}	20 GeV $< p_T <$ 50 GeV	$p_T \geq$ 50GeV
-2.4 $< \eta \leq$ -1.2	0.923 $\pm$ 0.003	0.935 $\pm$ 0.003
-1.2 $< \eta \leq$ 1.2	0.956 $\pm$ 0.001	0.958 $\pm$ 0.001
1.2 $< \eta \leq$ 2.4	0.925 $\pm$ 0.003	0.919 $\pm$ 0.003
$s_{l,i}^{trig}$	20 GeV $< p_T <$ 50 GeV	$p_T \geq$ 50GeV
-2.4 $< \eta \leq$ -1.2	0.981 $\pm$ 0.021	0.982 $\pm$ 0.023
-1.2 $< \eta \leq$ 1.2	0.988 $\pm$ 0.009	0.970 $\pm$ 0.009
1.2 $< \eta \leq$ 2.4	0.998 $\pm$ 0.020	1.009 $\pm$ 0.020

Table 4.8: Trigger efficiencies dependending on the lepton candidates transverse momentum p_T and pseudorapidity η for the $e\mu$ trigger in data ϵ_{trig}^{data} and MC ϵ_{trig}^{MC}. For MC statistical uncertainties are shown, for data and the weight per lepton $s_{l,i}^{trig}$ the systematic uncertainty is also taken into account.

3.2. Lepton energy scale and resolution

After the Z^0 signal selection in the dielectron channel, a displacement of the Z^0 invariant mass peak position with respect to the PDG value [**61**] is observed, as illustrated in Figure 4.7. The deviation can be traced back to a known timing problem of the ECAL, which is not corrected in the reconstruction procedure of the datasets available for this analysis [**22**]. Therefore the electron energies are re-calibrated by adjusting their lepton energy scale (LES).

The energy of each electron candidate is proportional to the Z^0 invariant mass peak position m_Z^{peak} in the ee channel. This allows to derive an energy recalibration factor c_{les} for the electron candidates from the ratio of the precisely known Z^0 mass value m_Z^{pdg} [**61**] to the measured one in the ee channel: $c_{les} = m_Z^{pdg}/m_Z^{peak}$. In order to obtain m_Z^{peak}, a fit of the Z^0 invariant mass peak region is performed, such that m_Z^{peak} corresponds to the maximum of the fitting function[4].

The systematic uncertainty of the energy recalibration factor due to the Z^0 mass value m_Z^{pdg} [**61**] is negligible as compared to the systematic uncertainty of the fit. The latter is estimated as follows: each of the fitting parameters is varied within its uncertainties. Then, the energy recalibration factor is recalculated accordingly. Its maximum difference to the central value is taken as the uncertainty. The procedure is performed for each of the fitting parameters and resulting uncertainties are added in quadrature.

The energy recalibration factors for data and MC are determined using this method independently for electron candidates measured in the barrel region ($|\eta| < 1.479$) and in the endcaps ($|\eta| > 1.479$), as listed in Table 4.9. For both, the Z^0 invariant mass peak region together with the fit functions and the parameter variations are illustrated in Figure 4.8.

	m_Z^{peak} [GeV]	c_{les}
Barrel data	90.903 ± 0.040	1.0032 ± 0.0005
Barrel MC	91.287 ± 0.008	0.9989 ± 0.0001
Endcaps data	89.209 ± 0.641	1.0223 ± 0.0073
Endcaps MC	91.756 ± 0.063	0.9938 ± 0.0007

Table 4.9: Fitted positions of the Z^0 peak for electron candidates measured in the endcaps and in the barrel region and corresponding energy scaling factors c_{les} to recalibrate the ECAL measurement using the PDG Z^0 mass value [**61**].

[4]Breit-Wigner function convoluted with a Gaussian and a first order polynomial to account for detector effects

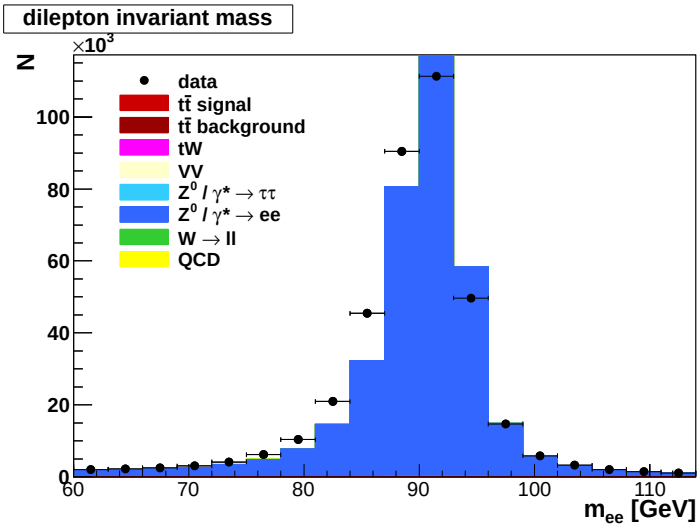

Figure 4.7: Invariant mass m_{ee} at the Z^0 peak after the dilepton selection in the ee channel without energy corrections. The data is shown in closed symbols. The red histogram represents the simulation of the $t\bar{t}$ production, the dark blue the prediction for the Z^0 production. The background contributions are shown in different colored histograms, as indicated in the legend.

Compared to the barrel region, less electron candidates deposit energy in the ECAL endcaps, which results in a larger uncertainty of the endcap energy recalibration factor determination. This is indicated by the large deviations of the varied functions with respect to the central values. However, the effect of this uncertainty on the cross section determination is small.

After adjusting the energy scale, there are remaining discrepancies originating from a different energy resolution in MC compared to the data, which are shown in Figure 4.9. In MC, the energy resolution can be adjusted by rescaling the electron candidates four-momenta $\mathbf{p}$ according to Equation 4.5, where f_{res} is the resolution factor, p_T^{reco} the candidates transverse momentum, p_T^{gen} the transverse momentum of the associated generated particle.

$$\mathbf{p}_{e,new} = \mathbf{p}_{e,old} \cdot \left(1 + (1 - f_{res}) \cdot \frac{p_T^{gen} - p_T^{reco}}{p_T^{reco}}\right) \tag{4.5}$$

To obtain the resolution correction factor, the normalized invariant mass of the selected electron candidate pair in the Z^0 invariant mass region in MC is compared to data and the differences are quantified by a χ^2 function defined in Equation 4.6, where $\Delta_{bin}^{MC,data}$ is the difference between data and MC in each bin, and $(\sigma_{bin}^{MC,data})^2$ is the quadratic sum

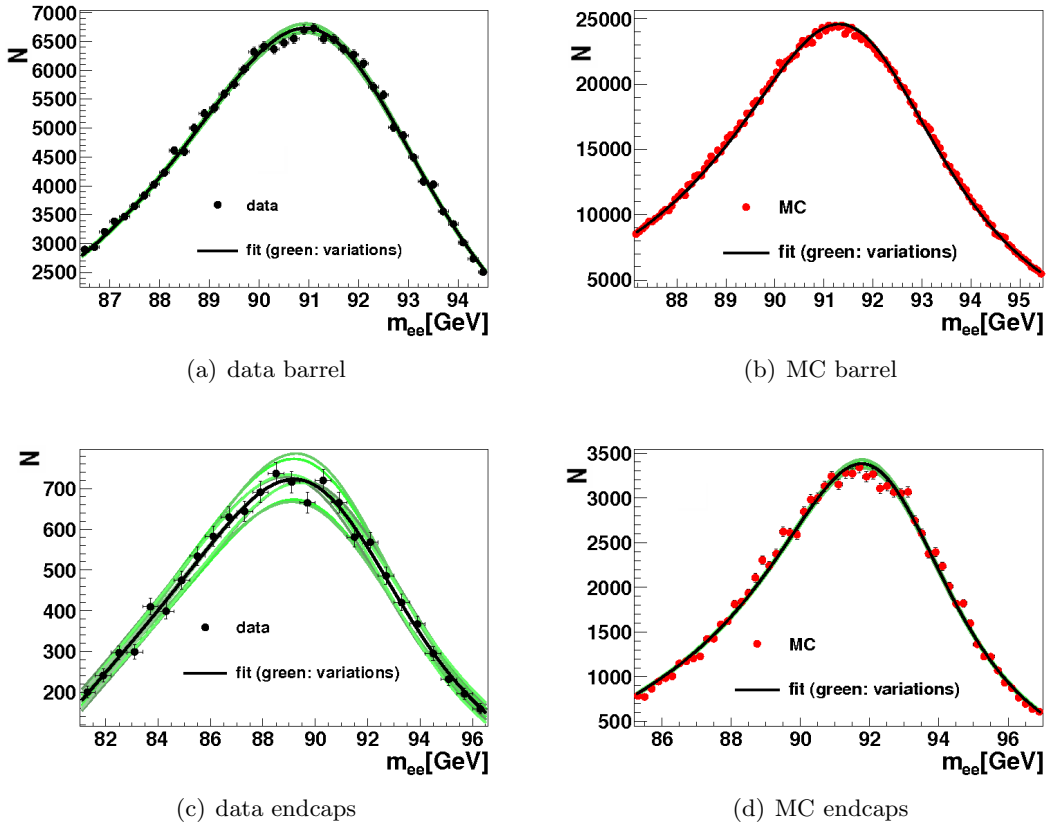

(a) data barrel (b) MC barrel

(c) data endcaps (d) MC endcaps

Figure 4.8: Fitted dielectron invariant mass m_{ee} at the Z^0 peak for data and MC after the dilepton selection in the ee channel for electron candidates measured in the barrel (a,b) and the endcaps (c,d). The data is shown in closed black symbols, the MC in closed red symbols. Black lines indicate the central fitting function and green lines variations of the fitting parameters.

of the statistical uncertainties in MC and data per bin.

$$\chi^2 = \sum_{bins} \left(\frac{\Delta_{bin}^{MC,data}}{\sigma_{bin}^{MC,data}} \right)^2 \tag{4.6}$$

The χ^2 function is calculated for different resolution factors between 0.1 and 1. It is fitted with a second order polynomial $\chi^2_{fit} = a(f_{res} - b)^2 + c$, where a, b and c are free parameters, to obtain the minimum, which corresponds to the best choice for f_{res}. This procedure is performed for the barrel and the endcap regions independently. The fitted χ^2 depending on f_{res} for both is shown in Figure 4.11. The resulting energy resolution factors are 0.788 ± 0.002 and 0.431 ± 0.003 for the barrel region or the endcap

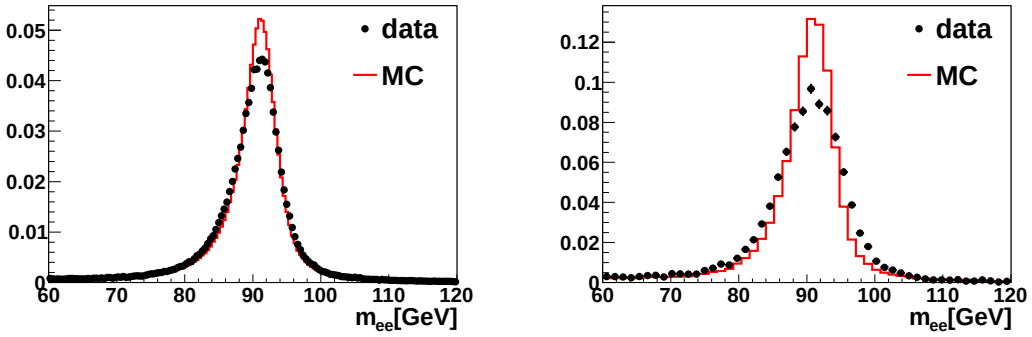

(a) Barrel (b) Endcaps

Figure 4.9: Normalized invariant mass distributions at the Z^0 peak reconstructed by electron candidates after the dilepton selection from the barrel region (a) and the endcaps (b). The red histogram indicates the simulation, the black closed symbols the data.

region, respectively. Their systematic uncertainty equals the uncertainty on the fitting parameter b. The application of these resolution correction factors results in a better agreement between data and MC. This is illustrated in Figure 4.10, in contrast to Figure 4.9, where no resolution correction is applied. Since the energy of the electron candidate influences a variety of variables, such as its p_T or isolation, the energy and resolution recalibration is performed before these variables are computed and electron candidates are selected.

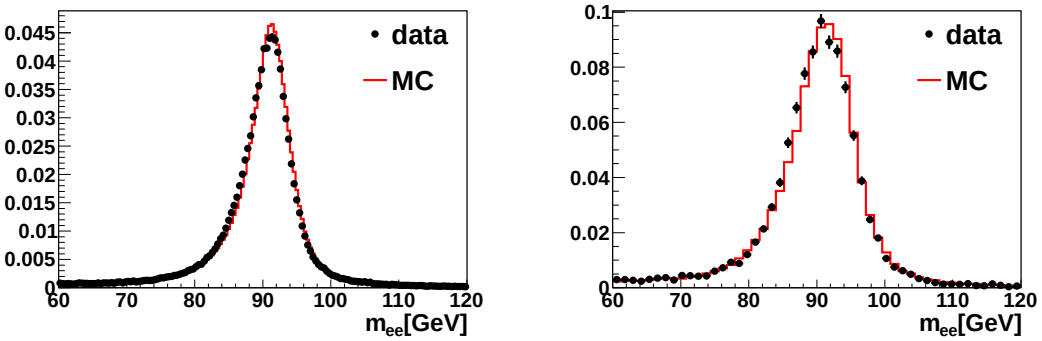

(a) barrel (f_{res} =0.788) (b) endcaps (f_{res} =0.431)

Figure 4.10: Normalized invariant mass distributions of the electron candidate pair after the dilepton selection at the Z^0 peak for electron candidates measured in the barrel (a) and endcap region (b) with energy resolution correction factors f_{res} applied. The red histogram indicates the simulation, the black closed symbols the data.

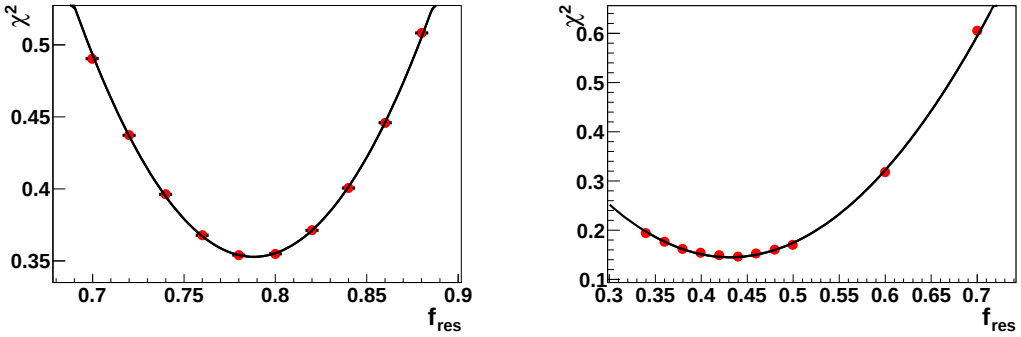

(a) Barrel (b) Endcaps

Figure 4.11: χ^2 (see Equation 4.6) for different resolution factors f_{res} to correct the ECAL energy resolution for the barrel region (a) and the endcaps (b). The red symbols represent calculated values, the black line the fit with a second order polynomial.

3.3. Lepton isolation

The isolation requirement for the lepton candidates is crucial in a high pileup environment with a large amount of tracks and energy deposits and its selection efficiency has to be precisely known. It is determined from data via a "tag-and-probe" method at the Z^0 invariant mass peak using ee and $\mu\mu$ events. Z^0 boson decays into 2 leptons are best suited for this purpose, since both leptons are isolated and affected by negligible background.

To select Z^0 candidate events, the full Z^0 selection as described in section 2.3 is applied, except for the isolation requirement. These events contain a lepton candidate pair with an invariant mass between 76 GeV and 106 GeV. Out of this pair, the lepton candidate with the highest p_T is chosen to be the *probe* candidate, while the other lepton candidate is required to fulfill the isolation criterion, to further reduce background. Thus, N_{sel} events are selected, which yield Z^0 candidate events and a negligible background contribution. This number is compared to the number of events, where the probe candidate fullfills the isolation requirement in addition N_{iso}, resulting in the isolation efficiency $\epsilon_{iso}^{data} = N_{iso}/N_{sel}$ per lepton candidate.

To account for correlations between the kinematic properties of the lepton candidates and the isolation efficiency, the latter is determined double-differentially in p_T and η of the probe candidate.

The same procedure is performed in MC to obtain the simulated isolation efficiencies ϵ_{iso}^{MC} and the data-driven correction factors per lepton $s_l^{iso} = \epsilon_{iso}^{data}/\epsilon_{iso}^{MC}$, which are listed in Table 4.10 for electron candidates and Table 4.11 for muon candidates. The corresponding statistical uncertainties are also shown.

Good agreement is found between data and MC, specially for muon candidates, for which correction factors are found to be almost 1.

ϵ_{iso}^{data}	-2.4 $< \eta \leq$ -1.2	-1.2 $< \eta \leq$ 1.2	1.2 $< \eta \leq$ 2.4
20 GeV $\leq p_T <$ 30 GeV	0.9510 ± 0.0032	0.9702 ± 0.0017	0.9522 ± 0.0031
30 GeV $\leq p_T <$ 40 GeV	0.9754 ± 0.0014	0.9851 ± 0.0005	0.9735 ± 0.0014
40 GeV $\leq p_T <$ 50 GeV	0.9860 ± 0.0007	0.9920 ± 0.0003	0.9869 ± 0.0007
50 GeV $\leq p_T$	0.9882 ± 0.0009	0.9929 ± 0.0003	0.9881 ± 0.0009
ϵ_{iso}^{MC}	-2.4 $< \eta \leq$ -1.2	-1.2 $< \eta \leq$ 1.2	1.2 $< \eta \leq$ 2.4
20 GeV $\leq p_T <$ 30 GeV	0.9568 ± 0.0010	0.9784 ± 0.0005	0.9599 ± 0.0009
30 GeV $\leq p_T <$ 40 GeV	0.9767 ± 0.0004	0.9887 ± 0.0002	0.9781 ± 0.0004
40 GeV $\leq p_T <$ 50 GeV	0.9869 ± 0.0002	0.9935 ± 0.0001	0.9875 ± 0.0002
50 GeV $\leq p_T$	0.9909 ± 0.0002	0.9945 ± 0.0001	0.9909 ± 0.0002
$s_{e,i}^{iso}$	-2.4 $< \eta \leq$ -1.2	-1.2 $< \eta \leq$ 1.2	1.2 $< \eta \leq$ 2.4
20 GeV $\leq p_T <$ 30 GeV	0.9939 ± 0.0035	0.9916 ± 0.0018	0.9920 ± 0.0035
30 GeV $\leq p_T <$ 40 GeV	0.9987 ± 0.0014	0.9963 ± 0.0006	0.9952 ± 0.0015
40 GeV $\leq p_T <$ 50 GeV	0.9991 ± 0.0007	0.9984 ± 0.0003	0.9994 ± 0.0007
50 GeV $\leq p_T$	0.9973 ± 0.0009	0.9984 ± 0.0004	0.9972 ± 0.0009

Table 4.10: Isolation efficiencies for data, ϵ_{iso}^{data}, and MC, ϵ_{iso}^{MC}, and resulting weights per lepton, $s_{e,i}^{iso}$, dependending on the lepton candidates transverse momentum p_T and pseudorapidity η for electron candidates. Only statistical uncertainties are shown.

ϵ_{iso}^{data}	-2.4 $< \eta \leq$ -1.2	-1.2 $< \eta \leq$ 1.2	1.2 $< \eta \leq$ 2.4
20 GeV $\leq p_T <$ 30 GeV	0.9776 ± 0.0019	0.9774 ± 0.0013	0.9779 ± 0.0019
30 GeV $\leq p_T <$ 40 GeV	0.9863 ± 0.0009	0.9899 ± 0.0004	0.9861 ± 0.0009
40 GeV $\leq p_T <$ 50 GeV	0.9905 ± 0.0005	0.9944 ± 0.0002	0.9905 ± 0.0005
50 GeV $\leq p_T$	0.9922 ± 0.0006	0.9948 ± 0.0003	0.9912 ± 0.0006
ϵ_{iso}^{MC}	-2.4 $< \eta \leq$ -1.2	-1.2 $< \eta \leq$ 1.2	1.2 $< \eta \leq$ 2.4
20 GeV $\leq p_T <$ 30 GeV	0.9777 ± 0.0006	0.9827 ± 0.0004	0.9791 ± 0.0006
30 GeV $\leq p_T <$ 40 GeV	0.9861 ± 0.0003	0.9907 ± 0.0001	0.9867 ± 0.0003
40 GeV $\leq p_T <$ 50 GeV	0.9910 ± 0.0001	0.9951 ± 0.0001	0.9907 ± 0.0002
50 GeV $\leq p_T$	0.9916 ± 0.0002	0.9950 ± 0.0001	0.9915 ± 0.0002
$s_{\mu,i}^{iso}$	-2.4 $< \eta \leq$ -1.2	-1.2 $< \eta \leq$ 1.2	1.2 $< \eta \leq$ 2.4
20 GeV $\leq p_T <$ 30 GeV	0.9999 ± 0.0020	0.9946 ± 0.0014	0.9988 ± 0.0020
30 GeV $\leq p_T <$ 40 GeV	1.0002 ± 0.0010	0.9992 ± 0.0005	0.9994 ± 0.0010
40 GeV $\leq p_T <$ 50 GeV	0.9995 ± 0.0005	0.9993 ± 0.0002	0.9999 ± 0.0005
50 GeV $\leq p_T$	1.0006 ± 0.0006	0.9998 ± 0.0003	0.9997 ± 0.0007

Table 4.11: Isolation efficiencies for data, ϵ_{iso}^{data}, and MC, ϵ_{iso}^{MC}, and resulting weights per lepton, $s_{e,i}^{iso}$, dependending on the lepton candidates transverse momentum p_T and pseudorapidity η for muon candidates. Only statistical uncertainties are shown.

The single lepton weights of the first and second lepton $s^{iso}_{l,1}$ $s^{iso}_{l,2}$ translate directly into an event weight for the isolation $w_{iso} = s^{iso}_{l,1} \cdot s^{iso}_{l,2}$, which is applied to each event in MC. Following [**32**], a conservative uncertainty of 2% per lepton for the $t\bar{t}$ measurement on the isolation is assigned taking into account differences in the isolation between $t\bar{t}$ and Z^0 decay.

3.4. B-tagging

From the differences in the b-tagging efficiencies in data and MC a scaling factor SF_b per event is derived. Efficiencies per jet in data and MC of $\epsilon^{data}_{b,jet} = 0.791(26)$ or $\epsilon^{MC}_{b,jet} = 0.821(1)$, respectively, are measured [**43**] for the b-tagging algorithm applied in this analysis. In events containing top-quark pair decays, two b-jets are expected. Therefore, the efficiencies per jet can be translated into an efficiency per event $\epsilon_{b,evt}$ to tag at least one b-jet as follows:

$$\epsilon_{b,evt} = 1 - (1 - \epsilon_{b,jet})^2 \tag{4.7}$$

The scaling factor per event, SF_b, is then given by $SF_b = \epsilon^{data}_{b,evt}/\epsilon^{MC}_{b,evt}$ and is found to be 0.988 ± 0.012.

4. Data-driven background estimation

In this section, the methods of background estimation for top-pair and Z^0 boson production, based on experimental data, are described.

4.1. Background to the Z^0 signal

The main background to the Z^0 signal are QCD processes, di-boson production and events containing leptonic decays of top-quark pairs. While the Z^0-signal events yield leptons of the same flavor in the final state, the background events appear with the same rate in same-flavor and mixed-flavor lepton pairs. Therefore, the data from the $e\mu$ channel can be used to determine the background to the Z^0 signal.

The Z^0 signal selection is performed on the dataset triggered by the $e\mu$ trigger. The same lepton candidate selection is applied as described in section 2.3. At the lepton candidate pair selection step, the pair is required to be an $e^{\pm}\mu^{\mp}$ candidate combination with an invariant mass falling into the Z^0 mass resonance range (76 GeV - 106 GeV). Then, the number of selected events, $N^{Z_r}_{e\mu}$, can be used to determine the background to the Z^0 signal in a particular decay channel, $N^{Z_{bg}}_{ll}$, as:

$$N^{Z_{bg}}_{ll} = 0.5 \cdot N^{Z_r}_{e\mu} \cdot c_l. \tag{4.8}$$

The factor 0.5 corrects for equal probability to have $e^-\mu^+$ and $e^+\mu^-$ in the final state. The factor c_l has to be applied to correct for differences in the reconstruction and selection efficiencies of electron, ϵ_e, and muon candidates, ϵ_μ.

Both correction factors, $c_e = \epsilon_e/\epsilon_\mu$ and $c_\mu = \epsilon_\mu/\epsilon_e$, can be determined from data using the selected Z^0 candidate events $N_{ee}^{Z_r}$ in the ee channel and $N_{\mu\mu}^{Z_r}$ in the $\mu\mu$ channel. Since these numbers are proportional to the corresponding single-lepton candidate selection efficiencies in quadrature, the correction factors can be written as:

$$c_e = \frac{\epsilon_e}{\epsilon_\mu} = \sqrt{\frac{N_{ee}^{Z_r}}{N_{\mu\mu}^{Z_r}}} = \frac{1}{c_\mu} \tag{4.9}$$

Taking into account all data-driven corrections the following numbers of events are selected in the Z^0 invariant mass region: $N_{ee}^{Z_r} = 391230$, $N_{\mu\mu}^{Z_r} = 422458$ and $N_{e\mu}^{Z_r} = 1109$. This results in the background estimates for the Z^0 signal in the ee channel $N_{ee}^{Z,bg} = 578$ and the $\mu\mu$ channel $N_{\mu\mu}^{Z_{bg}} = 532$ using Equation 4.8. The number of Z^0 signal event candidates $N_{ll}^{Z,data}$ is then given by $N_{ll}^{Z,data} = N_{ll}^{Z_r} - N_{ll}^{Z_{bg}}$, hence only determined from data.

4.2. Background to the $t\bar{t}$ signal

The dominant background to the $t\bar{t}$ signal in the ee and $\mu\mu$ channel are Drell-Yan processes. A data-driven approach to determine this background in both channels is taken by using the well known Z^0 invariant mass region as a control region for the normalization of the Drell-Yan MC contribution.

The normalization factor is obtained from the number of Z^0 events as determined from data. The Drell-Yan MC is scaled by $s_{DY,ll} = N_{ll}^{Z,data}/N_{ll}^{Z,MC}$.

The lepton candidate combinations ee, $\mu\mu$ and $e\mu$, selected as described above, are subjected to the top-pair event selection, applying the requirements of jets, $\not\!\!E_{\mathrm{T}}$ and a b-tagged jet. At each $t\bar{t}$ selection step, the scaling factor $s_{DY,ll}$ is recalculated. Assuming the shape of the Drell-Yan MC is modelled correctly, these factors are then used to rescale the Drell-Yan background contribution to the $t\bar{t}$ signal outside the Z^0 invariant mass region as well at the corresponding selection step. The obtained scaling factors for each step are listed in Tables 4.12 and 4.13 for the ee channel or the $\mu\mu$ channel, respectively.

step	$N_{e\mu}^{Z,data}$	$N_{ee}^{Z,data}$	$N_{ee}^{Z,MC}$	c_e	$s_{DY,ee}$
1 jet	758	56200	52466	0.92	1.06
2 jets	516	11542	10567	0.87	1.06
$E_{T,miss}$	438	1348	822	0.88	1.39
b-tag	398	660	299	0.94	1.56

Table 4.12: Selected events in the Z^0 invariant mass region in the $e\mu$ channel, $N_{e\mu}^{Z,data}$, and ee channel, $N_{ee}^{Z,data}$, simulated Drell-Yan contribution $N_{ee}^{Z,MC}$ in Z^0 region for each $t\bar{t}$ selection step and resulting correction (c_e) and scaling factors $s_{DY,ee}$ for the ee channel.

Figure 4.12 illustrates the effect of the scaling in the full e^+e^- candidate invariant mass region after all other $t\bar{t}$ selection requirements are applied. Without rescaling, the Drell-Yan background contribution is underestimated.

step	$N_{e\mu}^{Z,data}$	$N_{\mu\mu}^{Z,data}$	$N_{\mu\mu}^{Z,MC}$	c_e	$s_{DY,\mu\mu}$
1 jet	758	64549	61580	1.09	1.06
2 jets	516	13114	12420	1.15	1.03
$E_{T,miss}$	438	1486	983	1.11	1.28
b-tag	398	701	351	1.06	1.41

Table 4.13: Selected events in the Z^0 invariant mass region in the $e\mu$ channel, $N_{e\mu}^{Z,data}$, and $\mu\mu$ channel, $N_{\mu\mu}^{Z,data}$, simulated Drell-Yan contribution $N_{\mu\mu}^{Z,MC}$ in Z^0 region for each $t\bar{t}$ selection step and resulting correction (c_e) and scaling factors $s_{DY,\mu\mu}$ for the $\mu\mu$ channel.

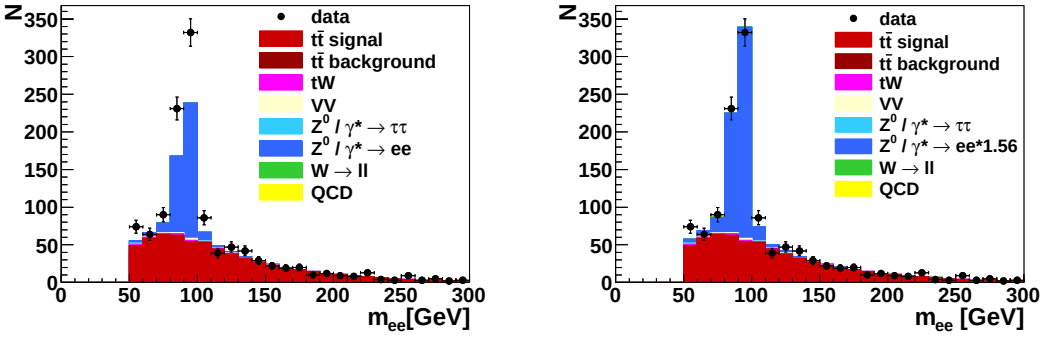

(a) Default

(b) Rescaled Drell-Yan MC

Figure 4.12: Invariant mass of the e^+e^- pair in the ee channel after all $t\bar{t}$ selection steps applied except for the Z^0 veto with without rescaling of the Drell-Yan contribution (a) and with a rescaled Drell-Yan contribution (b). The data is shown in closed symbols. The red histogram represents the simulation of the $t\bar{t}$ production, the dark blue the prediction for the Z^0 production. The background contributions are shown in different colored histograms, as indicated in the legend.

A summary of the selected events and simulated background contributions with all corrections applied is given in Tables 4.14, 4.15 and 4.16. Table 4.17 lists the numbers of signal events after background subtraction.

	dilepton	Z^0 selection	Z^0 veto	two jets	$\not\!\!E_{\mathrm{T}}$	b-tag
$t\bar{t}$ *signal*	1050	287	764	575	486	445
$t\bar{t}$ *background*	14	4	10	8	7	6
tW	65	17	48	18	16	13
VV	526	337	188	14	7	2
$Z^0 \,/\, \gamma* \,\rightarrow\, \tau\tau$	797	60	737	26	13	3
$Z^0 \,/\, \gamma* \,\rightarrow\, ee$	360678	332755	27923	981	114	41
$W \,\rightarrow\, ll$	148	36	112	10	6	2
QCD	438	262	176	0	0	0
MC sum	363716	333757	29959	1634	648	513
Data	391230±625	358523±599	32707±181	1740±42	675±26	532±23

Table 4.14: Summary of the selected events and simulated background contributions for ee channel including all corrections and scaling factors at each selection step. For data statistical errors are shown.

	dilepton	Z^0 selection	Z^0 veto	two jets	$\not\!\!E_{\mathrm{T}}$	b-tag
$t\bar{t}$ *signal*	1184	327	858	653	554	509
$t\bar{t}$ *background*	4	2	2	2	1	1
tW	73	19	54	21	18	15
VV	351	155	196	10	8	2
$Z^0 \,/\, \gamma* \,\rightarrow\, \tau\tau$	890	67	824	24	12	3
$Z^0 \,/\, \gamma* \,\rightarrow\, \mu\mu$	429814	398621	31194	1060	132	50
$W \,\rightarrow\, ll$	6	1	5	0	0	0
QCD	0	0	0	0	0	0
MC sum	432323	399190	33133	1770	726	581
Data	458931±677	422458±650	36473±191	1807±43	671±26	541±23

Table 4.15: Summary of the selected events and simulated background contributions for $\mu\mu$ channel including all corrections and scaling factors at each selection step. For data statistical errors are shown.

	dilepton	Z^0 veto	one jet	two jets	$\not\!\!E_{\mathrm{T}}$	b-tag
$t\bar{t}$ *signal*	2591	2591	2523	1988	1988	1826
$t\bar{t}$ *background*	21	21	20	17	17	15
tW	159	159	141	61	61	52
VV	557	557	136	24	24	7
$Z^0 \,/\, \gamma* \,\rightarrow\, \tau\tau$	2048	2048	378	90	90	28
$Z^0 \,/\, \gamma* \,\rightarrow\, ll$	150	150	37	7	7	2
$W \,\rightarrow\, ll$	192	192	60	14	14	4
QCD	117	117	10	0	0	0
MC sum	5835	5835	3305	2201	2201	1934
Data	6409±80	6409±80	3575±60	2275±48	2275±48	1968±44

Table 4.16: Summary of the selected events and simulated background contributions for $e\mu$ channel including all corrections and scaling factors at each selection step. For data statistical errors are shown.

channel	N^{Z}_{sig}	$N^{t\bar{t}}_{sig}$
ee	357945	464
$\mu\mu$	421926	468
$e\mu$		1860

Table 4.17: Signal events passing the whole Z^0 and $t\bar{t}$ event selection N^{Z}_{sig} or $N^{t\bar{t}}_{sig}$, respectively, for the ee, $\mu\mu$, and $e\mu$ channel.

5. Determination of efficiencies

The efficiencies of the full selection procedure for the Z^0 ($t\bar{t}$) events, ϵ^{Z}_{tot} ($\epsilon^{t\bar{t}}_{tot}$), are determined as ratios of the number of selected events to the number of generated events in the corresponding channel using simulation, according to Equation 4.10.

$$\epsilon_{tot} = \frac{N^{corr}_{reco,sel}}{N_{gen}} \tag{4.10}$$

No generator pre-selection is performed, therefore, the efficiency definition includes not measured phasespace and accounts for the detector acceptance. All previously described correction factors are applied as event weights or scaling factors, respectively.

As a result the corrected number of reconstructed and selected events, $N^{corr}_{reco,sel}$, is used for the efficiency determination. In Table 4.18 the total efficiencies for both decays and all channels are summarized.

channel	$N^{corr}_{reco,sel}$	N_{gen}	ϵ_{tot}
$t\bar{t}$ ee	8339	64204	0.130
$t\bar{t}$ $\mu\mu$	9534	62655	0.152
$t\bar{t}$ $e\mu$	34213	127270	0.269
Z^0 ee	3328549	11202295	0.297
Z^0 $\mu\mu$	3993560	11200026	0.357

Table 4.18: Total efficiencies, ϵ_{tot}, for all measured channels of the $t\bar{t}$ and Z^0 decay (ee, $\mu\mu$ and $e\mu$) derived from the number of reconstructed and selected events corrected by efficiencies from data, $N^{corr}_{reco,sel}$, and the number of generated events, N_{gen}, in the whole phasespace.

6. Systematic uncertainties

In order to estimate the systematic uncertainty of the measured cross sections originating from a particular source, the parameters, defining the particular error source, are varied and the whole selection and efficiency determination is repeated with all corrections applied. In case of the uncertainties due to non perfect detector modelling, such as, pileup effects, isolation and trigger efficiencies, energy scales and resolutions, also the effect on the background is re-evaluated. Theory uncertainties, such as matching and momentum scale, PDF and top mass variations, are taken into account for the total efficiencies. Their influence on the background is estimated separately.

6.1. Jet energy scale

The jet quantities only affect the $t\bar{t}$ analysis. The uncertainty due to the jet energy scale is determined by varying the jet energy scale dependent on the jets p_T and η within the uncertainties estimated in [**40**]. These variations are of the order of a few percent. The influence of this uncertainty on the $t\bar{t}$ cross sections and, in turn, on the ratios of the $t\bar{t}$ to the Z^0 cross section is listed in Table 4.19.

channel	$\Delta_{jes}(\sigma_{t\bar{t}})$	$\Delta_{jes}\left(\frac{\sigma_{t\bar{t}}}{\sigma_Z}\right)$
ee	-1.7% $+2.8\%$	-1.7% $+2.8\%$
$\mu\mu$	-0.8% $+1.6\%$	-0.8% $+1.6\%$
$e\mu$	-2.0% $+2.5\%$	

Table 4.19: Systematic uncertainties of the $t\bar{t}$ cross section determination and the cross section ratio measurement caused by uncertainties on the jet energy scale $\Delta_{jes}(\sigma_{t\bar{t}})$ or $\Delta_{jes}\,(\sigma_{t\bar{t}}/\sigma_Z)$, respectively, for upward (first value) and downward (second value) variation. Shown are all studied channels (ee, $\mu\mu$ and $e\mu$).

6.2. Jet energy resolution

The jet energy resolution uncertainty [**40**] is applied to the default resolution, dependent on the jets pseudorapidity η. For $|\eta| < 1.5$ the uncertainty is 10%, for $1.5 \leq |\eta| < 2.0$ 15%, and for $2.0 \leq |\eta|$ 20%. The jet energy resolution is varied within these ranges resulting in the uncertainties on the $t\bar{t}$ cross section and the $t\bar{t}$ / Z^0 cross section ratio, as listed in Table 4.20.

channel	$\Delta_{jer}(\sigma_{t\bar{t}})$	$\Delta_{jer}\left(\frac{\sigma_{t\bar{t}}}{\sigma_Z}\right)$
ee	$+1.1\%$ -0.6%	$+1.1\%$ -0.6%
$\mu\mu$	$+0.7\%$ -0.6%	$+0.7\%$ -0.6%
$e\mu$	$+0.9\%$ -1.2%	

Table 4.20: Systematic uncertainties of the $t\bar{t}$ cross section measurement and determination of the cross section ratio $\Delta_{jer}(\sigma_{t\bar{t}})$ or $\Delta_{jer}\,(\sigma_{t\bar{t}}/\sigma_Z)$, respectively, caused by uncertainties of the jet energy resolution for upward (first value) and downward (second value) variation. Shown are all studied channels (ee, $\mu\mu$ and $e\mu$).

6.3. Electron energy scale and resolution

Systematic uncertainties of the cross sections and their ratio due to the electron energy scale and resolution are determined by varying both within their uncertainties. The energy scale for barrel electron candidates and the endcap electron candidates is varied simultaneously. The same is done for the electron energy resolution. The variation of the energy resolution affects all channels by less than 0.1%. In Table 4.21 the influence of the electron energy scale is listed. The $\mu\mu$ channel is not sensitive to the electron energy recalibration.

channel	$\Delta_{les}(\sigma_Z)$	$\Delta_{les}(\sigma_{t\bar{t}})$	$\Delta_{les}\left(\frac{\sigma_{t\bar{t}}}{\sigma_Z}\right)$
ee	0.1% -0.1%	$+0.3\%$ -0.7%	$+0.3\%$ -0.7%
$e\mu$		$+0.2\%$ -0.1%	

Table 4.21: Systematic uncertainties for the measurement of the Z^0 and $t\bar{t}$ production cross section as well as their ratio $\Delta_{les}(\sigma_Z)$, $\Delta_{les}(\sigma_{t\bar{t}})$ or $\Delta_{les}\,(\sigma_{t\bar{t}}/\sigma_Z)$, respectively,due to variations of the electron energy scale for the ee and $e\mu$ channels. For each contribution the first value corresponds to an upward variation of the energy scale, the second value to a downward variation.

6.4. Pileup

As described in section 2.2 the vertex multiplicity in MC is adjusted to the data. To estimate the uncertainties due to the reweighting, the mean of the reweighted vertex

multiplicity is shifted by a value of ± 0.6. As shown in Figure 4.13 this procedure accounts for differences in data compared to the simulation.

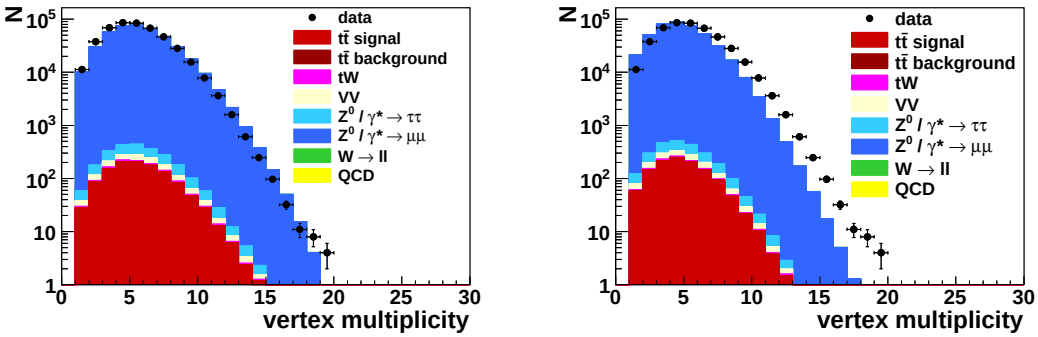

(a) shifted up (b) shifted down

Figure 4.13: Vertex multiplicity after the dilepton selection step in the $\mu\mu$ channel shifted up by 0.6 (a) and down by 0.6 (b). The data is shown in closed symbols. The red histogram represents the simulation of the $t\bar{t}$ production, the dark blue the prediction for the Z^0 production. The background contributions are shown in different colored histograms, as indicated in the legend.

The influence of this variation on the cross sections and their ratio is listed in Table 4.22. Here, a small correlation between the effect of the vertex multiplicity variation on the $t\bar{t}$ cross section and the Z^0 cross section results in a partial cancellation in the cross section ratio (see Table 4.22).

channel	$\Delta_{PU}(\sigma_Z)$	$\Delta_{PU}(\sigma_{t\bar{t}})$	$\Delta_{PU}\left(\frac{\sigma_{t\bar{t}}}{\sigma_Z}\right)$
ee	$+0.8\%$ -2%	$+0.2\%$ -0.2%	-0.7% $+2\%$
$\mu\mu$	$+0.6\%$ -1.7%	$+0.3\%$ -0.3%	$+1.4\%$ -0.3%
$e\mu$		$+0.4\%$ -0.5%	

Table 4.22: Systematic uncertainties for the measurement of the Z^0 and $t\bar{t}$ production cross section as well as their ratio $\Delta_{PU}(\sigma_Z)$, $\Delta_{PU}(\sigma_{t\bar{t}})$ or $\Delta_{PU}\left(\sigma_{t\bar{t}}/\sigma_Z\right)$, respectively, due to uncertainties of the pileup reweighting in the ee $\mu\mu$ and $e\mu$ channels for upward (first value) and downward (second value) variation.

6.5. Trigger efficiencies

As described in section 3.1 the trigger efficiencies are determined double differentially in transverse momentum p_T and pseudorapidity η of the lepton candidates. Two different methods are used to obtain the uncertainty on the cross sections and on the cross-section ratio. For the individual cross section determination procedure the efficiency in

all bins is varied simultaneously up or down within its uncertainties. To determine the maximum remaining influence of the trigger efficiency uncertainties on the cross-section ratio a different approach is taken. The efficiency is varied upwards in the kinematic range of the leptons, where events mostly originate from Z^0 decays. Simultaneously, the efficiency in bins where $t\bar{t}$ decays are dominant is varied down and vice versa. Table 4.23 lists the resulting uncertainties.

channel	$\Delta_{trig}(\sigma_Z)$	$\Delta_{trig}(\sigma_{t\bar{t}})$	$\Delta_{trig}\left(\frac{\sigma_{t\bar{t}}}{\sigma_Z}\right)$
ee	-1.2% $+1.0\%$	-1.3% $+1.3\%$	$+0.6\%$ -0.4%
$\mu\mu$	-0.8% $+1.1\%$	-1.2% $+1.2\%$	$+0.2\%$ -0.3%
$e\mu$		-1.3% $+1.3\%$	

Table 4.23: Systematic uncertainties for the measurement of the Z^0 and $t\bar{t}$ production cross section as well as their ratio $\Delta_{trig}(\sigma_Z)$, $\Delta_{trig}(\sigma_{t\bar{t}})$ or $\Delta_{trig}\left(\sigma_{t\bar{t}}/\sigma_Z\right)$, respectively, due to trigger efficiencies for the ee $\mu\mu$ and $e\mu$ channel. For each contribution the first value corresponds to an upward variation of the trigger efficiency, the second value to a downward variation.

6.6. Top mass, b-tagging efficiency and isolation efficiency

To estimate the influence of the top-mass value on the $t\bar{t}$ cross section measurement, alternative MC simulations are performed, in which the top mass is varied from 169.5 GeV to 175.5 GeV. The details of the simulation are given in the appendix, Table 5.13. The resulting uncertainties on the cross section determination are listed in Table 4.24.

channel	$\Delta_{m_t}(\sigma_{t\bar{t}})$	$\Delta_{m_t}\left(\frac{\sigma_{t\bar{t}}}{\sigma_Z}\right)$
ee	-5.6% $+1.7\%$	-5.6% $+1.7\%$
$\mu\mu$	-0.8% $+1.6\%$	-0.8% $+1.6\%$
$e\mu$	-1.5% $+2.2\%$	

Table 4.24: Systematic uncertainties for the measurement of the Z^0 and $t\bar{t}$ production cross section as well as their ratio $\Delta_{m_t}(\sigma_Z)$, $\Delta_{m_t}(\sigma_{t\bar{t}})$ or $\Delta_{m_t}\left(\sigma_{t\bar{t}}/\sigma_Z\right)$, respectively, due to variations of the top-mass value for the ee $\mu\mu$ and $e\mu$ channels. For each contribution the first value corresponds to an upward variation of the top-mass value to 175.5 GeV, the second value to a downward variation to 169.5 GeV.

The uncertainty of the the b-tagging scale factor of 1.2% (see sec. 2.5) and the isolation of 4% directly translates to an uncertainty on the efficiency and, in turn, the $t\bar{t}$ cross section in all channels. The influence of the isolation efficiency uncertainty on the Z^0 cross section is below 0.1% for all channels and therefore neglected.

6.7. Matching and momentum scale uncertainties

Uncertainties due to the choice of the matching scale and the momentum scale, Q^2, in simulations are determined using signal $t\bar{t}$ and Z^0 MC samples, in which the matching scale or Q^2 is varied, respectively[5]. The uncertainty due to the choice of Q^2 on generator level is studied by increasing and decreasing it by a factor of 4 with respect to the default value [**60**]. Resulting effects on the cross sections are listed in Tables 4.25 and 4.26.

The effect of the matching scale which influences the ratio of jet production on matrix element level to parton showering is studied by varying the scale by a factor of two up and down with respect to the default value of 20 GeV. Uncertainties due to initial state and final state radiation modelling are covered by these variations [**32**].

channel	$\Delta_{Q^2}(\sigma_Z)$	$\Delta_{Q^2}(\sigma_{t\bar{t}})$	$\Delta_{Q^2}\left(\frac{\sigma_{t\bar{t}}}{\sigma_Z}\right)$
ee	-2.7% $+1.9\%$	-3.8% -4.0%	-1.2% -5.7%
$\mu\mu$	-3.0% $+1.6\%$	$+2.2\%$ -2.4%	$+5.4\%$ -4.0%
$e\mu$		$+0.8\%$ $+0.2\%$	

Table 4.25: Systematic uncertainties for the measurement of the Z^0 and $t\bar{t}$ production cross section as well as their ratio $\Delta_{ms}(\sigma_Z)$, $\Delta_{ms}(\sigma_{t\bar{t}})$ or $\Delta_{ms}\left(\sigma_{t\bar{t}}/\sigma_Z\right)$, respectively, due to variations of the Q^2 scale for the ee $\mu\mu$ and $e\mu$ channels.For each contribution the first value corresponds to an upward variation of Q^2, the second value to a downward variation.

channel	$\Delta_{ms}(\sigma_Z)$	$\Delta_{ms}(\sigma_{t\bar{t}})$	$\Delta_{ms}\left(\frac{\sigma_{t\bar{t}}}{\sigma_Z}\right)$
ee	-1.0% -1.3%	-2.3% -5.4%	-1.3% -4.2%
$\mu\mu$	-0.6% -0.7%	$+3.8\%$ -0.4%	$+4.4\%$ $+0.3\%$
$e\mu$		$+0.3\%$ -1.5%	

Table 4.26: Systematic uncertainties for the measurement of the Z^0 and $t\bar{t}$ production cross section as well as their ratio $\Delta_{ms}(\sigma_Z)$, $\Delta_{ms}(\sigma_{t\bar{t}})$ or $\Delta_{ms}\left(\sigma_{t\bar{t}}/\sigma_Z\right)$, respectively, due to variations of the matching scale for the ee $\mu\mu$ and $e\mu$ channels.For each contribution the first value corresponds to an upward variation of the matching scale, the second value to a downward variation.

6.8. Background uncertainties

After the full $t\bar{t}$ signal selection, the remaining background amounts to about 10% in the ee and the $\mu\mu$ channels and to about 5% in the $e\mu$ channel. Following the CMS prescription [**27**], the background uncertainty is estimated by varying the normalization

[5] details: see appendix, Table 5.14

of each sample individually. The corresponding effects on the cross section are added in quadrature.

The Drell-Yan background normalization is varied by ±50% the normalization of the other contributions by ±30%. In Table 4.27 the influence of these variations on the $t\bar{t}$ cross section are summarized.

After the Z^0 selection, the background under the Z^0 peak accounts to less than 0.3%. An uncertainty of ±100% is assigned to this background in both channels.

background	ee	$\mu\mu$	$e\mu$
$t\bar{t}$ *background*	0.4%	0.1%	0.3%
tW	0.9%	1.0%	0.8%
VV	0.1%	0.1%	0.2%
Z^0 / $\gamma*$ $\rightarrow$ $\tau\tau$	0.2%	0.2%	0.5%
Z^0 / $\gamma*$ $\rightarrow$ ll	4.3%	5.3%	0.1%
W $\rightarrow$ ll	0.1%	0.1%	0.1%
QCD	0.1%	0.1%	0.1%
total	4.4%	5.4%	1.0%

Table 4.27: Relative uncertainties due to background modelling for the $t\bar{t}$ cross section in the ee, $\mu\mu$, and $e\mu$ channels for each background contribution.

6.9. PDF uncertainties

In MC, the proton structure is described by the CTEQ6 [**62**] parton density functions. This PDF contains 41 eigenvectors. Set S_0 corresponds to the central PDF and sets $S_1 - S_{41}$ are the eigenvectors of uncertainties. Estimation of the uncertainty of the cross section due to PDF variations by repeating the simulation for each eigenvector v is not feasible. Instead, a reweighting of the events according to [**47**] is performed with the weights calculated as:

$$w_{pdf,v}(n) = \frac{f_1(x_1(n), Q(n); S_v) \cdot f_2(x_2(n), Q(n); S_v)}{f_1(x_1(n), Q(n); S_0) \cdot f_2(x_2(n), Q(n); S_0)} \tag{4.11}$$

where $w_{pdf,v}(n)$ is the weight for event n, $f_i(x_i(n), Q(n); S_v)$ the probability of finding a parton i in the proton carrying a momentum fraction $x_i(n)$ of the proton at the momentum scale of $Q(n)$ of the interaction. These weights are applied in addition to all other corrections and the full event selection is performed on the signal MC samples.

The efficiency for each eigenvector is recalculated as follows:

$$\epsilon_{tot,v} = \frac{N^{corr}_{sel,v}}{\sum_{n}^{N_{gen}} w_{pdf,v}(n)} \tag{4.12}$$

taking into account the number of selected events with all corrections and the PDF weight applied, $N^{corr}_{sel,v}$, for each set v and the number of generated events N_{gen}. The total systematic uncertainty on the efficiency, Δ_{pdf}, is determined using Equation 4.13 following the CTEQ recommendation [**62**]. Since for the ratio of the $t\bar{t}$ to the Z^0 cross section the ratio of the efficiencies $\epsilon^{Z}_{tot}/\epsilon^{t\bar{t}}_{tot}$ is the relevant quantity, its PDF uncertainty is computed using Equation 4.14 to take into account possible correlations. The resulting effects on the cross sections are listed in Table 4.28.

$$\Delta_{pdf}(\epsilon_{tot}) = \pm\frac{1}{2}\sqrt{\sum_{v=1}^{20}\left(\epsilon_{tot,2v-1} - \epsilon_{tot,2v}\right)^2} \tag{4.13}$$

$$\Delta_{pdf}\left(\frac{\epsilon^{Z}_{tot}}{\epsilon^{t\bar{t}}_{tot}}\right) = \pm\frac{1}{2}\sqrt{\sum_{v=1}^{20}\left(\frac{\epsilon^{Z}_{tot,2v-1}}{\epsilon^{t\bar{t}}_{tot,2v-1}} - \frac{\epsilon^{Z}_{tot,2v}}{\epsilon^{t\bar{t}}_{tot,2v}}\right)^2} \tag{4.14}$$

channel	$\Delta_{pdf}(\sigma_Z)$	$\Delta_{pdf}(\sigma_{t\bar{t}})$	$\Delta_{pdf}\left(\frac{\sigma_{t\bar{t}}}{\sigma_Z}\right)$
ee	1.8%	0.4%	1.8%
$\mu\mu$	1.7%	0.4%	1.7%
$e\mu$		0.5%	

Table 4.28: Systematic uncertainties for the measurement of the Z^0 and $t\bar{t}$ production cross section as well as their ratio $\Delta_{pdf}(\sigma_Z)$, $\Delta_{pdf}(\sigma_{t\bar{t}})$ or $\Delta_{pdf}\left(\sigma_{t\bar{t}}/\sigma_Z\right)$, respectively, due to variations of the PDF parameters in the ee $\mu\mu$ and $e\mu$ channels.

6.10. Branching ratios

Based on the branching ratios provided by the PDG [**61**] for the leptonic $W^{\pm}$ decay, $BR_{W\to l\nu}$, the tau decay to electrons, $BR_{\tau\to\nu_\tau e\nu_e}$, and muons, $BR_{\tau\to\nu_\tau\mu\nu_\mu}$, the branching fraction for the $t\bar{t}$ decay in the ee and $\mu\mu$ channel $BR_{t\bar{t}\to X\to l^+l^-}$ is calculated as:

$$BR_{t\bar{t}\to X\to l^+l^-} = \left(BR_{W\to l\nu}\cdot\left(1 + BR_{\tau\to l\nu_l\nu_\tau}\right)\right)^2 \tag{4.15}$$

In the $e\mu$ channel, the branching ratio is given in Equation 4.16. The resulting branching fractions (and those for the dileptonic Z^0 decays [**61**]) are listed in Table 4.29 including their uncertainties.

$$BR_{t\bar{t}\to X\to e^{\pm}\mu^{\mp}} = 2 \cdot \sqrt{BR_{t\bar{t}\to X\to e^{+}e^{-}} \cdot BR_{t\bar{t}\to X\to \mu^{+}\mu^{-}}} \tag{4.16}$$

decay	BR	$\Delta_{BR}(\sigma)$
$Z^0 \to e^+e^-$	3.363%	0.1%
$Z^0 \to \mu^+\mu^-$	3.366%	0.2%
$t\bar{t} \to X \to e^+e^-$	1.616%	3.4%
$t\bar{t} \to X \to \mu^+\mu^-$	1.668%	2.0%
$t\bar{t} \to X \to e^{\pm}\mu^{\mp}$	3.284%	2.3%

Table 4.29: Uncertainties of the measured cross section of Z^0 production and $t\bar{t}$ production $\Delta_{BR}(\sigma)$ due to uncertainties of the branching ratios BR for the ee $\mu\mu$ and $e\mu$ channels.

6.11. Luminosity

The uncertainty due to the luminosity determination enters the cross-section determination as a normalization. The current value of the luminosity uncertainty at CMS is 4.5% [**30**]. For the cross section ratio this uncertainty cancels.

A summary of all systematic uncertainties for the Z^0 and $t\bar{t}$ production cross section as well as their ratio is given in Tables 6.11, 6.11, and 4.31.

	$\Delta(\sigma_Z)$	$\Delta(\sigma_{t\bar{t}})$	$\Delta\left(\frac{\sigma_{t\bar{t}}}{\sigma_Z}\right)$
Jet energy scale		-1.7% $+2.8\%$	-1.7% $+2.8\%$
Jet energy resolution		$+1.1\%$ -0.6%	$+1.1\%$ -0.6%
Pileup	$+0.8\%$ -2.0%	$+0.2\%$ -0.2%	-0.7% $+2.0\%$
Trigger efficiencies	-1.2% $+1.0\%$	-1.3% $+1.3\%$	$+0.6\%$ -0.4%
Lepton energy scale	0.1%	$+0.3\%$ -0.7%	$+0.3\%$ -0.7%
b-tagging		1.2%	1.2%
Isolation		4%	4%
Matching scale	-1.0% -1.3%	-2.3% -5.4%	-1.3% -4.2%
Momentum scale	-2.7% $+1.9\%$	-3.8% -4.0%	-1.2% -5.7%
top mass m_t		-5.6% $+1.7\%$	-5.6% $+1.7\%$
PDF	1.8%	0.4%	1.8%
background	0.3%	4.4%	4.5%
total	$+2.3\%$ -4.2%	$+7.1\%$ -10.1%	$+7.6\%$ -11.3%
Lumi	4.5%	4.5%	
Branching ratio	0.1%	3.4%	3.4%

Table 4.30: Systematic uncertainties for the measurement of the Z^0 and $t\bar{t}$ production cross section as well as their ratio $\Delta(\sigma_Z)$, $\Delta(\sigma_{t\bar{t}})$ or $\Delta\left(\sigma_{t\bar{t}}/\sigma_Z\right)$, respectively, in the ee channel. Uncertainties of the luminosity and the branching ratio (BR) are not included in the total uncertainty given here. For each contribution the first value corresponds to an upward variation of the parameter, the second value to a downward variation.

	$\Delta(\sigma_Z)$	$\Delta(\sigma_{t\bar{t}})$	$\Delta\left(\frac{\sigma_{t\bar{t}}}{\sigma_Z}\right)$
Jet energy scale		-2.2% $+2.8\%$	-2.2% $+2.8\%$
Jet energy resolution		$+0.7\%$ -0.6%	$+0.7\%$ -0.6%
Pileup	$+0.6\%$ -1.7%	$+0.3\%$ -0.3%	-0.3% $+1.4\%$
Trigger efficiencies	-0.8% $+1.1\%$	-1.2% $+1.2\%$	$+0.2\%$ -0.3%
b-tagging		1.2%	1.2%
Isolation		4%	4%
Matching scale	-0.6% -0.7%	$+3.8\%$ -0.4%	$+4.4\%$ $+0.3\%$
Momentum scale	-3.0% $+1.6\%$	$+2.2\%$ -2.4%	$+5.4\%$ -4.0%
top mass m_t		-0.8% $+1.6\%$	-0.8% $+1.6\%$
PDF	1.7%	0.4%	1.7%
background	0.3%	5.4%	5.5%
total	$+2.7\%$ -4.0%	$+8.9\%$ -7.8%	$+10.6\%$ -8.6%
Lumi	4.5%	4.5%	
Branching ratio	0.2%	2.0%	2.0%

Table 4.31: Systematic uncertainties for the measurement of the Z^0 and $t\bar{t}$ production cross section as well as their ratio $\Delta(\sigma_Z)$, $\Delta(\sigma_{t\bar{t}})$ or $\Delta\left(\sigma_{t\bar{t}}/\sigma_Z\right)$, respectively, in the $\mu\mu$ channel. Uncertainties of the luminosity and the branching ratio (BR) are not included in the total uncertainty given here. For each contribution the first value corresponds to an upward variation of the parameter, the second value to a downward variation.

	$\Delta(\sigma_{t\bar{t}})$
Jet energy scale	-2.0% $+2.5\%$
Jet energy resolution	$+0.9\%$ -1.2%
Pileup	$+0.4\%$ -0.5%
Trigger efficiencies	-1.3% $+1.3\%$
Lepton energy scale	$+0.2\%$ -0.1%
b-tagging	1.2%
Isolation	4%
Matching scale	$+0.3\%$ -1.5%
Momentum scale	$+0.8\%$ $+0.2\%$
top mass m_t	-1.5% $+2.2\%$
Background	1.0%
PDF	0.5%
total	$+5.7\%$ -5.5%
Lumi	4.5%
Branching ratio	2.3%

Table 4.32: Systematic uncertainties for the measurement of the Z^0 and $t\bar{t}$ production cross section as well as their ratio $\Delta(\sigma_Z)$, $\Delta(\sigma_{t\bar{t}})$ or $\Delta\left(\sigma_{t\bar{t}}/\sigma_Z\right)$, respectively, in the $e\mu$ channel. Uncertainties of the luminosity and the branching ratio (BR) are not included in the total uncertainty given here. For each contribution the first value corresponds to an upward variation of the parameter, the second value to a downward variation.

CHAPTER 5

Results and Conclusions

1. Results

1.1. Cross section determination

The inclusive cross section σ_{inc} is determined as follows:

$$\sigma_{inc} = \frac{N_{sel} - N_{bg}}{\epsilon_{inc} \cdot BR \cdot L}. \tag{5.1}$$

Here, N_{sel} is the number of selected events, N_{bg} denotes the number of background events, ϵ_{inc} the total reconstruction and selection efficiency accounting for detector acceptance, BR the branching ratio for the particular decay channel and L the luminosity. The resulting Z^0 and $t\bar{t}$ production cross sections and their ratio are listed in Tables 5.1, 5.2, and 5.3. The obtained cross sections are in very good agreement with recent CMS measurements of the inclusive $t\bar{t}$ cross sections in different decay channels [**29**]. The measured Z^0 production cross section is in a very good agreement with the CMS measurement [**44**]. The statistical uncertainty of the Z^0 production cross section is about 0.1% and is therefore neglected.

channel	$\sigma_{t\bar{t},inc}$ $[pb]$
ee	187.8 $\pm$8.7(stat.) $\pm^{14.8}_{20.1}$(sys) $\pm$8.5(lumi)
$\mu\mu$	167.2 $\pm$7.7(stat.) $\pm^{15.2}_{13.5}$(sys) $\pm$7.5(lumi)
$e\mu$	184.5 $\pm$4.3(stat.) $\pm^{11.3}_{11.1}$(sys) $\pm$8.3(lumi)

Table 5.1: Inclusive cross sections of $t\bar{t}$ production, $\sigma_{t\bar{t},inc}$, measured using the ee $\mu\mu$ and $e\mu$ channel.

channel	$\sigma_{Z,inc}$ $[nb]$
ee	31.4 $\pm^{0.7}_{1.3}$(sys) $\pm$1.4(lumi)
$\mu\mu$	30.8 $\pm^{0.8}_{1.2}$(sys) $\pm$1.4(lumi)

Table 5.2: Inclusive cross sections for Z^0 production, $\sigma_{Z,inc}$, measured using the ee and $\mu\mu$ channel.

channel	$\frac{\sigma_{t\bar{t},inc}}{\sigma_{Z,inc}} \cdot 10^3$
ee	5.98 $\pm$0.28(stat.) $\pm^{0.50}_{0.71}$(sys)
$\mu\mu$	5.43 $\pm$0.24(stat.) $\pm^{0.59}_{0.44}$(sys)

Table 5.3: Ratio of the inclusive production cross sections of $t\bar{t}$ pairs to Z^0 $\frac{\sigma_{t\bar{t},inc}}{\sigma_{Z,inc}}$ measured using the ee and $\mu\mu$ channel.

channel	$\sigma^R_{t\bar{t},inc}$ $[pb]$
ee	172.8 $\pm$8.0(stat.) $\pm^{13.2}_{19.5}$(sys.) $\pm$7.5(theo.)
$\mu\mu$	156.9 $\pm$7.2(stat.) $\pm^{16.6}_{13.5}$(sys.) $\pm$6.8(theo.)

Table 5.4: Inclusive cross section, $\sigma^R_{t\bar{t},inc}$, obtained by using the cross section ratio of $t\bar{t}$ production to Z^0 production in the ee and $\mu\mu$ channel. The uncertainty referred to as (theo.) denotes the uncertainty due to the prediction for the Z^0 production cross section.

The measurement of both, $t\bar{t}$ and Z^0 production cross sections is limited by the systematic uncertainty. With increasing luminosity at the LHC, data-driven methods for systematic uncertainty estimation will be exploited to a larger extent, aiming for a minimization of the systematic uncertainty. However, it will be difficult to improve the luminosity measurement significantly. Therefore, one can think of new ways of normalization for the determination of the $t\bar{t}$ cross section. In this work, the Z^0 production cross section is used as a normalization to obtain the $t\bar{t}$ production cross section, instead of the luminosity. The measured cross section ratio, $\left(\sigma_{t\bar{t},ll}/\sigma_{Z,ll}\right)_{meas}$, is multiplied by the NNLO prediction of the Z^0 production cross section [**24**], $\sigma_{Z\to ll,theo}$, described in Chapter 2 and corrected for branching ratios using Equation 5.2.

$$\sigma^R_{t\bar{t},inc} = \left(\frac{\sigma_{t\bar{t},ll}}{\sigma_{Z,ll}}\right)_{meas} \cdot \sigma_{Z\to ll,theo} \cdot \frac{1}{BR_{t\bar{t}\to X\to ll}} \tag{5.2}$$

The resulting $t\bar{t}$ production cross sections $\sigma^R_{t\bar{t}}$ are listed in Table 5.4. The uncertainty is dominated by the PDF uncertainty of 4.1% while the estimate for missing higher order corrections contributes with about 1%. The uncertainty on the PDF can be reduced by inclusion of more recent measurements in the PDF determination.

1.2. Combination

In order to achieve a more precise result, the cross sections measured in the different channels are combined. This is done by weighting the cross section measured in each channel i, σ_i, with its statistical uncertainty $\Delta_{stat}(\sigma_i)$ [**33**] , which is treated as uncorrelated:

$$\sigma_{comb} = \frac{\sum_i \left(\frac{\sigma_i}{(\Delta_{stat}(\sigma_i))^2} \right)}{\sum_i \frac{1}{(\Delta_{stat}(\sigma_i))^2}} \tag{5.3}$$

All systematic uncertainties are assumed to be 100% correlated. To estimate the influence of the systematic uncertainties and their correlations on the cross section measurement, the corresponding error-source is varied simultaneously in all analyzed channels. This leads to reduced systematic uncertainties due to variations of matching threshold and Q^2 in the simulation. The sources of systematic uncertainties of the combined cross sections and their influences on the cross-section values are summarized in Table 5.5.

	$\Delta(\sigma_{Z,comb})$	$\Delta(\sigma_{t\bar{t},comb})$	$\Delta(\sigma^R_{t\bar{t},comb})$
Jet energy scale		-2.0% $+2.6\%$	-2.0% $+2.8\%$
Jet energy resolution		$+0.9\%$ -1.0%	$+0.9\%$ -0.6%
Pileup	$+0.7\%$ -1.9%	0.4%	-0.5% $+1.7\%$
Trigger efficiencies	-1.0% $+1.1\%$	1.3%	0.4%
Lepton energy scale	$< 0.1\%$	0.2%	$+0.2\%$ -0.3%
b-tagging		1.2%	1.2%
Isolation		4%	4%
Matching scale	-0.8% -1.0%	$+0.5\%$ -1.9%	$+1.7\%$ -1.8%
Momentum scale	-2.9% $+1.7\%$	$+0.3\%$ -2.1%	$+2.3\%$ -4.8%
top mass m_t		-2.1% $+2.0\%$	-3.1% $+1.7\%$
PDF	1.8%	0.5%	1.8%
background	0.3%	2.4%	5.0%
Branching ratio	0.2%	2.4%	2.7%
total	$+2.8\%$ -4.2%	$+6.6\%$ -7.0%	$+8.7\%$ -9.7%
Luminosity	4.5%	4.5%	
theo			4.3%

Table 5.5: Systematic uncertainties of the combined cross section $\sigma_{t\bar{t},comb}$ and the combined cross section obtained with the cross section ratio $\sigma^R_{t\bar{t},comb}$. For each contribution the first value corresponds to an upward variation of the parameter, the second value to a downward variation.

After combining the channels the Z^0 and the $t\bar{t}$ production cross section are found as follows:

$\sigma_{Z,comb} = 31.1\ ^{+0.9}_{-1.3}$ (syst.) ± 1.4 (lumi.) nb

$\sigma_{t\bar{t},comb} = 181.6 \pm 3.5$ (stat.) $^{+12.0}_{-12.7}$ (syst.) ± 8.2 (lumi.) pb

The cross section for $t\bar{t}$ production determined using the ratio is found to be:

$\sigma^{R}_{t\bar{t},comb} = 164.0 \pm 5.4$ (stat.) $^{+14.2}_{-15.9}$ (syst.) ± 7.1 (theo.) pb

1.3. Comparison to theory predictions

The measured Z^0 production cross section in the dileptonic final state is compared to the theoretical prediction [**24**] in Figure 5.1. Assuming lepton universality, the cross sections in the ee and $\mu\mu$ channels are combined in the leptonic cross section $\sigma_{(Z\to ll)}$. This way, the uncertainty due to the partial branching ratios for muon- or electron-decays do not enter the total uncertainty. Details of the NNLO prediction of the Z^0 production cross section are described in Chapter 2. The parton distribution functions CTEQ6M [**62**] are used. The theory uncertainty includes the dominant contribution due to PDF uncertainties and the small uncertainty due to missing higher order contributions, estimated by varying the renormalization and factorization scale in the calculation. The measurement and the NNLO prediction agree very well within uncertainties.

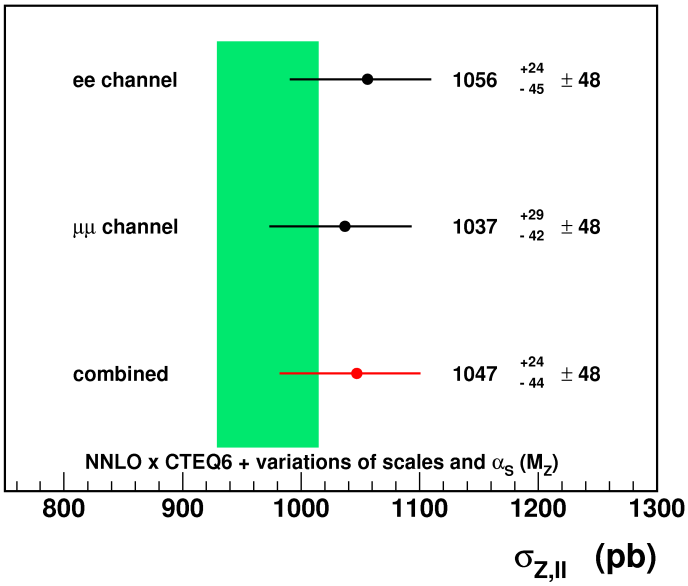

Figure 5.1: The cross section for Z^0 boson decay to two leptons as obtained in the different channels. The combination of the measurements in different channels is shown in red. The statistic uncertainties are indicated by the inner error bar, while the full error bar corresponds to the total uncertainty. The NNLO prediction [**24**] is represented by a band. The theory uncertainty includes the variation of renormalization and factorization scales, PDF uncertainty and the variation of $\alpha_S(M_Z)$ in the PDF.

The measured $t\bar{t}$ production cross sections are compared to the approximate NNLO predictions [**57, 55, 55**] in Figure 5.2. The details of the theory calculations are discussed in Chapter 2. The proton structure is described by the MSTW08NNLO [**59**] parton densities. The theory uncertainty includes missing higher order corrections, estimated by varying the renormalization and factorization scales, the PDF uncertainties and the assumptions on the value of $\alpha_s(M_Z)$ The values of the cross sections, obtained using the Z^0 cross section as normalization are also shown. The measurements are very well described by the predictions within the experimental and theoretical uncertainties.

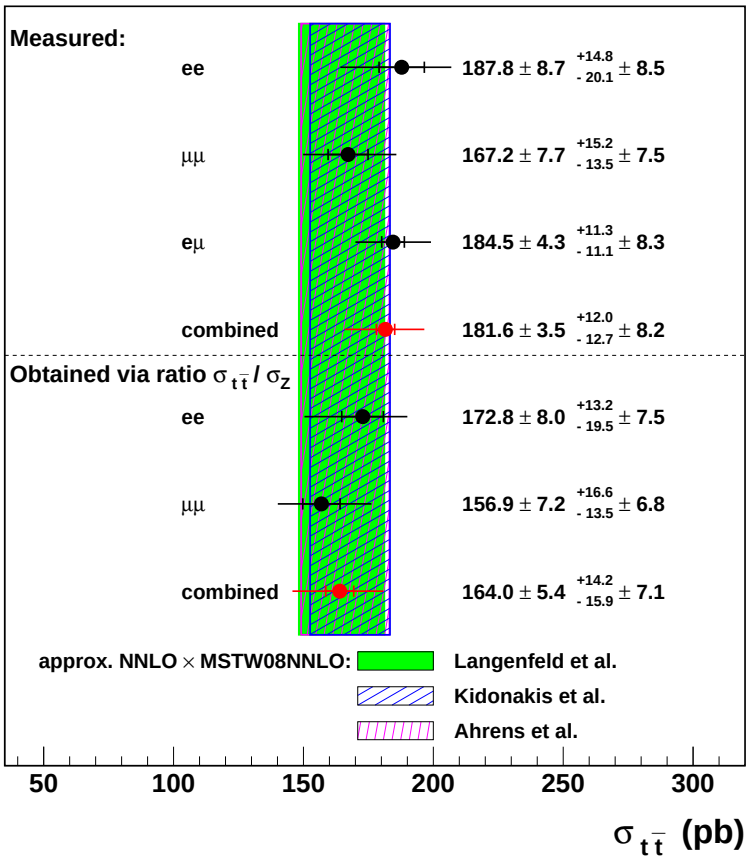

Figure 5.2: The cross section for top-quark pair production as obtained in the different channels with leptons in the final state. The combination of the measurements in different channels is shown in red. The statistic uncertainties are indicated by the inner error bar, while the full error bar corresponds to the total uncertainty. The measurements are compared to the cross-section values, obtained using the predicted cross section for Z^0 -boson production. The approx. NNLO predictions [**57, 55, 55**] are represented by shaded bands with different hashed styles (see legend). The theory uncertainty includes the variation of renormalization and factorization scales, PDF uncertainty and the variation of $\alpha_S(M_Z)$ in the PDF.

2. Conclusions

In this thesis, a measurement of the top-antitop production cross section, the Z^0 boson production cross section and their ratio is described. The decays of Z^0 bosons and top-quark pairs with leptons in the final state are studied. For the $t\bar{t}$ production cross section measurement, the discrimination between signal and background is crucial and relies on a sophisticated procedure, resulting in a variety of systematic uncertainties. Data-driven corrections are applied to the simulation, in order to reduce the influence of theory predictions on the cross section determination. The trigger efficiencies for all channels are determined double-differentially from data by performing the lepton candidate selection on a dataset based on independent triggers. The electron energy scale and resolution is re-calibrated by exploiting the precise knowledge of the Z^0 boson invariant-mass distribution. The latter is also used to study the isolation efficiencies on the kinematics of the electron and muon candidates and to correct the normalization of the dominant background contribution to the $t\bar{t}$ signal in the ee and $\mu\mu$ channel. The background to the Z^0 signal is determined from data only, such that both luminosity dependent cross section measurements are neither biased by the predictions for the $t\bar{t}$ cross section nor by the simulation of the inclusive Z^0 production cross section.

A luminosity-independent method for the determination of the $t\bar{t}$ cross section is used alternatively. The NNLO prediction for the Z^0 production cross section is used to obtain the $t\bar{t}$ production cross section from the measured cross section ratio of $t\bar{t}$ to Z^0 production. The measurement of the ratio is performed taking into account correlations in selection efficiencies, corrections and model uncertainties. The results from the different channels are combined taking into account correlations of the systematic uncertainties. These dominate the total uncertainties of the measured Z^0 and $t\bar{t}$ production cross sections, which are listed below.

$\sigma_{Z,comb} = 31.1\ \pm^{0.9}_{1.3}\ \text{(syst.)}\ \pm 1.4\ \text{(lumi.)}\ \text{nb}$

$\sigma_{t\bar{t},comb} = 181.6\ \pm 3.5\ \text{(stat.)}\ \pm^{12.0}_{12.7}\ \text{(syst.)}\ \pm 8.2\ \text{(lumi.)}\ \text{pb}$

$\sigma^{R}_{t\bar{t},comb} = 164.0\ \pm 5.4\ \text{(stat.)}\ \pm^{14.2}_{15.9}\ \text{(syst.)}\ \pm 7.1\ \text{(theo.)}\ \pm 0\ \text{(lumi.)}\ \text{pb}$

All cross-section values for Z^0 production and $t\bar{t}$ production are in agreement with Standard Model predictions at NNLO or approximate NNLO, respectively. In the top-pair production cross section obtained using the NNLO prediction for Z^0 production, the luminosity uncertainty cancels completely. However, the total systematic uncertainty is not reduced. Instead of the luminosity error, a compatible uncertainty of the same size is arising, due to the uncertainty on the NNLO prediction of the Z^0 production cross section. The latter is dominated by the uncertainty due to the PDF with only a very small contribution from the missing higher orders. In the future, the sonstent determination of the PDF using proton-proton collision data can help decreasing this uncertainty.

In 2012, the center of mass energy of the LHC will be increased to $\sqrt{s}$ =8 TeV. A reevaluation of several detector and modelling parameters has to be performed. Amongst others, the luminosity uncertainty will increase with respect to 2011 at the beginning of the data taking period, which makes the normalization to the Z^0 production cross section a method to be considered in cross section measurements.

Appendix

All MC samples are generated using the generator parameter set listed in table 5.6, 5.7 and 5.8.

Parameter	Value
BR($H \to AA$)	1.42784807E-03
m_τ for the Yukawa y_t	1.77700000E+00
m_b for the Yukawa y_b	0 ? 4.20000000E+00
$\alpha_s(m_Z)$ SM MSbar	1.18000000E-01
BR($H \to WW^*$)	7.46091936E-02
top pole mass	1.72500000E+02
BR($H \to ZZ^*$)	6.90768858E-03
$\alpha_{em}^{-1}(m_Z)$ SM MSbar	1.32506980E+02
m_t for the Yukawa y_t	1.64500000E+02
bottom pole mass	4.80000000E+00
W width	2.04759951E+00
Vud for Cabibbo matrix	9.75000000E-01
BR($H \to gg$)	3.02217699E-02
BR($H \to \tau^-\tau^+$)	4.31827533E-02
Z mass	9.11880000E+01
W mass	8.04190000E+01
BR($H \to c\bar{c}$)	8.27656837E-02
Z width	2.44123340E+00
H mass	1.20000000E+02
ickkw	1
G_{Fermi}	1.16639000E-05
tau mass	1.77700000E+00
top width	1.45412849E+00
m_c for the Yukawa y_c	1.42000000E+00
BR($H \to b\bar{b}$)	7.17702310E-01
H width	5.75165778E-03
bwcutoff	5
Z mass (as input parameter)	9.11880000E+01
BR($H \to t\bar{t}$)	0.00000000E+00

Table 5.6: Parameter set used to generate the MadGraph MC samples.

Parameter	Value
$\alpha_{em}(m_Z)^{-1}$ SM MSbar	128.930
Z^0 width	2.495
m_t	172.5
$sin^2(\theta_W)$	0.23102
W width	2.124
wtop	1.7
Z^0 mass	91.188
W mass	80.425
$\alpha_s(m_Z)$ SM MSbar	0.11798

Table 5.7: Parameter set used to generate the Powheg MC samples.

Parameter	Value	Description
MSTU(21)	1	Check on possible errors during program execution
'MSTJ(22)	2	Decay those unstable particles
'PARJ(71)	10 .	for which ctau 10 mm
'MSTP(33)	0	no K factors in hard cross sections
'MSTP(2)	1	which order running alphaS
'MSTP(51)	10042	structure function chosen (external PDF CTEQ6L1)
'MSTP(52)	2	work with LHAPDF
'PARP(82)	1.832	pt cutoff for multiparton interactions
'PARP(89)	1800.	sqrts for which PARP82 is set
'PARP(90)	0.275	Multiple interactions: rescaling power
'MSTP(95)	6	CR (color reconnection parameters)
'PARP(77)	1.016	CR
'PARP(78)	0.538	CR
'PARP(80)	0.1	Prob. colored parton from BBR
'PARP(83)	0.356	Multiple interactions: matter distribution parameter
'PARP(84)	0.651	Multiple interactions: matter distribution parameter
'PARP(62)	1.025	ISR cutoff
'MSTP(91)	1	Gaussian primordial kT
'PARP(93)	10.0	primordial kT-max
'MSTP(81)	21	multiple parton interactions 1 is Pythia default
'MSTP(82)	4	Defines the multi-parton model

Table 5.8: Pythia parameters used to generate the Pythia MC samples.

Sample	cross section $[pb^{-1}]$	Luminosity
TTJets_TuneZ2_7TeV-MadGraph-tauola	169.9	21 fb^{-1}
DYJetsToLL_TuneZ2_M-50_7TeV-MadGraph-tauola	3048	11 fb^{-1}
T_TuneZ2_tW-channel-DR_7TeV-powheg-tauola	7.87	113 fb^{-1}
Tbar_TuneZ2_tW-channel-DR_7TeV-powheg-tauola	7.87	113 fb^{-1}
WWTo2L2Nu_TuneZ2_7TeV_pythia6_tauola	4.51	46 fb^{-1}
WZTo3LNu_TuneZ2_7TeV_pythia6_tauola	0.61	335 fb^{-1}
ZZ_TuneZ2_7TeV_pythia6_tauola	7.4	565 fb^{-1}
WJetsToLNu_TuneZ2_7TeV-MadGraph-tauola	31314	2.6 fb^{-1}
DYToEE_M-10To20_TuneZ2_7TeV-pythia6	3457	614 fb^{-1}
DYToMuMu_M-10To20_TuneZ2_7TeV-pythia6	3457	0.6 fb^{-1}
DYToTauTau_M-10To20_TuneZ2_7TeV-pythia6-tauola	3457	0.6 fb^{-1}
DYToEE_M-20_TuneZ2_7TeV-pythia6	1666	1.4 fb^{-1}
DYToMuMu_M-20_TuneZ2_7TeV-pythia6	1666	1.3 fb^{-1}
DYToTauTau_M-20_TuneZ2_7TeV-pythia6-tauola	1666	1.2 fb^{-1}
QCD_Pt-20_MuEnrichedPt-15_TuneZ2_7TeV-pythia6	84679	0.07 pb^{-1}
QCD_Pt-20to30_EMEnriched_TuneZ2_7TeV-pythia6	2.50×10^6	0.15 pb^{-1}
QCD_Pt-30to80_EMEnriched_TuneZ2_7TeV-pythia	3.63×10^6	1.2 pb^{-1}
QCD_Pt-80to170_EMEnriched_TuneZ2_7TeV-pythia6	143×10^3	9 pb^{-1}

Table 5.9: MC samples used in this analysis, the cross sections, they are normalised to, and the approximate production luminosity.

channel	triggers
$\mu^+\mu^-$ runs 160431-163869	HLT_DoubleMu7_*
$\mu^+\mu^-$ runs 165008-167913	HLT_Mu13_Mu8_v*
$\mu^+\mu^-$ MC	HLT_DoubleMu7_*
e^+e^- (data and MC)	HLT_Ele17_CaloIdL_CaloIsoVL_Ele8_CaloIdL_CaloIsoVL_v*
	HLT_Ele17_CaloIdT_TrkIdVL_CaloIsoVL_TrkIsoVL_
	Ele8_CaloIdT_TrkIdVL_CaloIsoVL_TrkIsoVL_v*
$e^\pm\mu^\pm$ (data and MC)	HLT_Mu8_Ele17_CaloIdL_*
	HLT_Mu17_Ele8_CaloIdL_*

Table 5.10: HLT Triggers used in this analysis.

Trigger path
HLT_CentralJet80_MET65_v1
HLT_CentralJet80_MET80_v1
HLT_CentralJet80_MET100_v1
HLT_CentralJet80_MET160_v1
DiJet60_MET45_v1
PFMHT150_v2
MET100_v1
MET120_v1
MET200_v1

Table 5.11: HLT cross triggers used for trigger analysis.

Dataset	Luminosity
/METBTag/Run2011A-May10ReReco-v1/AOD	214.8 pb^{-1}
/MET/Run2011A-PromptReco-v4/AOD	927.9 pb^{-1}

Table 5.12: Datasets used for trigger analysis and their corresponding luminosity.

sample
TTJets_TuneZ2_mass169_5_7TeV-madgraph-tauola
TTJets_TuneZ2_mass175_5_7TeV-madgraph-tauola

Table 5.13: MC samples used to determine the influence of a variation of the top mass on the measured cross sections.

sample
TTjets_TuneZ2_scaleup_7TeV-MadGraph-tauola
TTjets_TuneZ2_scaledown_7TeV-MadGraph-tauola
TTjets_TuneZ2_matchingup_7TeV-MadGraph-tauola
TTjets_TuneZ2_matchingdown_7TeV-MadGraph-tauola
ZJetsToLL_TuneZ2_scaleup_7TeV-MadGraph-tauola
ZJetsToLL_TuneZ2_scaledown_7TeV-MadGraph-tauola
ZJetsToLL_TuneZ2_matchingup_7TeV-MadGraph-tauola
ZJetsToLL_TuneZ2_matchingdown_7TeV-MadGraph-tauola

Table 5.14: Systematic samples used to determine the effect of Q^2 and matching scale variation on the measured cross sections.

parameter	value
W mass	80.398 GeV
W width	2.141 GeV
Z mass	91.1876 GeV
Z width	2.4952
top mass	172.5 GeV
b mass	4.8 GeV
c mass	1.27 GeV
α_{QED}	0.007297352

Table 5.15: Parameters used for the calculation of the Z^0 cross section in the dileptonic channels with FEWZ [**52**].

Bibliography

[1] CMS Detector Drawings. `http://cmsinfo.web.cern.ch/cmsinfo/Media/Images/Detector/Detector%20Drawings/index.html`.

[2] CMS Media. `http://cmsinfo.web.cern.ch/cmsinfo/Media`.

[3] LHC luminosity charts. `http://lpcc.web.cern.ch/LPCC/index.php?page=luminosity_charts`.

[4] Observation of the Top Quark. *Phys. Rev. Lett.*, 74:2632–2637, Apr 1995.

[5] Particle-Flow Event Reconstruction in CMS and Performance for Jets, Taus, and Missing E_T . *CMS Physics Analysis Summary*, CMS-PAS-PFT-09-001, 2009.

[6] Combined Standard Model Higgs boson searches with up to 2.3 inverse femtobarns of pp collision data at $\sqrt{s} = 7$ TeV at the LHC. 2011.

[7] F.D. Aaron et al. Combined Measurement and QCD Analysis of the Inclusive e+- p Scattering Cross Sections at HERA. *JHEP*, 1001:109, 2010.

[8] V.M. Abazov et al. Measurement of B($t \to$ Wb) /B($t \to$ Wq) at $\sqrt{s}$ = 1.96-TeV. *Phys.Lett.*, B639:616–622, 2006.

[9] S. Agostinelli, J. Allison, K. Amako, J. Apostolakis, H. Araujo, P. Arce, M. Asai, D. Axen, S. Banerjee, G. Barrand, F. Behner, L. Bellagamba, J. Boudreau, L. Broglia, A. Brunengo, H. Burkhardt, S. Chauvie, J. Chuma, R. Chytracek, G. Cooperman, G. Cosmo, P. Degtyarenko, A. Dell'Acqua, G. Depaola, D. Dietrich, R. Enami, A. Feliciello, C. Ferguson, H. Fesefeldt, G. Folger, F. Foppiano, A. Forti, S. Garelli, S. Giani, R. Giannitrapani, D. Gibin, J.J. Gmez Cadenas, I. Gonzlez, G. Gracia Abril, G. Greeniaus, W. Greiner, V. Grichine, A. Grossheim, S. Guatelli, P. Gumplinger, R. Hamatsu, K. Hashimoto, H. Hasui, A. Heikkinen, A. Howard, V. Ivanchenko, A. Johnson, F.W. Jones, J. Kallenbach, N. Kanaya, M. Kawabata, Y. Kawabata, M. Kawaguti, S. Kelner, and P. Kent. Geant4 a simulation toolkit. *Nuclear Instruments and Methods in Physics Research Section A: Accelerators, Spectrometers, Detectors and Associated Equipment*, 506(3):250 – 303, 2003.

[10] Valentin Ahrens, Andrea Ferroglia, Matthias Neubert, Ben D. Pecjak, and Li Lin Yang. Renormalization-Group Improved Predictions for Top-Quark Pair Production at Hadron Colliders. *JHEP*, 1009:097, 2010.

[11] M. Aliev, H. Lacker, U. Langenfeld, S. Moch, P. Uwer, et al. HATHOR: HAdronic Top and Heavy quarks crOss section calculatoR. *Comput.Phys.Commun.*, 182:1034–1046, 2011.

[12] G. Alterelli and G. Parisi. Asymptotic freedom in parton language. *Nucl. Phys*, 1977.

[13] Johan Alwall et al. MadGraph/MadEvent v4: The New Web Generation. *JHEP*, 09:028, 2007.

[14] M. Arneodo et al. Measurement of the proton and deuteron structure functions, F2(p) and F2(d), and of the ratio sigma(L)/sigma(T) . *Nucl. Phys.*, B483:3–43, 1997.

[15] S.Mert Aybat, Lance J. Dixon, and George F. Sterman. The Two-loop soft anomalous dimension matrix and resummation at next-to-next-to leading pole. *Phys.Rev.*, D74:074004, 2006.

[16] Christian W. Bauer, Sean Fleming, and Michael E. Luke. Summing Sudakov logarithms in B $\to$ X(s gamma) in effective field theory. *Phys.Rev.*, D63:014006, 2000.

[17] Werner Bernreuther. Top quark physics at the LHC. *J.Phys.G*, G35:083001, 2008.

[18] Oliver Sim Brning, Paul Collier, P Lebrun, Stephen Myers, Ranko Ostojic, John Poole, and Paul Proudlock. *LHC Design Report*. CERN, Geneva, 2004.

[19] Matteo Cacciari, Gavin P. Salam, and Gregory Soyez. The anti- k t jet clustering algorithm. *Journal of High Energy Physics*, 2008(04):063, 2008.

[20] Stefano Catani, Leandro Cieri, Giancarlo Ferrera, Daniel de Florian, and Massimiliano Grazzini. Vector boson production at hadron colliders: A Fully exclusive QCD calculation at NNLO. *Phys.Rev.Lett.*, 103:082001, 2009.
[21] R. S. Chivukula. Electroweak symmetry breaking. *J.Phys.: Conf.Ser.*
[22] `https://hypernews.cern.ch/HyperNews/CMS/get/ewk-dileptons/45.html`, 2012.
[23] Cuts in Categories (CiC) Electron Identification. `https://twiki.cern.ch/twiki/bin/view/CMSPublic/SWGuideCategoryBasedElectronID`.
[24] Standard Model cross sections. `https://twiki.cern.ch/twiki/bin/viewauth/CMS/StandardModelCrossSections`.
[25] Jet Energy Corrections: Official Software Tools for applying JEC Corrections and Uncertainties. `https://twiki.cern.ch/twiki/bin/view/CMSPublic/WorkBookJetEnergyCorrections#JetEnCor2011`, 2012.
[26] Jet Identification. `https://twiki.cern.ch/twiki/bin/viewauth/CMS/JetID`, 2012.
[27] The CMS Collaboration. `https://twiki.cern.ch/twiki/bin/viewauth/CMS/TopLeptonPlusJets2010Systematics`. CMS Twiki.
[28] The CMS Collaboration. CMS Physics Technical Design Report Volume I : Detector Performance and Software. CMS-TDR-008-1.
[29] The CMS Collaboration. Combination of top pair production cross section measurements. CMS PAS TOP-11-024.
[30] The CMS Collaboration. Measurement of CMS Luminosity. CMS PAS EWK-10-004.
[31] The CMS Collaboration. Measurement of the inelastic pp cross section at $\sqrt{s} = 7$ TeV with the CMS detector. CMS PAS-PWD-11-001.
[32] The CMS Collaboration. Measurement of the ttbar production cross section in the dilepton channel in pp collisions at 7 TeV with a luminosity of 1.14 fb-1. CMS PAS Top-11-005.
[33] The CMS Collaboration. Measurement of Top Quark Pair Differential Cross Sections at $\sqrt{s} = 7$ TeV. PAS TOP-11-013.
[34] The CMS Collaboration. Top quark mass determination from the top pair cross section in the di-lepton channel. CMS PAS Top-11-008.
[35] The CMS Collaboration. CMS MUON Technical Design Report. dec. 1997. CMS TDR 3.
[36] The CMS Collaboration. Plans for Jet Energy Corrections at CMS. Jul 2008.
[37] The CMS Collaboration. The CMS experiment at the CERN LHC. *Journal of Instrumentation*, 3(08):S08004, 2008.
[38] The CMS Collaboration. Track reconstruction in the CMS Tracker, 2009. CMS PAS TRK-09-001-pas-v0.
[39] The CMS Collaboration. Alignment of the CMS silicon tracker during commissioning with cosmic rays. *Journal of Instrumentation*, 5(03):T03009, 2010.
[40] The CMS Collaboration. Determination of the Jet Energy Scale in CMS with pp collisions at $\sqrt{s} =$ 7 TeV, 2010. PAS JME-10-010.
[41] The CMS Collaboration. Performance of the CMS hadron calorimeter with cosmic ray muons and LHC beam data. *Journal of Instrumentation*, 5(03):T03012, 2010.
[42] The CMS Collaboration. Absolute Calibration of Luminosity Measurement at CMS: Summer 2011 Update. 2011.
[43] The CMS Collaboration. Measurement of btagging efficiency using ttbar events, 2011. CMS PAS BTV-11-003.
[44] The CMS Collaboration. Measurement of the inclusive W and Z production cross sections in pp collisions at $\sqrt{s} =$ TeV with the CMS experiment. *Journal of High Energy Physics*, 2011:1–76, 2011. 10.1007/JHEP10(2011)132.
[45] The CMS Collaboration. Measurement of the Rapidity and Transverse Momentum Distributions of Z Bosons in pp Collisions at $\sqrt{s} = 7$ TeV. 2011.
[46] UA1 Collaboration. Experimental observation of isolated large transverse energy electrons with associated missing energy at $\sqrt{s} = 540$ GeV. *Phys. Lett.*, 1983.
[47] M R Whalley D. Bourilkov, R C Group. LHAPDF: PDF Use from the Tevatron to the LHC. arxiv:hep-ph/0605240v2, May 2006.

[48] Dirk Johannes Dammann, Joachim Mnich, and Achim Geiser. *Production Cross Section Measurement of Top-Antitop Pairs in the Dimuon Decay Channel at $\sqrt{s} = 7TeV$ with the CMS Experiment. oai:cds.cern.ch:1361031.* PhD thesis, Hamburg U., 2011. presented 2011.
[49] N. Davidson, G. Nanava, T. Przedzinski, E. Richter-Was, and Z. Was. Universal Interface of TAUOLA Technical and Physics Documentation. *Comput.Phys.Commun.*, 183:821–843, 2012.
[50] Y. L. Dokshitzer. Calculation of the Structure Functions for Deep Inelastic Scattering and e+ e- Annihilation by Perturbation Theory in Quantum Chromodynamics. *Sov.Phys.JETP*, 1977.
[51] C. Adloff et al., 2003.
[52] Ryan Gavin, Ye Li, Frank Petriello, and Seth Quackenbush. FEWZ 2.0: A code for hadronic Z production at next-to-next-to-leading order. *Comput.Phys.Commun.*, 182:2388–2403, 2011.
[53] V.N. Gribov and L.N. Lipatov. Deep inelastic scattering in perturbation theory. *Sov.J.Nucl.Phys*, 1972.
[54] K.Lipka for the H1 and ZEUS experiments. Recent results from HERA and their impact for LHC. 2012.
[55] Nikolaos Kidonakis. Next-to-next-to-leading soft-gluon corrections for the top quark cross section and transverse momentum distribution. *Phys.Rev.*, D82:114030, 2010.
[56] Makoto Kobayashi and Toshihide Maskawa. CP Violation in the Renormalizable Theory of Weak Interaction. *Prog. Theor. Phys.*, 49:652–657, 1973.
[57] U. Langenfeld, S. Moch, and P. Uwer. Measuring the running top-quark mass. *Phys.Rev.*, D80:054009, 2009.
[58] L.N. Lipatov. The parton model and perturbation theory. *Sov.J.Nucl.Phys*, 1975.
[59] A.D. Martin, W.J. Stirling, R.S. Thorne, and G. Watt. Parton distributions for the LHC. *Eur.Phys.J.*, C63:189–285, 2009.
[60] Sebastian Naumann-Emme. Simultaneous measurement of top quark mass and jet energy scale using template fits at the CMS experiment.
[61] Particle Data Group: K. Nakamura et al. PDG Particle Listings, 2010. `http://pdg.lbl.gov/2010/listings/contents_listings.html`.
[62] J. Pumplin et al. New generation of parton distributions with uncertainties from global QCD analysis. *JHEP*, 07:012, 2002.
[63] C Oleari S.Frixione, P.Nason. Matching NLO QCD computations with Parton Shower simulations: the POWHEG method. *JHEP*, 11:070, 2007.
[64] Torbjorn Sjostrand, Stephen Mrenna, and Peter Z. Skands. PYTHIA 6.4 Physics and Manual. *JHEP*, 05:026, 2006.
[65] Precision electroweak measurements on the Z resonance. *Physics Reports*, 427(5?6):257 – 454, 2006.
[66] A. W. Thomas and Wolfram Weise. *The Structure of the Nucleon.* 2000.
[67] M. Tzanov, D. Naples, S. Boyd, J. McDonald, V. Radescu, R. A. Johnson, N. Suwonjandee, M. Vakili, J. Conrad, B. T. Fleming, J. Formaggio, J. H. Kim, S. Koutsoliotas, C. McNulty, A. Romosan, M. H. Shaevitz, P. Spentzouris, E. G. Stern, A. Vaitaitis, E. D. Zimmerman, R. H. Bernstein, L. Bugel, M. J. Lamm, W. Marsh, P. Nienaber, N. Tobien, J. Yu, T. Adams, A. Alton, T. Bolton, J. Goldman, M. Goncharov, L. de Barbaro, D. Buchholz, H. Schellman, G. P. Zeller, J. Brau, R. B. Drucker, R. Frey, D. Mason, S. Avvakumov, P. de Barbaro, A. Bodek, H. Budd, D. A. Harris, K. S. McFarland, W. K. Sakumoto, and U. K. Yang. Precise measurement of neutrino and antineutrino differential cross sections. *Phys. Rev. D*, 74:012008, Jul 2006.
[68] S. van der Meer. Calibration of the effective beam height in the ISR. oai:cds.cern.ch:296752. 1968.
[69] J. Weng. A Global Event Description using Particle Flow with the CMS Detector. 2008.
[70] Standard Model of Elementary Particles. `http://en.wikipedia.org/wiki/File:Standard_Model_of_Elementary_Particles.svg`.